Experimental investigation of methods for remediation of approach slab settlements in integral abutment bridges

by

Justin Yenne

B.S., Kansas State University, 2022

A THESIS

submitted in partial fulfillment of the requirements for the degree

MASTER OF SCIENCE

Department of Civil Engineering
Carl R. Ice College of Engineering

KANSAS STATE UNIVERSITY
Manhattan, Kansas

2024

Approved by:

Major Professor
Dr. Dunja Perić

Copyright

Abstract

Traditional bridges incorporate costly deck expansion joints that accommodate temperature induced expansion and contraction. Construction and life time maintenance of these joints impose a significant financial burden on their owners that lead to a paradigm shift resulting in development of integral bridges.

Abutments of integral abutment bridges (IABs) are seamlessly monolithically connected to girders. In fully integral bridges abutments are also monolithically connected to piles. These bridges offer numerous advantages, such as enhanced resilience, increased redundancy, decreased construction and maintenance costs, and improved quality of vehicular ride. However, the absence of expansion joints in IABs introduces difficulties associated with thermal load transfer. IABs' decks and girders undergo ambient temperature induced cyclic seasonal expansions and contractions that affect their short- and long-term behaviors. The cyclic abutment movements, towards and away from the retained backfill soil lead to a long-term buildup of the lateral earth pressure and settlement of the backfill resulting in the formation of a subsidence zone and distress of the approach slab, also known as a "bump" at the end of the bridge. The onset of a void formation often starts early after the construction of the bridge had been completed.

This thesis experimentally investigated methods for alleviation of bridge approach settlement in IABs. This was accomplished by conducting experiments on a down- scaled model of an existing integral bridge. The model abutment supported by piles and surrounded by the selected backfill soil was subjected to 100 cycles of backward-forward motion simulating the action of seasonal cyclic changes of ambient temperature. Explored alleviation methods include use of geogrid, geotextile, different configurations of expanded polystyrene (EPS) geofoam

inclusions, and different combinations of EPS geofoam and geogrid, and EPS geofoam and geotextile reinforcements. Additionally, the backfill soil failure and collapse mechanisms that contribute to development of bridge approach settlement were captured by use of digital camera and digital imaging correlation (DIC) software, a technique originating from fluid mechanics. It was found that use of geotextile and EPS geofoam, and geogrid and EPS foam were the best performing alleviation methods overall.

The insights gained from this study are crucial for alleviating bridge approach settlements in IABs, and further decreasing the maintenance costs while ensuring sustained efficiency and durability of integral bridges and transportation lifelines.

Table of Contents

List of Figures

List of Tables

Acknowledgements

I want to thank my family for being supportive throughout my schooling and beyond. The support for this research provided by Kansas Department of Transportation through KTRAN program is greatly appreciated. I also want to thank my major professor, Dr. Dunja Perić, for working with me and guiding me through my master's studies with my degree direction change going into graduate school. Lastly, I also want to give special thanks to family and friends that continuously helped me with my research especially my brother Eric Yenne, my two undergraduate research assistants, Blair Long and Ty Reishus, and my colleague Derek Bogner.

Chapter 1 - Introduction

1.1 Background

Traditional bridges include deck expansion joints that accommodate bridge expansion and contraction induced by ambient temperature. However, deck expansions joints are expensive to install and maintain, leading to significant financial burden for the owners. A need to lower the high costs associated with construction and maintenance of the traditional bridges lead to the elimination of deck expansion joints, resulting in development of integral abutment bridges (IABs) or integral bridges (IB), in which girders are seamlessly and monolithically connected to abutments.

Since construction of the first IAB in the US, in 1938, in Gallia County, Ohio (Burke, 2009) the building of integral bridges in the United States and world-wide has taken off. According to a survey conducted by the New York State Department of Transportation to other states Departments of Transportation there are now over 9,000 fully integral bridges and more than 4,000 semi-integral bridges that are being used (White & New York State Department of Transportation, 2007).

IABs usually fall into two different categories including fully-integral abutment bridge (FIAB) and semi-integral abutment bridge (SIAB). White & New York State Department of Transportation (2007) defined FIAB as a structure where bridge girders and deck are directly connected to abutments so that during thermally induced movements superstructure and substructure move together, away from and into the soil backfill. Additionally, they defined SIAB as a structure where only the backwall portion of the substructure is connected to the superstructure. Therefore, the superstructure, backwall and approach slab move together away from and into the backfill during thermal expansion and contraction.

Although structural system employed in IBs provides benefits of redundancy, increased resilience, reduced installation and maintenance costs, and improved vehicular ride quality it also has some drawbacks. Thermally induced seasonal expansion and contraction of bridge deck and girders induces a cyclic translation and rotation of the abutment away from the backfill and towards the backfill. During winter, bridges shrink and move away from the granular backfill, enabling backfill to fall into the newly created gap and resulting in the initiation of the void formation, also known as a subsidence zone shown in Figure 1-1.

Figure 1-1 Seasonal Movement of Integral Bridge Abutment

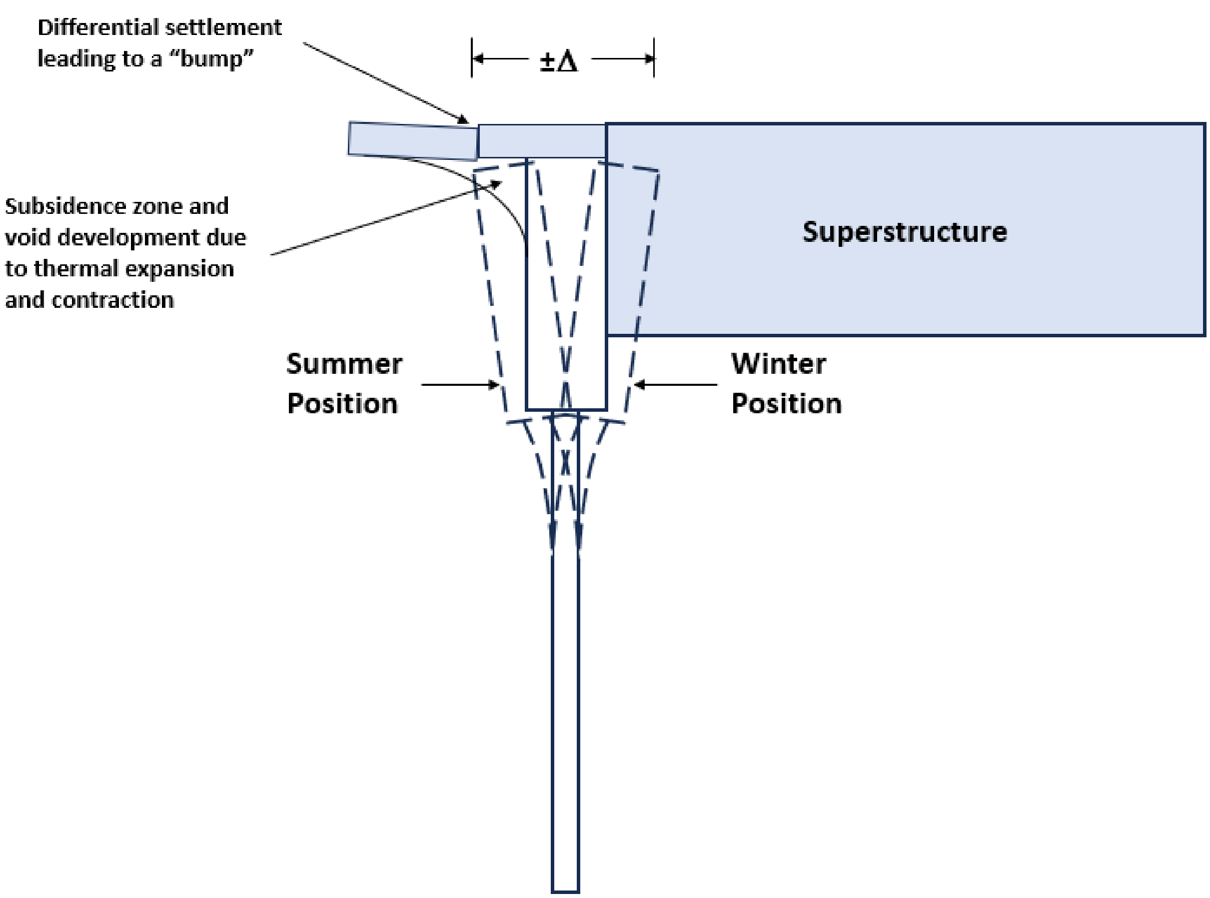

During summers, the bridge deck pushes out the abutments into the back backfill while the collapsed near surface backfill is unable to return back to the original configuration it had before the commencement of the cyclic motion. A subsequent movement of the abutment into the backfill then causes an increase in the earth pressure. The approach slab begins to experience distress due to the loss of a soil support originating in the void formation, leading to the early formation of a “bump” at the end of the bridge. The onset of void formation clearly starts with the first movement of the abutment away from the backfill, which is bound to happen early after the construction of a bridge had been completed, thus resulting in frequent and costly repairs and associated traffic interruptions.

1.2 Problem Statement

Bridge approach settlements that are induced by cyclic seasonal expansion and contraction of the IB superstructure require frequent and costly maintenance, resulting in traffic interruptions. Therefore, it is vitally important to identify successful methods for alleviation of bridge approach settlements in IBs that will improve performance of transportation infrastructure while directly increasing its cost effectiveness and minimizing traffic interruptions. The Bureau of Transportation Statics (2023) reports that the State of Kansas has the fifth largest number of bridges in the US, including many IBs, thus further stressing the importance of identifying effective methods of alleviation of bridge approach settlements.

1.3 Objectives and Scope

The scope of this study involves an experimental investigation of the soil-structure interaction associated with cyclic seasonal movements of IAB’s abutments induced by the ambient temperature change. The study focuses on development and assessment of different alleviation methods for bridge approach settlements. In addition to contact measurements, non-contact measurements based on digital imaging correlation (DIC) were also used during testing.

While the primary goal of this study is to experimentally investigate different methods of alleviation of bridge approach settlements, the specific objectives include:

- Conduct review of literature that addresses the bridge approach settlement and lateral earth pressure response in IABs.
- Conduct laboratory experiments on an instrumented physical model of abutment, piles, and backfill to study the effects of abutment movement on the soil settlement and lateral earth pressures.
- Investigate the potential ways to mitigate the soil structure interaction through the use of different configurations of EPS geofoam, geogrid, geotextile, and combinations of these methods.
- Investigate the feasibility of using DIC software to capture underlying backfill soil failure and collapse mechanisms.
- Provide conclusions ranking the effectiveness of the tested alleviation methods.

1.4 Structure of Thesis

- Chapter Two
- Chapter two presents a review of the related literature. A particular focus is given to the effects of ambient temperature changes on abutment backfill settlement in integral bridges and settlement mitigation methods. Additional focus is given to the use of digital imaging techniques in geotechnical engineering including

different software. Finally, the gaps in the current knowledge of soil structure interaction and abutment settlement in IABs are identified.

- Chapter Three

  Chapter three delves into the methodology and experimental program of the study.

- Chapter Four

  In this chapter the experimental results are presented, including information about settlement of the backfill at its interface with the abutment or EPS inclusion, about the lateral extent of settlement, measured horizontal force vs horizontal displacement and history of the horizontal displacement. Additionally, DIC results obtained from VIC-2D software are also shown.

- Chapter Five

  This chapter provides further discussion and comparison of experimental results.

- Chapter Six

  Chapter six provides conclusions derived from the experimental results obtained in this study, and recommendations for future studies concerned with different mitigation methods and the related use of DIC.

Chapter 2 - Literature Review

Bridge deck movement depends on multitude of factors such as, deck length, deck type, and geographical location (England et al., 2000). Engineers need to factor in these movements into design of integral bridges as they affect the amount of the backfill settlement behind the abutment. When abutment faces displacements of $\Delta/2H \geq \pm 0.25\%$ (England et. al., 2000), where Δ is the horizontal displacement at the top of the abutment and H is the height of the abutment, shear bands develop in the backfill soil indicating the attainment of active failure state. In granular soils, which are largely used as a backfill to ensure a proper drainage, the active failure is unavoidably accompanied by near surface collapse that creates settlement and associated subsidence zone whose size progressively increases with increasing age of the bridge. The subsequent passive movements will then produce enhanced granular flow and increased soil heave (England et al., 2000).

2.1 Integral Bridge Passive Earth Pressure

Although there is a vast number of IABs around the world and their popularity continues to increase there are no standards for correct calculation of horizontal passive earth pressures (Arsoy et al., 1999). The current guidelines are based on empirical approaches or past experiences from previously constructed structures. The traditional methods for calculating the earth pressure coefficient are quite conservative for the middle and lower half of a bridge abutment while this is not the case for the upper third where measured pressures can exceed those values calculated by Rankine or Coulomb (Huntley and Valsangkar, 2013). To improve the calculation of earth pressure at lower depths England and Tsang (2005) modified a UK Highways agency's equation for the lateral earth pressure as follows:

$$K^{*} = K_{o} + \left(\frac{\Delta}{0.03H}\right)^{.6} K_{p} \tag{2.1}$$

where, K_0 is the coefficient of earth pressure at rest, Δ is the maximum lateral movement at the top of the abutment during the seasonal temperature cycle, H is the retained height of the backfill, K_p is the coefficient of passive earth pressure using Coulomb's theory and K^* refers to the lateral earth pressure coefficient at passive failure.

As IABs undergo seasonal thermal contractions and expansions the backfill experiences a complex soil structure interaction due to its exposure to drained cyclic loading. At fixed strain amplitude cyclic loading produces progressive stiffening of the soil and increase in the peak stress ratio that can lead to attainment of a shakedown limit corresponding to a state where stresses no longer increase and no further volume change is encountered (England et al, 2000). While response of granular soil at constant stress amplitude drained loading strongly depends on the nature of imposed cyclic stress changes, it can lead to ratcheting (England et al., 2000). Hong et al. (2024) found that high cycle strain accumulation behavior can change remarkably from a shakedown to ratcheting by lowering the stress amplitude and increasing the density of a granular material, and also by rendering the fabric orientation closer to the loading direction.

2.2 Geosynthetics

2.3.1. Expanded Polystyrene Geofoam (EPS)

Expanded Polystyrene (EPS) geofoam is a polymer-based material that belongs to the realm of geosynthetics. EPS has many unique characteristics that make it a very favorable choice, including its low density that can be as low as 10kg/m^3 (Horvath, 1994) and its high compressibility. EPS geofoam comes in variety of sizes, shapes, and densities to fit the needs of

IABs. Virginia Department of Transportation developed an equation based on internal studies, shown below, for calculating the thickness of EPS geofoam placed behind the abutments of IABs (VDOT Design Manual, 2020).

$$EPS_t = 10[0.01H + 0.67(\Delta L)] \tag{2.2}$$

Where, H is the height of integral backwall/abutment in inches, ΔL is the total thermally induced movement (in inches), corresponding to the entire temperature range (total of expansion and contraction) and EPS_t is the EPS' thickness in inches.

$$EPS_t = 10[0.01h + 0.67(\Delta L)] \tag{2.3}$$

Where, h is the height of integral backwall/abutment in inches; ΔL is the total thermal induced movement corresponding to the entire temperature range in inches (total of expansion and contraction) and EPS_t is the EPS thickness in inches.

2.3.2. Geotextile

Geotextiles are widely used in geotechnical engineering for foundation reinforcement, slope protection and drainage systems due to their tensile strength, cost-effectiveness, and ease of use (Wu et al., 2020). In the context of integral bridges, geotextile is a great choice for reinforcing the backfill behind the abutment and increasing its bearing capacity, as well as for controlling soil settlement and erosion, which can contribute to the stability and longevity of integral bridges (Das and Sivakugan, 2018; Rickson, 2006).

Geotextiles are categorized based on their fabrication into woven or nonwoven. Geotextiles used for construction of mechanically stabilized earth (MSE) can be paired with the facing elements, such as concrete modular blocks (FHWA, 2018), as shown in Figure 2-1.

Figure 2-1 Common Geotextile Facing for Retaining Walls (Modified From FHWA, 2018)

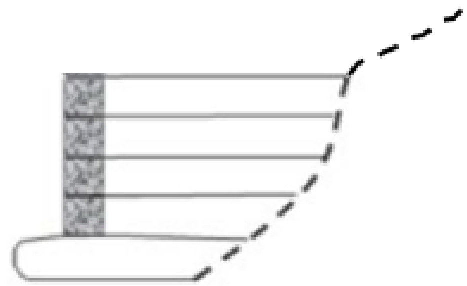

A. Modular block

Although Pellon Tru-Grid is highly unlikely to be used in the field, the ease of obtaining it facilitates its use in research (Nova-Roessig and Sitar, 2006). FHWA (2006), who used Pellon Tru-Grid, provided its properties, shown in Table 2.1 where the term “machine direction” refers to the strength along the length of the roll of the geosynthetic and the term “cross machine direction” refers to the strength along the width. The information presented in Table 2.1 shows that Pellon Tru-Grid is highly anisotropic and would be considered a “Nonwoven” fabric:

Table 2.1 Pellon Tru-Grid Tensile Strength

Geotextile	Direction	Unconfined Tensile Strength (kN/m)
Pellon Tru-Grid	Machine Direction	1.12
	Cross-Machine Direction	.09

2.3.3. Geogrid

Geogrids are high-modulus polymer materials, such as polypropylene and polyethylene, that are prepared by tensile drawing (Das and Sivakugan, 2018). They come in uniaxial biaxial, and triaxial varieties. Uniaxial geogrids have smaller openings or apertures in the transverse direction than in the longitudinal direction, while the biaxial geogrids have equal aperture sizes in transverse and longitudinal directions. The major function of geogrids is reinforcement (Das and Sivakugan, 2018). Geogrids preform the role of reinforcement in soil well because they have apertures that are large enough to allow interlocking with surrounding soil or rock (Das and Sivakugan, 2018). Sarsby (1985) found the highest efficiency of geogrid with respect to pullout was obtained for the relationship between the minimum width of the geogrid aperture (B_{GG}) and mean particle size (D_{50}) given by

$$B_{GG} > 3.5D_{50} \tag{2.4}$$

2.4 Previous Experimental Studies

Several studies (Al-Qarawi, A. 2016; Al-Qarawi, A. 2021; Liu, et al., 2021; Sigdel, et al. 2023) investigated the effects of cyclic seasonal movements of abutments on the backfill settlement. All these studies employed small-scale models with a "full abutment" configuration, wherein no piles were used. The settlement and the lateral earth pressures in these studies depended on the abutment size, the Δ/H ratio, backfill material, and number of the load cycles. The values of these parameters selected in the above studies are provided in Table 2.2.

Table 2.2. Design Parameters of Previous Experimental Studies

Reference	Abutment Height (m) x Abutment Width (m)	Δ/H (%)	Backfill Material	Number of Cycles
Al-Qarawi, A., 2016	0.30 x 0.24	0.6	Dry Siliceous Sand (γ_d = 14.33 kN/m^3 to 14.90 kN/m^3)	30
Al-Qarawi, A., 2021	1.10 x 1.50	1-2	Black Sand (γ_d = 27.20 kN/m^3)	20 – 50 (depending on test)
Liu, et al., 2021	1.00 x 0.30	0.3	Kansas River Sand (γ_d = 18.05 kN/m^3)	30
Sigdel, et al. 2023	0.96 x 1.50	1	Black Sand (γ_d = 26.38 kN/m^3 32.16 kN/m^3)	120

Liu et al. (2021) used EPS foam and geogrid to mitigate the IAB's backfill settlement induced by seasonal temperature changes. They used a uniaxial geogrid with the aperture size of 25 mm in transverse direction and 33 mm in the longitudinal direction, with layers placed 100 mm apart, up to the model abutment height of 1 m. The geogrid was wrapped around after each lift and a piece of nonwoven geotextile was added to the wrap to provide facing that prevents the soil from falling through the geogrid apertures. The Kansas river sand was subjected to 30 cycles of forward-backward abutment movements. Liu at al. (2021) measured backfill settlement at different distances away from abutment back-face. They selected a critical value of the approach slab settlement's gradient (s/x) of 0.01, as a repair criterion. Specifically, the region where the backfill settlement produced the approach slab settlement's gradient larger than 0.01 would require repair such that new support of the approach slab is provided within this region. Results of the experimental investigation conducted by Liu et al. (2021) are provided in Table 2.3.

Table 2.3 Summary of Results Provided by Liu et al. (2021)

Mitigation Method	Settlement Near the Abutment Back-face After 30 Cycles (mm)	Repair Length Measured from the Abutment Back-face (mm)
None	39.0	500
Geogrid without wrap-around facing	54.0	325
Geogrid with wrap-around facing	39.0	425
EPS foam sheet 25mm thick	37.5	425
EPS foam and geogrids without wrap-around facing	52.0	325
EPS foam and geogrid with wrap-around facing	23.0	425

Based on Table 2.3 the best performing alleviation configurations in terms of the repair length are is geogrid without wrap-around facing, EPS foam and geogrid without wrap-around facing. The second-best performing group includes geogrid with wrap-around facing, EPS foam and geogrid with wrap-around facing, and EPS foam sheet. Additionally, the smallest settlement near the back face of the abutment occurred in the EPS foam and geogrid with wrap-around facing followed by in order, EPS foam sheet, geogrid with wrap-around facing, EPS foam and geogrid without wrap-around facing, and geogrid without wrap-around facing. The settlement in reference configuration was smaller than in geogrid without wrap-around facing, and EPS foam and geogrid without wrap-around facing.

Al-Qarawi (2016), and Al-Qarawi (2021) investigated effects of different EPS geofoam sizes and shapes on the amount of lateral earth pressure and backfill settlement. Al-Qarawi (2016) placed an EPS inclusion with a density of 20 kg/m^3 behind a model abutment. Three horizontal layers of EPS were used having the following dimensions: 1) the bottom layer: 50 mm x 80 mm x 248 mm, 2) the middle layer: 100mm x 80mm x 248mm, and 3) the top layer: 150mm x 80mm x 248mm. Al-Qarawi (2016) employed a Δ/H ratio of 0.6%. The corresponding results are summarized below in Table 2.4.

Table 2.4 Al-Qarawi's Study (2016), Using EPS Foam

Mitigation Method	Settlement After 30 Cycles Next to Abutment Back-Face (mm)	Distance from the Interface where Settlement Vanishes (mm)
None	25	250
EPS Wedge	14.7	400

Additionally, Al-Qarawi (2016) showed that the maximum pressure measured at the middle of the abutment at the passive position decreased from 7.82 kPa in the case without any EPS inclusion to 2.87 kPa with the wedge-shaped EPS inclusion. Al-Qarawi (2021) also used a Δ/H ratio of 1% and a medium dense EPS geofoam inclusion having a thickness of 600 mm, placed behind the abutment. The results revealed that the maximum lateral earth pressure developed after 50 load cycles and remained equal to 80 kPa for the remainder of the test, compared to the maximum pressure of 114 kPa measured in the test without the inclusion. Al-

Qarawi et al. (2021) measured the settlements near the back-face of the abutment that are depicted in Table 2.5**.**

Table 2.5 Al-Qarawi's Study (2021)

Mitigation Method	Settlement Near Abutment Back-face After 20 Cycles (mm)	Distance Where Settlement Vanishes From the Interface (mm)
None (δ/H = 1%)	313 mm	625 mm
EPS Geofoam with 600 mm inclusion	175 mm	500 mm

2.5 Digital Imaging VIC-2D

DIC is an image-based deformation measurement, which has been widely used for measuring deformation in geotechnical models (Peters et al., 1983). It is a technique that analyzes a series of deformed configuration pictures to obtain the volumetric and shear strain (Sigdel et al., 2021). Particle imaging velocimetry-DIC has been used to study integral bridge abutment backfill responses observed during backward and forward abutment movements induced by seasonal temperature changes (Sigdel et al., 2021; Sigdel et al., 2023). These studies used two different DIC programs, GeoPIV-RG (Stanier et al., 2016) and OpenPIV (Liberzon et al., 2020). VIC-2D is another more sophisticated DIC software that can be used in geotechnical engineering (Stanier et al., 2016 Kapogianni and Sakellariou, 2017). The increased level of sophistication of VIC-2D originates in the software's ability to incorporate a higher order of subset functions, image intensity interpolation and deformation parameter optimization (Stanier et al., 2016).

All DIC programs function in a similar way. The algorithms start by selecting an area of interest and dividing the area of interest into several subset patches with dimensions L x L pixels. The software then compares the spatial variation of brightness between a subset patch and a search patch with dimensions larger than the subset patch to calculate the degree of match in both the X and Y directions (White and Take, 2002). In order to be able to capture the spatial variation a sufficient contrast and adequate texture distribution must be present (Stanier et al., 2016). The subset patch with the highest degree of match within the search area is then considered to be where the subset moved to in subsequent photographs.

Sigdel et al. (2021) used a model enclosure measuring 700 mm x 250 mm x 300 mm to conduct experimental modeling of a backfill settlement in IABs. They used GeoPIV-RG to capture a deformation pattern in the backfill behind the abutment and obtained contours indicating that the soil near the abutment was undergoing a significant deformation corresponding to active failure.

Compared to Sigdel et al. (2021), Sigdel et al. (2023) used a larger size model and investigated the use of EPS and Infinergy® as mitigation methods for minimizing the settlement behind the integral bridge abutment and compared it to a reference test employing no mitigation method. Sigdel et al. (2023) used OpenPIV to provide vector plots of the displacement. The vector plot for unmitigated experiment helped identify an active failure surface and passive failure surface. The experiment where Infinergy® was used as a mitigation method demonstrated only an active failure surface and no passive failure surface. The area of subsidence zone measured in the experiment where no mitigation was used was 0.014m^2. Sigdel et al. (2023) also measured the subsidence zone of the Infinergy® test and found that its area was equal to 0.012 m^2.

While VIC-2D was used to capture the shear strain filed in a downscaled slope model with retaining wall (Kapogianni and Sakellariou, 2017) it has not be used for capturing the deformation mechanism behind IB abutments. Kapogianni and Sakellariou (2017) were able to capture the strains that were present along with the corresponding failure mechanism. Inflow of water behind the retaining wall caused active failure of the soil while the corresponding failure surface was successfully captured by using the VIC-2D software, thus indicating that VIC-2D is a very good choice for capturing failure and collapse mechanisms behind IB abutment.

2.6 Gaps in Current Knowledge

Integral abutment bridges have been gaining increasing popularity not only because of redundancy and enhanced resilience derived from the monolithic structural system where the superstructure seamlessly connects to the substructure, but also because of a significant reduction of construction and maintenance costs resulting from the elimination of deck expansion joints. Nevertheless, seasonal cyclic changes in ambient temperature induce expansion and contraction of deck and girders that is transferred to abutments and ultimately to the backfill soil behind them. This leads to the creation of subsidence zone directly behind the abutment and a distress in the approach slab due to the loss of a soil support.

Although there have been a few recent investigations addressing the remediation of bridge approach settlement, the in depth understanding of the underlying deformation mechanisms, which is crucial for development of efficient remediation methods, has not yet emerged. In addition, majority the previously conducted research used full size abutment without piles that does not correspond to the current bridge design and construction practices in the U.S. Consequently, there is a need to investigate a more relevant case of a stub abutment founded on the piles.

The use of the different geosynthetics, including geotextile, geogrid and EPS foam has been shown to attenuate the lateral earth pressure and settlement of the soil. Nevertheless, no studies have used wrap-around geotextile for mitigation of bridge approach settlement behind abutments of IABs. Although the use of DIC in geotechnical engineering is growing, its use in the context of alleviation of bridge approach settlements and mitigation methods in IABs has been scarce.

In summary, this study adopts an experimental approach to address a more realistic bridge abutment/piles configuration along with a high-resolution digital camera and digital imaging correlation software VIC-2D for capturing and evaluating underlying failure and collapse mechanisms in unmodified backfill and in several different remediation scenarios, thus helping to provide more scientifically based evaluation of alleviation methods.

Chapter 3 - Methodology and Experimental Program

3.1 Soil Enclosure and Scaling

Abutment and supporting piles of the "Bemis Road Bridge: F-4-20" over the Nashua River in Fitchburg, Massachusetts (Perić et al., 2016) are selected as a prototype for a down-scaled experimental model in this study. The length and spans of this bridge along with its stub abutment and supporting steel piles are very similar to a those found in a typical Kansas bridge. The prototype bridge abutment height is 2.44 m and sits upon HP 310 x 100 piles that with a scale of 1:5 results in the model abutment height of 0.483 m.

The floor of the soil enclosure measures 1.09 m x 1.50 m and is constructed from two pieces of plywood, each 1.27 cm thick. The front and back walls are made of plexiglass, 2.54 cm thick, with a height of 1.12 m and a width of 1.50 m. The left and right-side walls, measuring 1.12 m in height and 1.14 m in width, are composed of two pieces of plywood, each 1.27 cm thick. All sides of the enclosure are shown in Figure 3-1. These walls are then positioned vertically and side bracing consisting of four steel angles connected together into a rectangle is placed around them, as seen in Figure 3-2. One bracing is placed at the bottom, one at the top and the third one at 0.356 m from the bottom of the container. Three additional steel angles connecting two long walls are placed at the top of the container shown in Figure 3-3.

Figure 3-1 Assembling the Testing Enclosure

The abutment, which was made of aluminum block having height of 0.483 m, width of 1.09 m, and with of 0.152 m. It is supported by two hollow aluminum piles each 3.81 cm in diameter and wall thickness of 0.508 cm, 50.8 cm tall, with center to center spacing of 54.61 cm. In accordance with recommendations provided by Meymand (1998), flexural rigidity of a model pile was scaled with respect to the prototype pile at a scale of $1/\lambda^5$, where λ is a length scale factor, equal to five in this case. These piles are inserted into pile holes drilled into four steel plates, each 1.27 cm thick, 15.24 cm long, and 5.08 cm wide, attached to the floor of the enclosure. To facilitate movement of the abutment, a screw jack is employed, and connected to a reaction frame comprising two steel channels extending along wooden vertical sides that are connected with two long threaded rods extending along the plexiglass sides shown Figure 3-2.

Figure 3-2. Soil Enclosure Showing Steel Channels and Steel Rod

Figure 3-3 View of Steel Angles Used for Bracing

3.2 Experimental Program

Kansas River Sand, which was chosen as a backfill soil in this investigation, has a peak friction angle of 42.2º, based on direct shear tests conducted at relative density of 75%, and the minimum and maximum dry unit weights of 16.02 kN/m^3 and 18.85 kN/m^3 respectively (Liu et al. 2021). Based on the grain size distribution curve provided by Liu et al. (2021), the sand has coefficients of uniformity and curvature of 3.18 and 0.9 respectively, resulting in Unified Soil Classification System (USCS) designation of purely graded sand (SP). The air-dried sand was thoroughly mixed, placed into container and subsequently compacted to a relative density of

75% making it a dense sand according Das and Sivakugan (2018). The sand was placed and compacted in five lifts below the abutment bottom and additional lifts above the bottom of the abutment. To help provide a contrast to the sand that is needed for DIC, black aquarium sand was added within about 2 cm of the plexiglass wall facing the camera.

The experimental program was designed to investigate different remediation methods including use of: 1) EPS geofoam, 2) geotextile, 3) geogrid, 4) combined EPS geofoam and geogrid, and 5) combined EPS geofoam and geotextile. Additionally, a reference test was conducted, in which no mitigation method was employed. Further details of experimental program are provided in Table 3.1.

Table 3.1 Experimental Program Details

Test	Mitigation Method	Details
T1	None/Reference	
T2	Stiff EPS Wedge	three-layer-stiff wedge
T3	Stiff EPS Inverse Wedge	three-layer stiff wedge
T4	Geotextile	five layers
T5	Geogrid	five layers
T6	Soft EPS geofoam sheet	10.2 cm thick sheet
T7	Stiff EPS geofoam sheet	10.2 cm thick sheet
T8	Soft EPS geofoam and geogrid	5.1 cm thick EPS geofoam sheet and five geogrid layers
T9	Soft EPS geofoam and geotextile	5.1 cm thick EPS geofoam sheet and five geotextile layers
T10	Soft EPS geofoam and geotextile	5.1 cm thick geotextile and eight geotextile layers

For each experiment sand was compacted as described in Section 3.2. Each experiment started from the neutral or a nearly vertical position of the abutment that corresponded to the end of the backfill compaction. All experiments were conducted in a displacement control mode whereby each cycle started by imposing a 3 mm horizontal displacement at the top of the abutment in the direction away from the backfill corresponding to a displacement between neutral and active configurations. This was followed by 3 mm displacement towards the backfill corresponding to displacement between active and neutral configurations. The abutment was subsequently moved additional 3 mm towards the backfill. Each cycle was completed by additional 3 mm displacement away from the backfill, thus, corresponding to a displacement between passive and neutral configurations. The intended displacement rate of the abutment was 24mm/min. The displacements were controlled by manually moving the screw attached to the abutment. Bridges are usually designed and built for a service life of 100 years (Maier et al. 2014), thus resulting in a total of 100 cycles being applied to the abutment top during these experiments

3.3 Experimental Details

3.3.1. Geofoam

Density, compressive resistances of EPS geofoams at different deformations, and elastic moduli are listed in Table 3.2.

Table 3.2 EPS Geofoam Properties

Property	Soft EPS Geofoam	Stiff EPS Geofoam
Density	11.2 kg/m^3	14.4 kg/m^3
Compressive Resistance @ 10% deformation	40 kPa	70 kPa
Compressive Resistance @ 5% deformation	35 kPa	55 kPa
Compressive Resistance @ 1% deformation	15 kPa	25 kPa
Elastic Modulus	1500 kPa	2500 kPa

Test T2, T3, T6, T7, T8, T9, and T10 all use the EPS geofoam in different configurations. Stiff EPS geofoam was used in tests T2 and T3, for which detailed configurations are depicted in Figures 3-4 and 3-5 respectively.

Figure 3-4 EPS Wedge Configuration

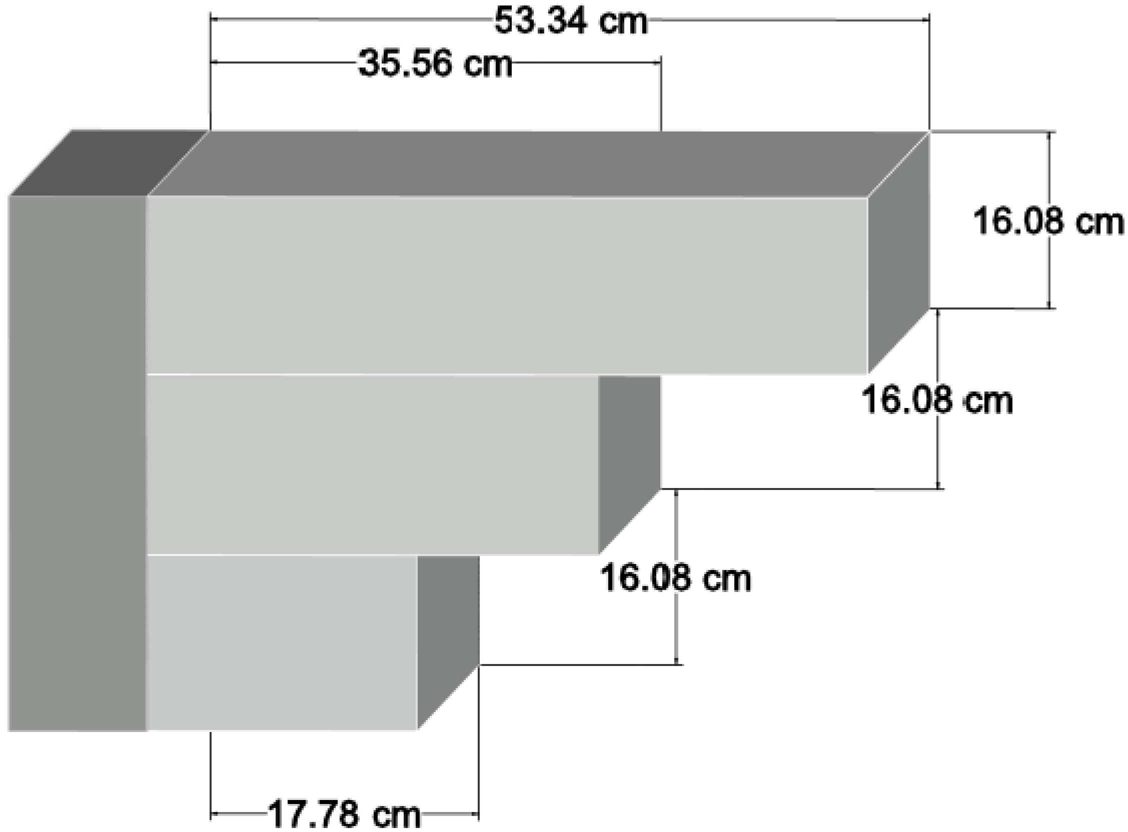

Figure 3-5 Inverse Wedge Configuration

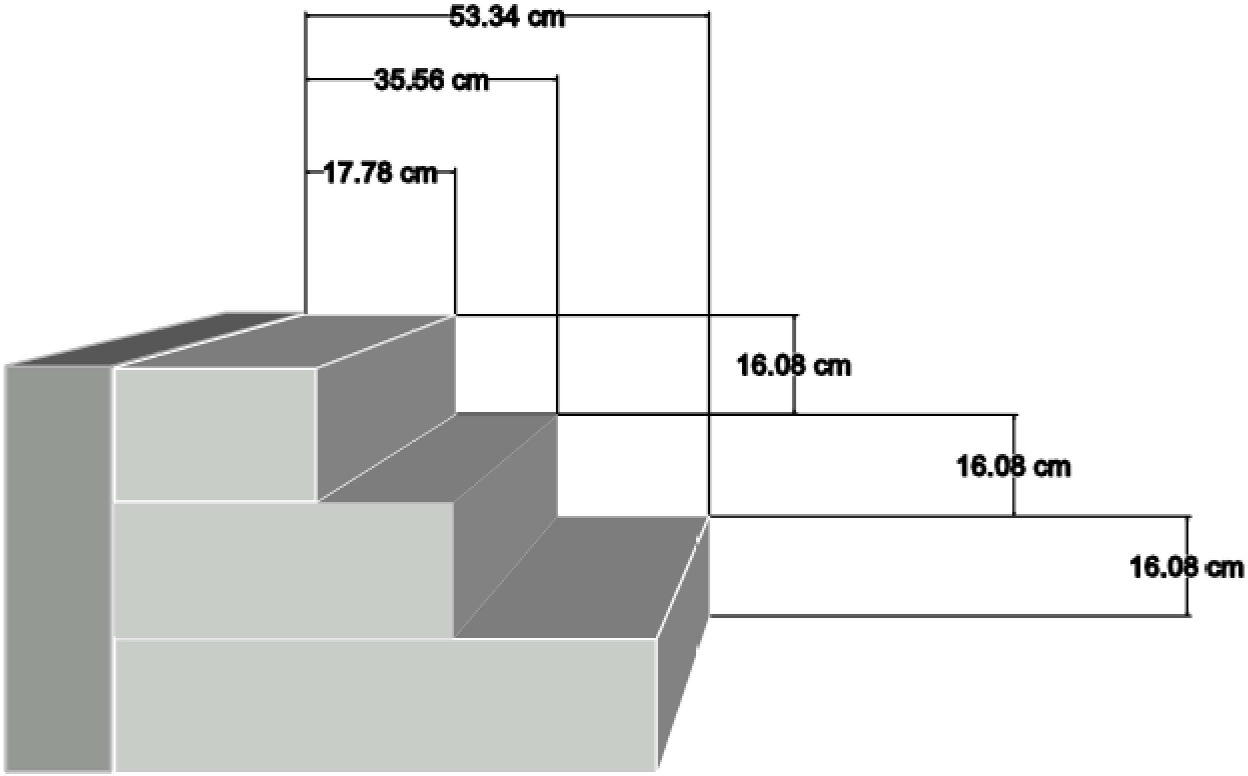

Test T6 and T7 incorporate an EPS sheet, which is 10.16 cm wide, 109.22 cm long and 48.24 cm high. Soft EPS geofoam inclusions were used in tests T8, T9, and T10, each 5.08 cm wide, 109.22 cm long and 48.24 cm high. Test T8 uses the EPS soft geofoam sheet with five layers of geogrid, T9 employs EPS soft geofoam sheet with five layers of geotextile, and test T10 incorporates EPS soft geofoam foam sheets with eight layers of geotextile.

3.3.2 Geogrid

Tests T5 and T8 both incorporate biaxial geogrids, which has the apertures size of 2.54 cm x 2.54 cm in the experiments. The properties of the geogrids are outlined in Table 3-3.

Table 3.3 Geogrid Properties

Geotextile	Direction	Unconfined Tensile Strength (kN/m)
Miragrid® 2XT	Machine Direction	29.2
	Cross-Machine Direction	29.2

In test T5 the geogrid was placed in 5 layers and geotextile was wrapped around the edge facing next to the abutment. The first four layers are placed with a bottom length of 50 cm, a vertical spacing of 9.65 cm and a lap length of 20cm. The top layer also as a bottom length of 50 cm and a vertical spacing of 9.65 cm, however, the lap length is 40 cm. It is this longer lap length that allows for 10 cm of the geotextile to rest at the level of the top of the abutment, followed by 10 cm buried beneath the top at approximately 45° angle, and covered with sand. The remaining 20 cm of geotextile was buried under 5 cm of soil. A 30 cm long piece of geotextile was wrapped around the facing of the four bottom lifts to prevent the soil from falling out. A soft density EPS geofoam was used in test T8 along with the geogrid and geotextile for wrapping as described in test T5.

3.3.3 Geotextile

The Pellon Tru-Grid was used as the geotextile in experiments T4, T9, and T10. In test T4, the geotextile was arranged in five layers. The first four layers had bottom length of 50 cm, a vertical spacing of 9.65 cm, and a lap length of 20cm. The top layer shared the same dimensions for its bottom length and vertical spacing, but with a lap length of 40 cm. This top layer is configured so that 10 cm of geotextile rests at the level of the top the top of the backfill, followed by 10 cm buried in the sand and inclined at approximately at 45° angle, followed by remaining 20 cm that is buried under 5 cm of sand.

In test T9, a similar arrangement of five layers of geotextile is employed. The first four layers maintain a bottom length of 50 cm, a vertical spacing of 9.65 cm, and a lap length of 20 cm. The top layer, however, has a bottom length of 60 cm, a vertical spacing of 9.65 cm, and a lap length of 50 cm. This top layer is position so that 20 cm of geotextile is at the level of the top of the backfill, followed by 10 cm of geotextile buried at approximately at 45° angle, and the remaining 30 cm buried under 5cm of sand.

In test T10 the geotextile is placed in eight layers. The first seven layers each have a bottom length of 50 cm, a vertical spacing of 6.0 cm and a lap length of 40 cm. The top layer had a bottom length of 50 cm, a vertical spacing of 6.0 cm and lap length of 40 cm. The top layer was configured in such a way that the 10 cm of geotextile is placed at the level of the top of the backfill, followed by 10 cm of fabric that is buried underneath the layer at approximately 45° angle with sand being placed on top. The remaining 20 cm of geotextile was then buried underneath the 5 cm of soil.

3.3.4 Camera

The camera selected for the experiment was a Sony Cyber-Shot 20.9-megapixel DSC-RX10 IV camera. This camera provides an effective picture size of 20.1 megapixels, thus allowing for a 5472-pixel x 3648-pixel pictures. The camera was setup 1.27 m away from the container, and it captured the entire soil enclosure. It took one photo per each ±3 mm displacement of the abutment, thus resulting in a total of four photos per cycle.

3.3.5 VIC-2D

VIC-2D, a commercial digital imaging correlation software was used in this study. The program allows for customization and adaptation to a particular experiment. The area of interest feature allows the program to select the area that is going to be analyzed. Within the area VIC-2D locates a subset of L x L pixels, and identifies and follows that subset based on the contrast and noise present in the digital photographs. Specifically, it takes that subset of pixels and a search area that is bigger than the subset while creating a search window. Within that search window VIC-2D searches subset by subset of pixels until it finds a displacement match indicating how much that subset of pixels has moved. Based on the displacements VIC-2D can calculate several different types of strain.

Chapter 4 - Results

4.1 Earth Pressure Calculations

Before presenting experimental results theoretical values of earth pressures acting on abutment were calculated including at rest pressure, and active and passive pressures according to Rankine and Coulomb theories.

Lateral earth pressure at rest for normally consolidated soil is given by,

$$P_o = \frac{1}{2}\gamma' H^2 K_{o(NC)} L \tag{4.1}$$

where γ' is the effective unit weight of the backfill, which is equal to 18.05 kN/m^3, H is the height of the abutment equal to 0.483 m, L is the length of the abutment equal 1.09 m, and $K_{o(NC)}$ is the coefficient of lateral earth pressure at rest according to Jaky (1944) that is given by,

$$K_{o(NC)} = 1 - \sin(\phi') = 1 - \sin(42.2°) = .328 \tag{4.2}$$

and ϕ' is the soil's effective friction angle, equal to 42.2°. Equation 4.1 results in a P_o equal to .751 kN with a $K_{o(NC)}$ calculated to be .328 based on equation 4.2. It is estimated that coefficient of lateral earth pressure at rest for overconsolidated soil $K_{0(OC)}$ is given by

$$K_{o(OC)} = K_{o(NC)} OCR^m \tag{4.3}$$

where *OCR* is the overconsolidation ratio. Mayne and Kulhawy (1982) suggested that

$$m = \sin\phi' \tag{4.4}$$

Equation 4.3 gives $K_{0(OC)}$ values of 0.522 and 0.832 for *OCR* values of 2 and 4 with corresponding values of lateral earth pressure at rest resultants of 1.20 kN and 1.91 respectively.

The resultants of lateral earth pressures in active and passive failure states are also calculated. According to Rankine's theory the coefficient of active earth pressure is given by

$$K_a = tan^2\left(45° - \frac{\phi'}{2}\right) \tag{4.5}$$

and the coefficient of passive earth pressure is given by,

$$K_p = tan^2\left(45° + \frac{\phi'}{2}\right) \tag{4.6}$$

The resulting K_a and K_p from equations 4.5 and 4.6 with a ϕ' of 42.2° are 0.196 and 5.09 respectively. The corresponding resultants of active and passive pressures according to Rankine's theory are given by

$$P_a = \frac{1}{2}K_a\gamma H^2 L \tag{4.7}$$

and

$$P_p = \frac{1}{2}K_p\gamma H^2 L \tag{4.8}$$

Finally, P_a and P_p values of 0.449 kN and 11.66 kN are obtained from equations (4.7) and (4.8) respectively.

Equation 4.8 provides the active pressure coefficient according to Coulomb's theory of earth pressure.

$$K_a = \frac{sin^2(\beta + \phi')}{sin^2(\beta)\sin(\beta - \delta')\left[1 + \sqrt{\frac{\sin(\phi' + \delta')\sin(\phi' - \alpha)}{\sin(\beta - \delta')\sin(\alpha + \beta)}}\right]^2} \tag{4.9}$$

where β is the angle the of the abutment back-face with respect to the horizontal, δ' is the interface friction angle between the abutment and backfill, and α is the inclination of the backfill above the horizontal above at the level of the abutment top. According to Das and Sivakugan (2018), δ' is typically assumed to be between ½ ϕ' and ⅔ ϕ', resulting in δ' values of 21.1° and 28.1° respectively. Equation 4.6 results in K_a values of 0.181 and 0.182 for a vertical abutment (β

= 90°) with horizontal backfill (α=0°) and δ' values of 21.1° and 28.1° respectively. The corresponding value of active Coulomb's force resulting from the active pressure

$$P_a = \frac{1}{2} K_a \gamma H^2 L \tag{4.10}$$

where K_a is the active pressure coefficient given by Coulomb's theory of active pressure. Equation 4.10 results in a force of 0.415 kN and 0.417 for K_a values of 0.181 and 0.246 respectively.

Equation 4.11 provides the passive pressure coefficient according to Coulomb's theory earth pressure.

$$K_p = \frac{sin^2(\beta - \phi')}{sin^2(\beta)\sin(\beta + \delta')\left[1 - \sqrt{\frac{\sin(\phi' + \delta')\sin(\phi' + \alpha)}{\sin(\beta + \delta')\sin(\alpha + \beta)}}\right]^2} \tag{4.11}$$

Equation 4.11 results in K_p values of 15.0 and 26.5 for δ' values of 21.1° and 28.1° respectively. The resulting passive Coulomb's force resulting is given by

$$P_p = \frac{1}{2} K_p \gamma H^2 L \tag{4.12}$$

where K_p is the passive pressure coefficient given by Coulomb's theory of passive pressure. Equation 4.12 provides Coulomb's passive force of 34.4 kN and 60.7 kN for K_p values of 15.0 and 26.5 respectively.

Finally, the inclination of the Coulomb's active and passive forces from the horizontal direction is equal to the abutment-backfill interface friction angle. The horizontal components of P_a and P_p are given by

$$P_a^H = P_a \cos(\delta') \tag{4.13}$$

and

$$P_p^H = P_p \cos(\delta') \tag{4.14}$$

thus, resulting in P_a^H of 0.387 kN for a P_a of 0.415 kN and a δ' of 21.1º, and a P_a^H of 0.368 kN for a P_a of 0.417 kN and a δ' of 28.1°. The resulting P_p^H calculated from equation 4.14 is 32.09 kN for a P_p of 34.4kN and a δ' of 21.1° and 53.54 kN for a P_p of 60.7kN and a δ' of 28.1°.

4.2 Test T1: Reference Test

The load cell, model Artech Industries- 20210-2000, which was used to measure the horizontal force applied to abutment, was connected to the abutment and screw jack in an assembly that prevented transfer of moment. Additional instrumentation included two LVDTS, model: ELE International ALM/SGD-15mm, out of which, one was placed in front of the abutment and used to measure the horizontal displacement at the top of the abutment and another one was used to measure vertical soil displacement behind the abutment. During test T1, initial measured the at-rest force acting on abutment was equal to 0.739 kN. The abutment was subjected to cyclic loading via moving the screw jack backward and forward in the amount of 3 mm. Figure 4-1 shows test T1 configurations prior to the beginning of test T1 with the abutment in a neutral position.

Figure 4-1 Configuration Prior to the Beginning of Experiment, Test T1

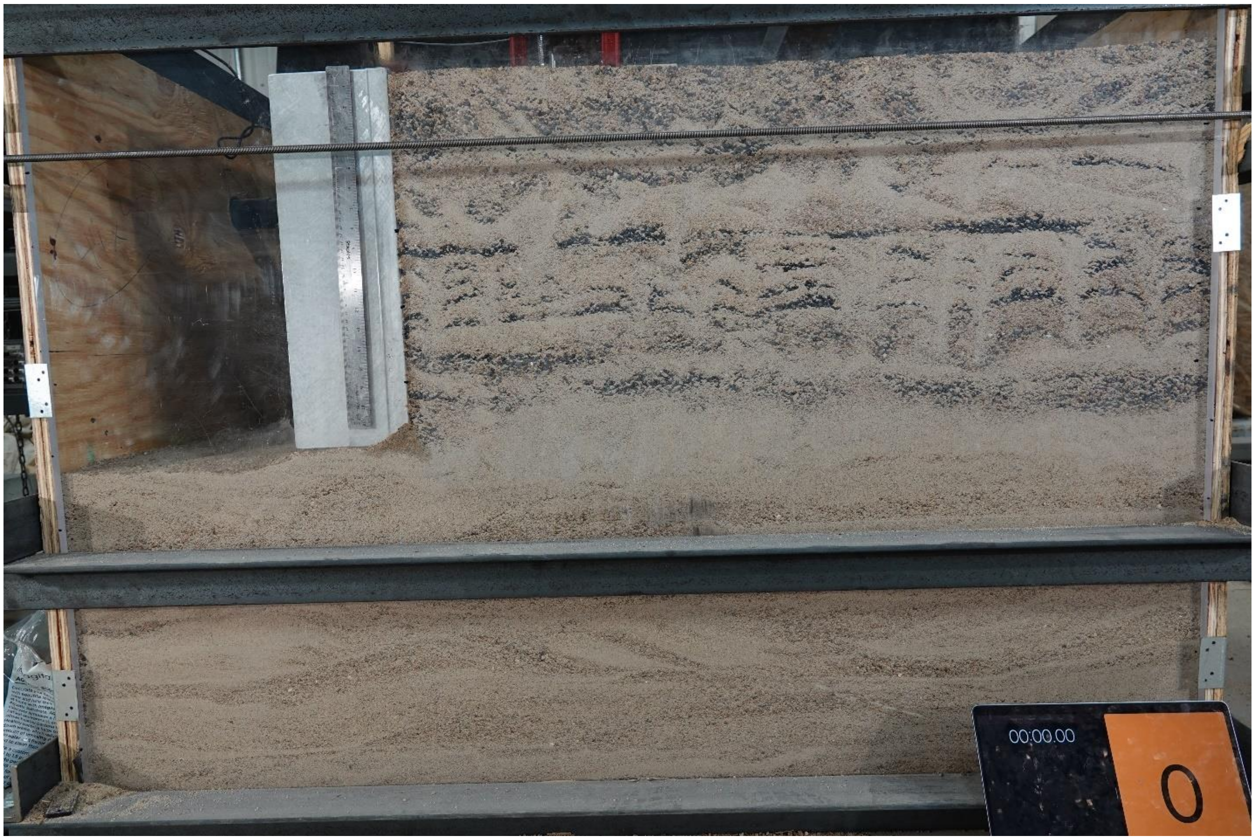

Figure 4-2 shows the measured horizontal force vs horizontal displacement at the top of the abutment where compressive force is positive and the abutment's displacement away from the backfill is positive. The maximum force recorded force was equal to 10.62 kN and it corresponds to the maximum abutment's displacement towards the backfill. This value is smaller than all previously calculated values of passive failure force including Rankine's and horizontal components of Coulomb's for $\delta' = 21.1°$ and $\delta' = 28.1°$ passive force.

Transparent long thin plastic guards were attached to the abutment edge in test T1 or edge of the EPS geofoam used in other test to prevent flow of sand between the abutment or EPS geofoam and the plexiglass wall. Plastic guards are not clearly visible in figures as they were placed perpendicular to the plexiglass wall. Due to the friction induced by these guards the force measurements presented here are not exactly equal to the resultant of earth pressures acting behind the abutment. Nevertheless, resultant of earth pressures acting on the abutment during its motion towards the backfill is smaller than the measured force due to the direction of friction. Consequently, passive failure was not reached in the backfill soil behind abutment in test T1.

The minimum measured value of the force acting on the abutment is negative indicating that magnitude of Rankine's and Coulomb's active forces is larger than the friction. In addition, as the maximum measured force continues to further increase with increasing number of cycles while the minimum measured force remains approximately constant. For example, the maximum measured force in the 1st cycle was 5.99 kN, but by the 91st cycle it increased to 10.36 kN.

Figure 4-2 Horizontal Force vs. Horizontal Displacement, Test T1

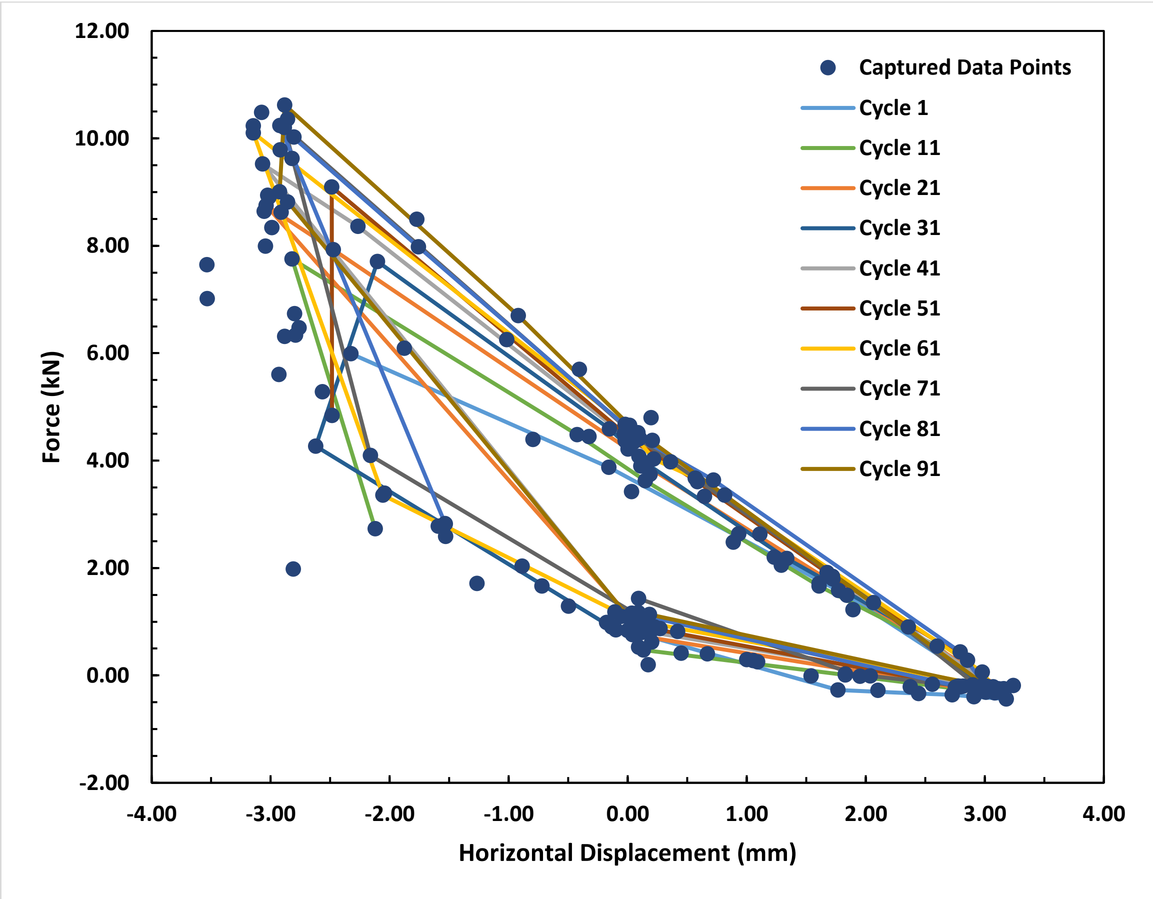

Although the intended abutment's displacement rate is 24mm/min the captured displacement rate and magnitude usually slightly deviate from intended values due to the manual movement of the screw jack. Figure 4-3 below shows the intended displacement magnitude and rate vs the captured data while Figure 4-4 shows the photograph taken at the end of test T1.

Figure 4-3 Intended Displacement History vs. Captured Data, Test T1

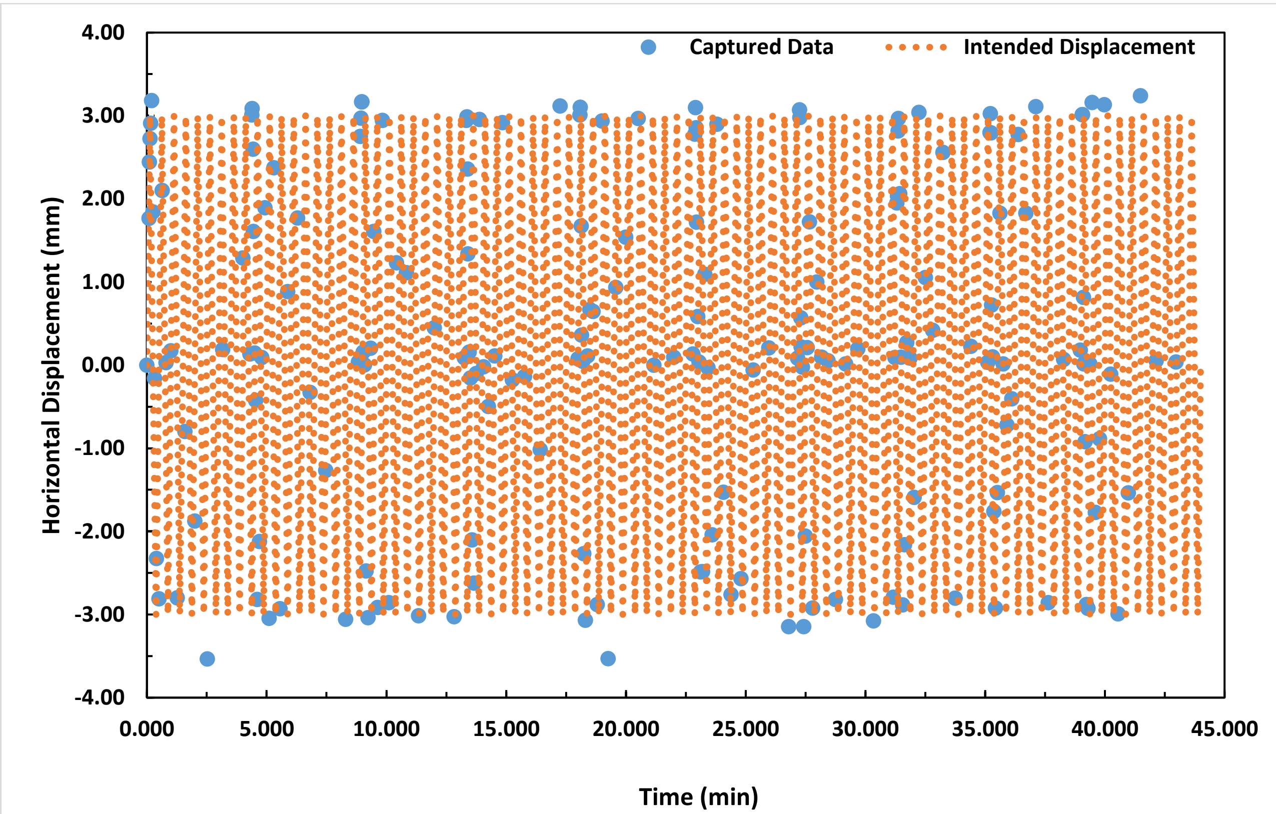

Figure 4-4 clearly shows the near surface backfill soil collapse behind the abutment that evolved throughout 100 cycles This collapse results in gradual loss of soil support for an approach slab that is usually placed above the backfill soil, but not included in this investigation. A progress of backfill settlement at the interface of the abutment and soil is shown in Figure 4-5, resulting in 81.9 mm of settlement after 100 loading cycles.

Figure 4-4 Configuration at End of Experiment, Test T1

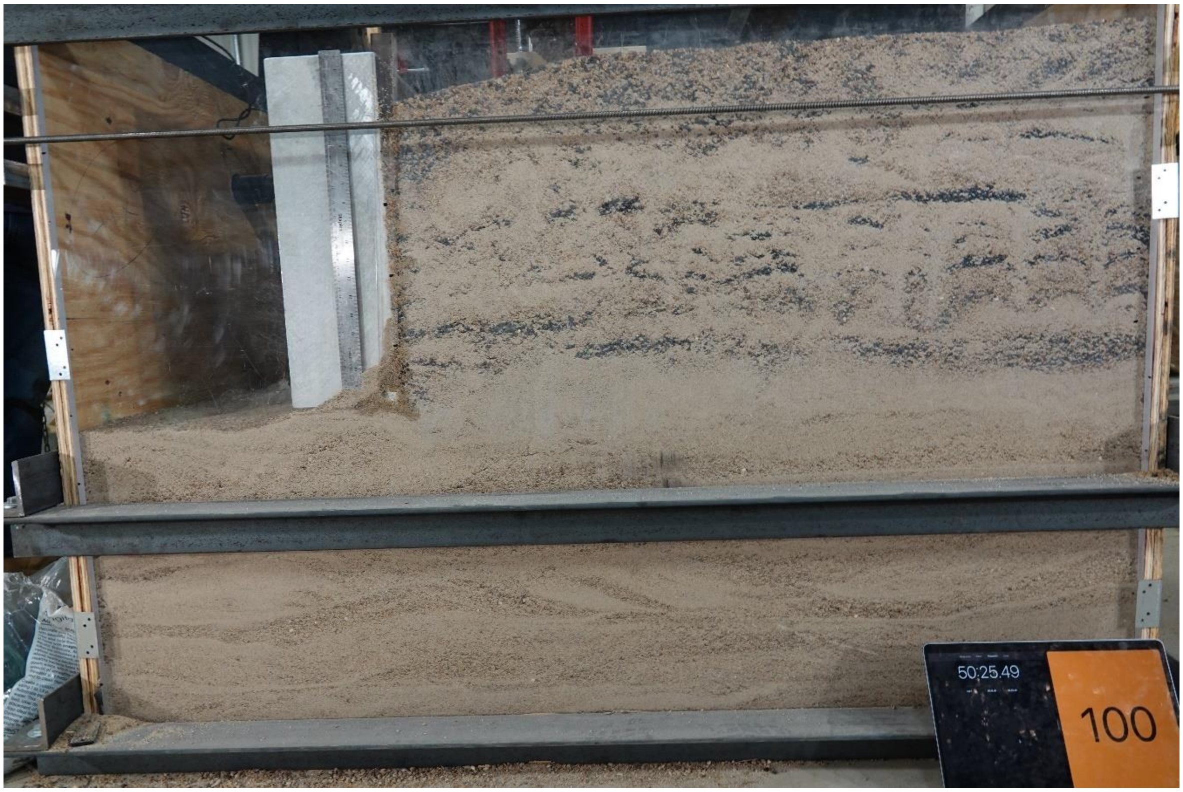

Figure 4-5 Cycle Number vs. Settlement, Test T1

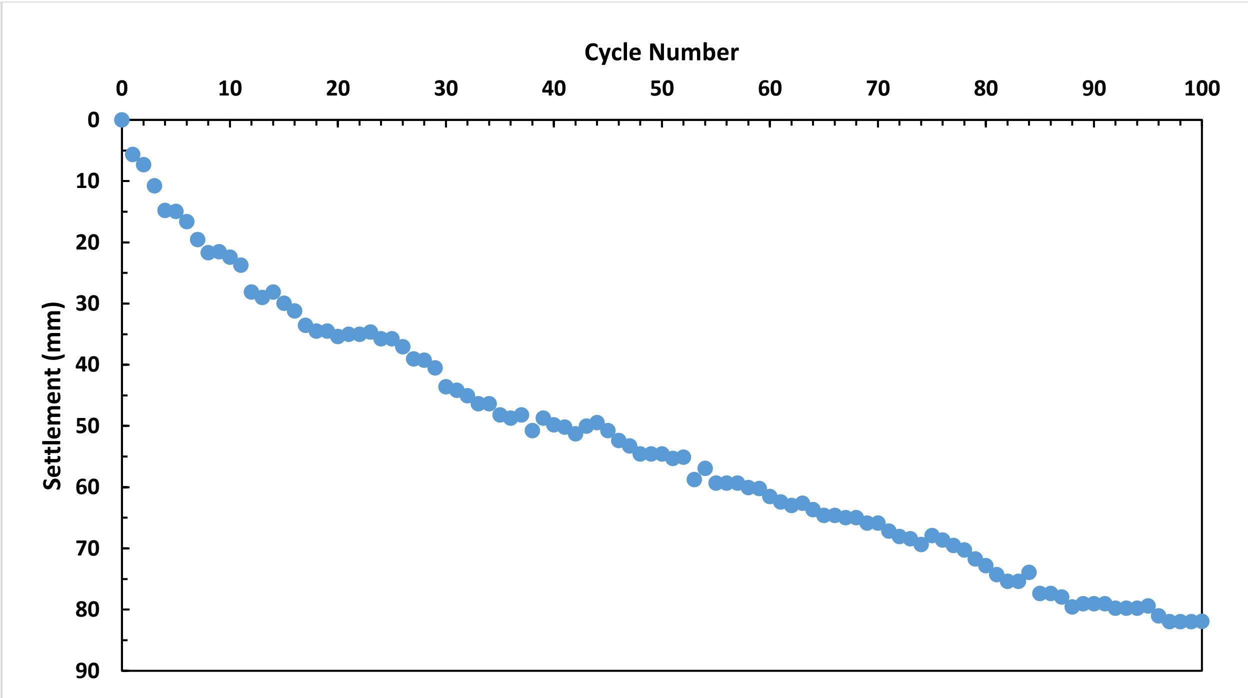

Figure 4-6 shows the Lagrangian shear strain (ε_{xy}) strain, where the Cartesian coordinate system x,y is located in the plane of the picture. All Lagrangian shear strains were obtained from the photographs taken during testing and using DIC software VIC-2D, and the one shown in Figure 4-6 develops between initial undeformed configuration and the very first outward movement of the abutment top of magnitude 3 mm. Clearly, this figure shows a shear band within the backfill material demonstrating that the backfill reached the state of active failure at the beginning of the very 1st cycle. The shear band is inclined at the angle of 68° towards the horizontal direction. The maximum shear strain (ε_{xy}) in the shear band is 1.08%. Another interface shear band is also noticeable along the contact of the abutment and backfill with maximum magnitude of shear strain of 0.72% The interface shear band develops due to falling sand and the resulting large shear strain. The vectors shown in Fig 4-6 show displacements indicating that the backfill located within the active wedge moves as expected, downwards and to the left.

Figure 4-7 shows Lagrangian shear strain developing between the initial undeformed configuration and the beginning of the 5th cycle, i.e., + 3mm displacement at the beginning of the 5th cycle. As shown, ε_{xy} within the shear band has increased although the shear band has become shorter, and several regions of large shear strain develop in the near surface region.

Figure 4-6 Lagrangian Strain (ε_{xy}) Neutral to Active Position, Cycle 1, Test T1

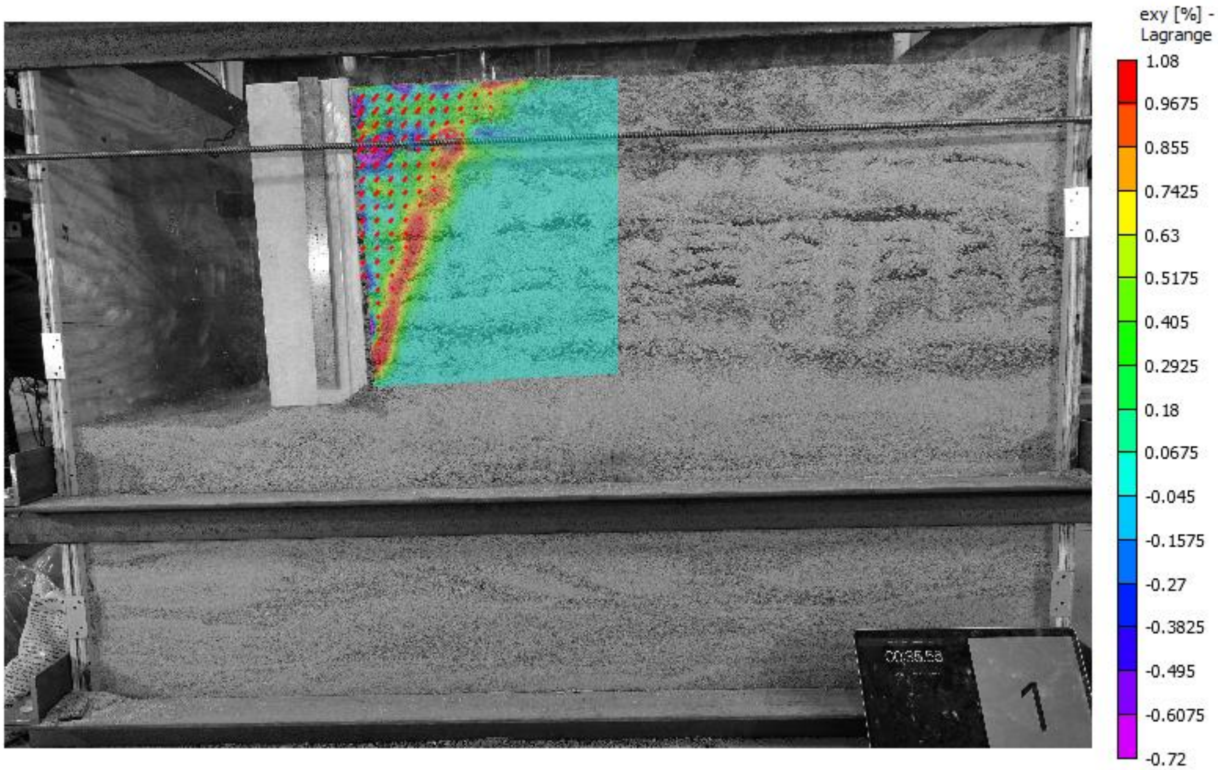

Figure 4-7 Lagrangian Strain (ε_{xy}), Neutral to Active Position, Cycle 5, Test T1

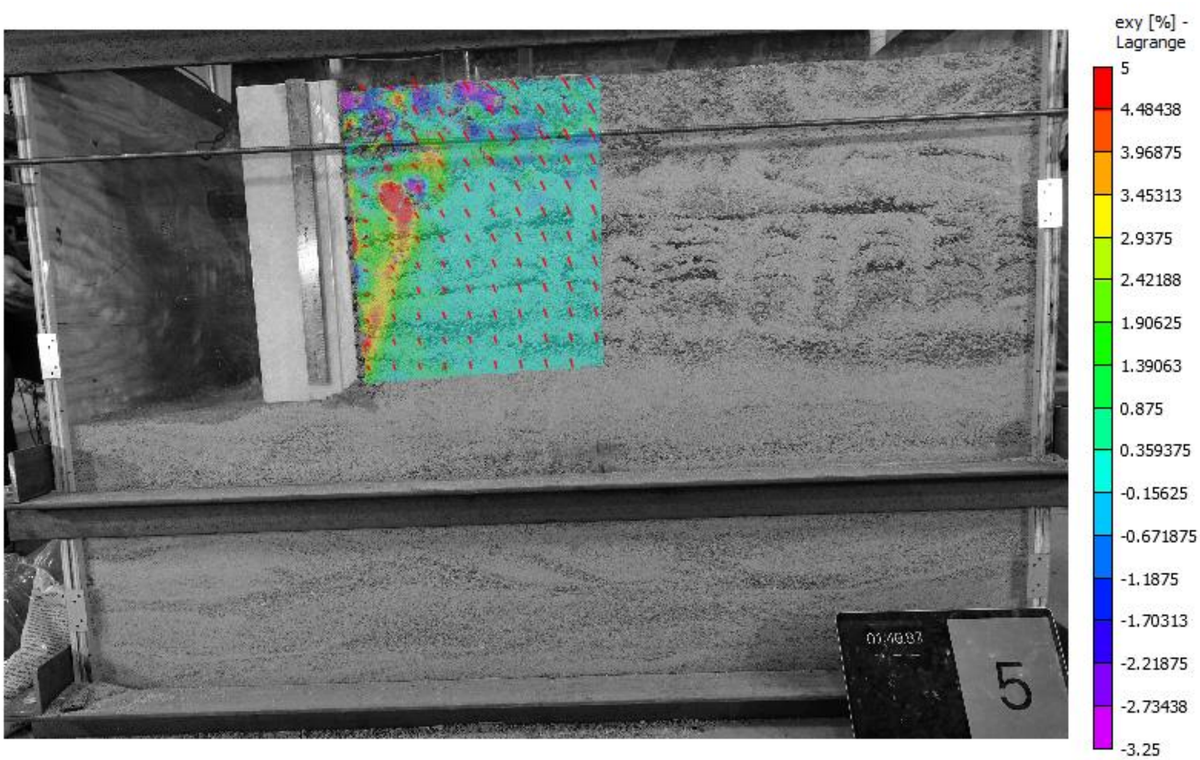

4.3 Test T2: Stiff EPS Wedge

In test T2, a stiff EPS geofoam wedge was placed behind the abutment. As shown in Figure 4-8 the maximum force measured in this test was 6.49 kN, which is less than the one measured in test T1 by 3.87 kN. This reduction can clearly be attributed to the EPS geofoam wedge. The minimum measured force compared to the minimum force in test T1 did not change significantly. Figure 4-8 also shows that the maximum force in each loading cycle increases with the increasing number of cycles until it reaches a maximum force of 6.49 kN by cycle 51. Intended and captured displacement history is shown in Figure 4-9.

Figure 4-8 Horizontal Force vs. Horizontal Displacement, Test T2

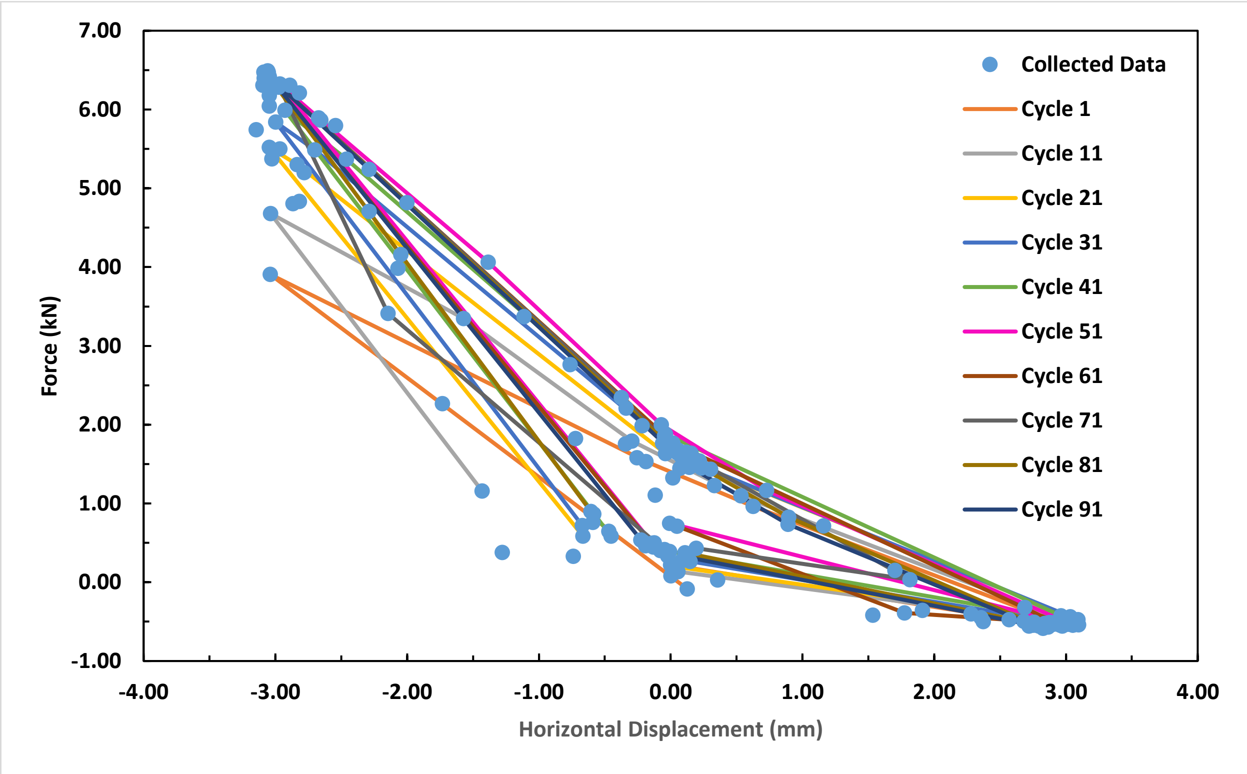

Figure 4-9 Intended Displacement History vs. Captured Data, Test T2

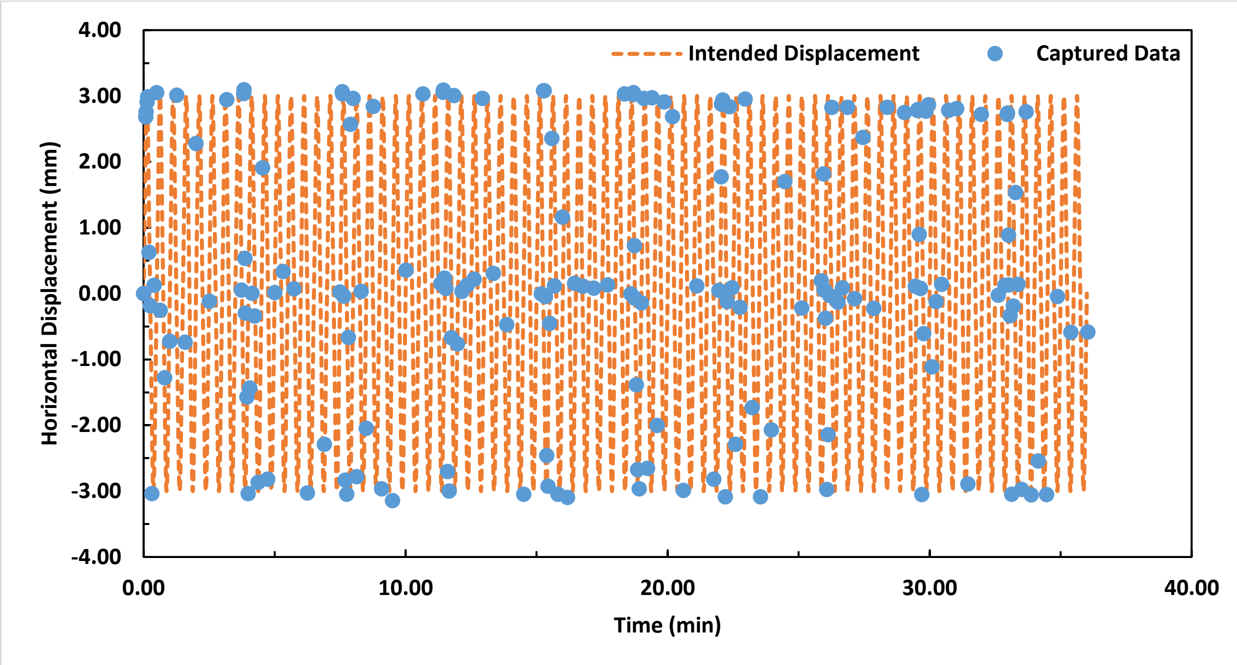

Figure 4-10 shows the configuration with the EPS wedge and the backfill within the soil enclosure before the beginning of test T2. Figure 4-11 depicts the state at the end of the 100th cycle, illustrating the backfill collapse that now occurs at three different levels, behind the top, middle and bottom layers of the EPS geofoam, with the latter being barely noticeable. The settlement at the interface of the top EPS geofoam layer and the backfill soil was 40.81 mm, while the settlement behind the middle and bottom EPS geofoam layers was 36.43 and 13.25 mm respectively. Interestingly, the sum of these settlements that occur at three different levels is equal to 80.49 mm, which is very close to the surface settlement in reference test T1 that is equal to 81.9 mm. Nevertheless, the surface settlement in test T2 is equal to only 40.81 mm at the end of the 100th cycle. Figure 4-12 shows the progress of surface settlement with increasing number of loading cycles. The rate of settlement vs. cycle number is approximately constant in test T2, unlike in test T1 where it gradually decreases with increasing number of cycles.

Figure 4-10 Configuration Prior to the Beginning of Experiment, Test T2

Figure 4-11 Configuration at End of Experiment, Test T2

Figure 4-12 Cycle Number vs. Settlement, Test T2

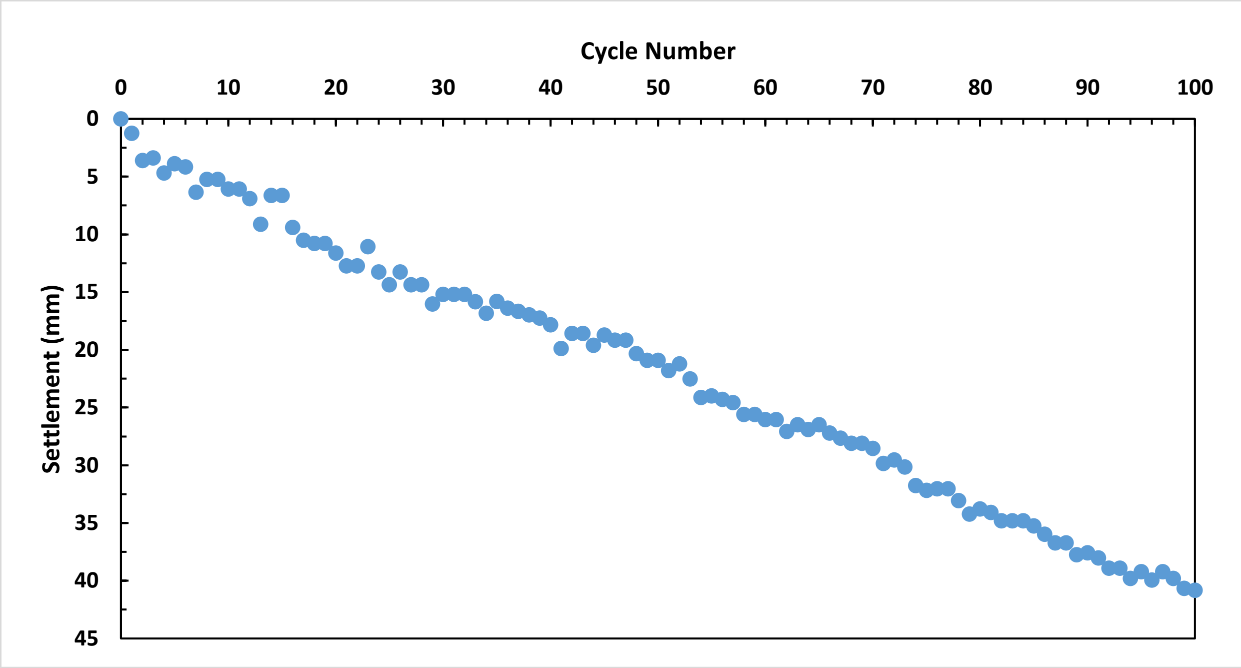

Figure 4-13 below shows the computed Lagrangian shear strain (ε_{xy}) between initial undeformed configuration and the first + 3mm abutment top movement. Figure 4-13 clearly shows two shear bands corresponding to the development of active failure behind the top and middle EPS geofoam layers while the inception of the shear band behind the bottom layer of EPS geofoam is barely noticeable. Additionally, interface shear bands develop at the interface of EPS geofoam vertical and horizontal surfaces with the soil. Magnitude of maximum shear strain in inclined shear bands is 1.33% while the magnitude of maximum shear strain inside the interface shear bands is 1.04%. Similarly, to test T1, each shear band is accompanied with soil collapse where the collapse next to the top EPS geofoam layer is the near surface collapse. The collapses taking place behind the middle and bottom EPS geofoam layers are not surface collapses and they do not cause surface settlement.

Figure 4-14 below shows Lagragian shear strain (ε_{xy}) that develops between initial undeformed configuration and the beginning of the 5th cycle. It indicates that the pattern of shear strain behind the middle and bottom EPS geofoam layers becomes more dispersed, while two shear bands, inclined and vertical with maximum shear strain of about 8.38% remain present behind the top EPS geofoam layer.

Figure 4-13 Lagrangian Strain (ε_{xy}), Neutral to Active Position, Cycle 1, Test T2

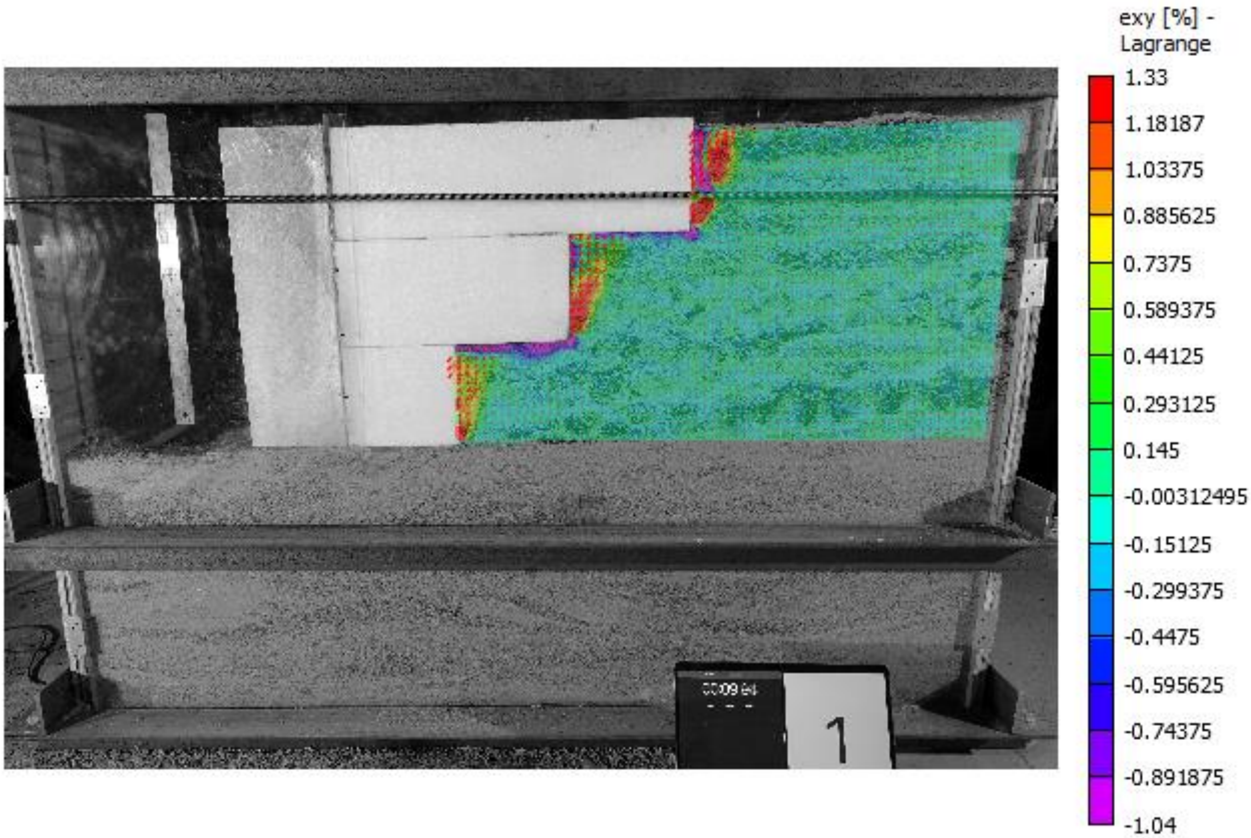

Figure 4-14 Lagrangian Strain (ε_{xy}), Neutral to Active Position, Cycle 5, Test T2

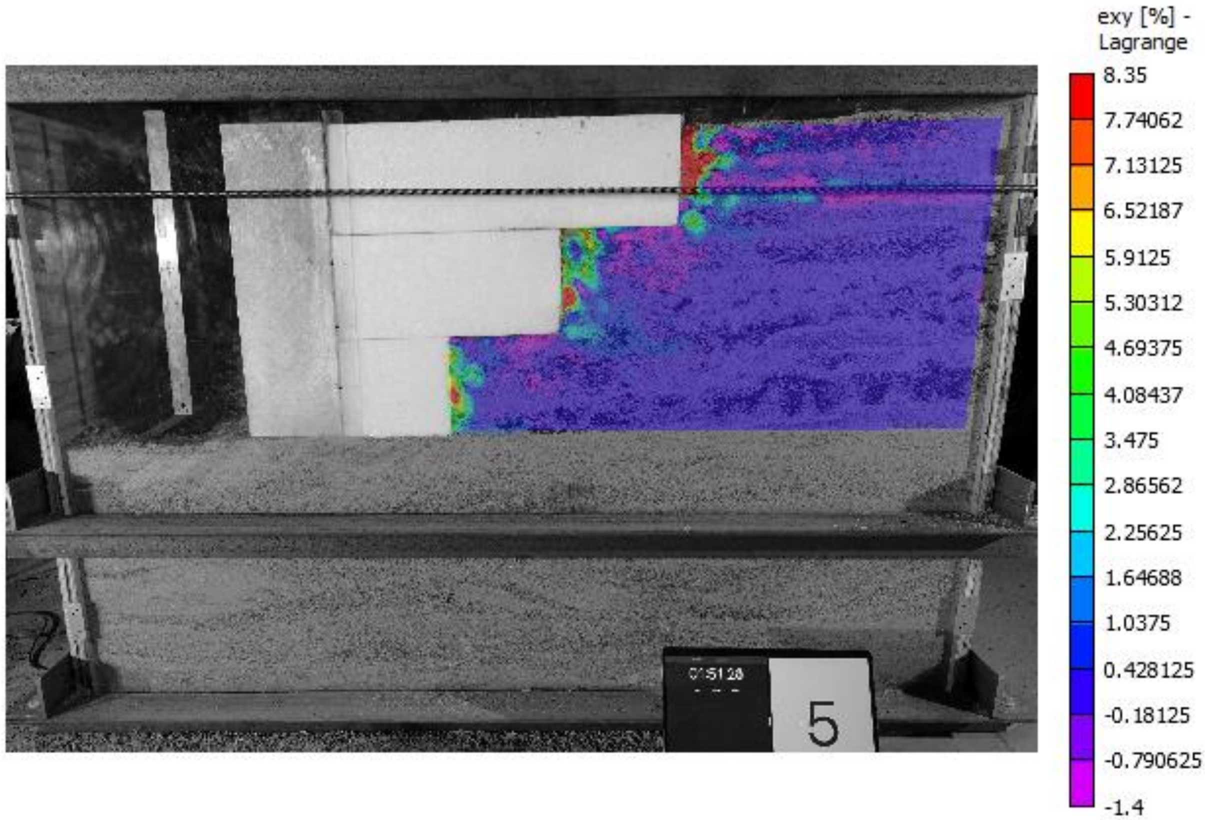

4.4 Test T3: Stiff Inverse Wedge

In test T3, an inverse stiff wedge-shaped EPS Geofoam inclusion was used. As seen in Figure 4-15 the maximum compressive horizontal force measured in the 1st cycle was 3.36 kN and by the 91st cycle it increased to 4.68 kN. The intended vs. captured displacement history is shown in Figure 4-16.

Figure 4-15 Horizontal Force vs. Horizontal Displacement, Test T3

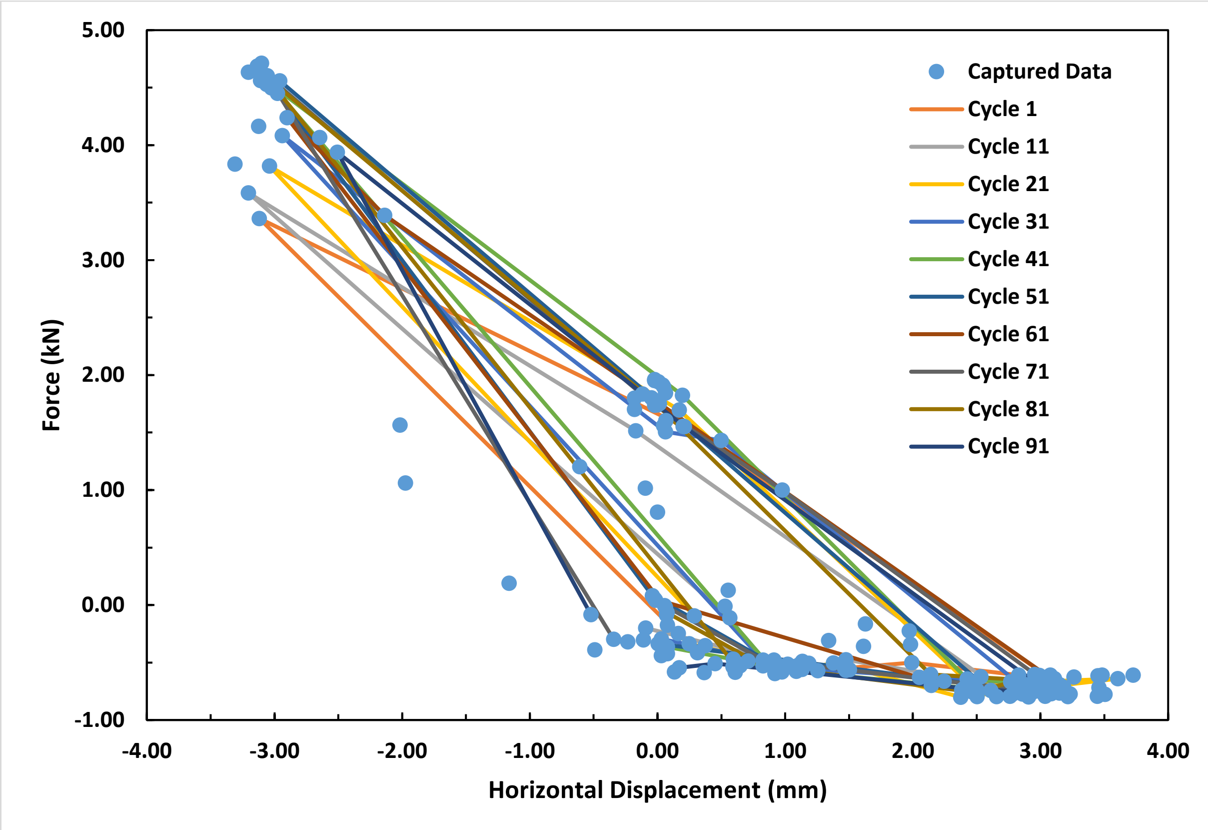

Figure 4-16 Intended Displacement History vs. Capture Data, Test T3

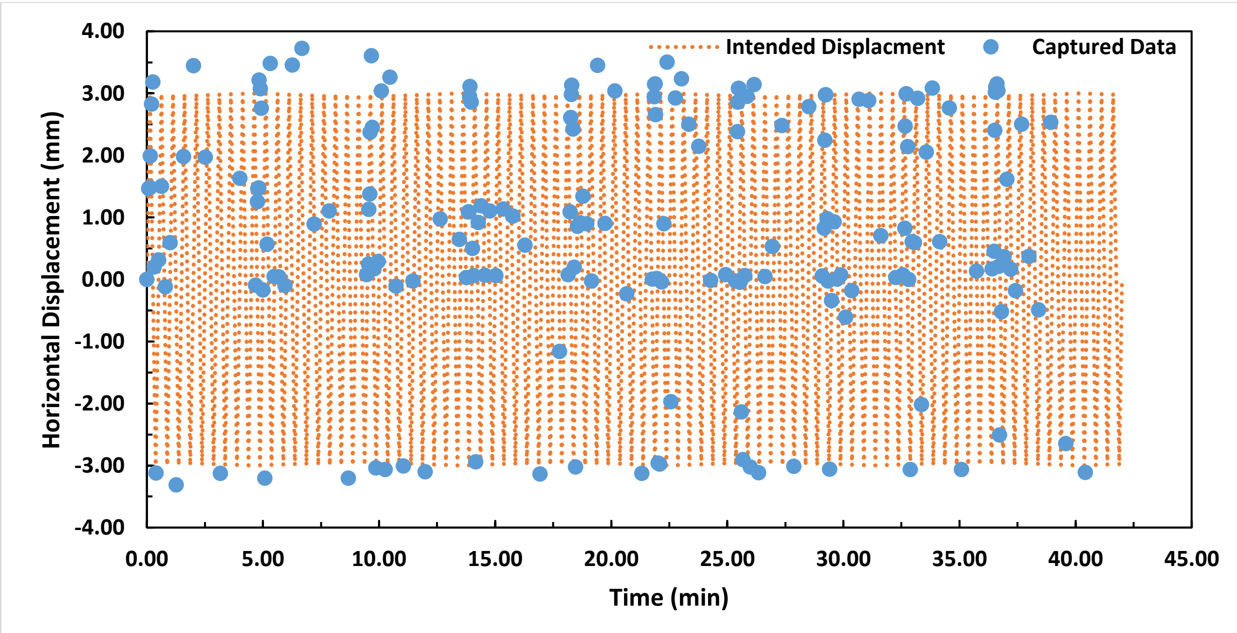

Figure 4-17 shows the test configuration including the inverse EPS geofoam wedge and the backfill within the enclosure. Figure 4-18 captures the surface of the backfill at the end of the 100th cycle, thus illustrating the culmination of the near surface collapse. Unlike in test T2, in this case settlement occurs only next to the top EPS geofoam layer, and it is equal to 70.3 mm at the end of the 100th cycle. In addition, settlement trend is similar to the one observed in test T1 where rate of settlement gradually decreases with increasing number of cycles, except in the vicinity of the 100th cycle.

Figure 4-17 Configuration Prior to Beginning of Experiment, Test T3

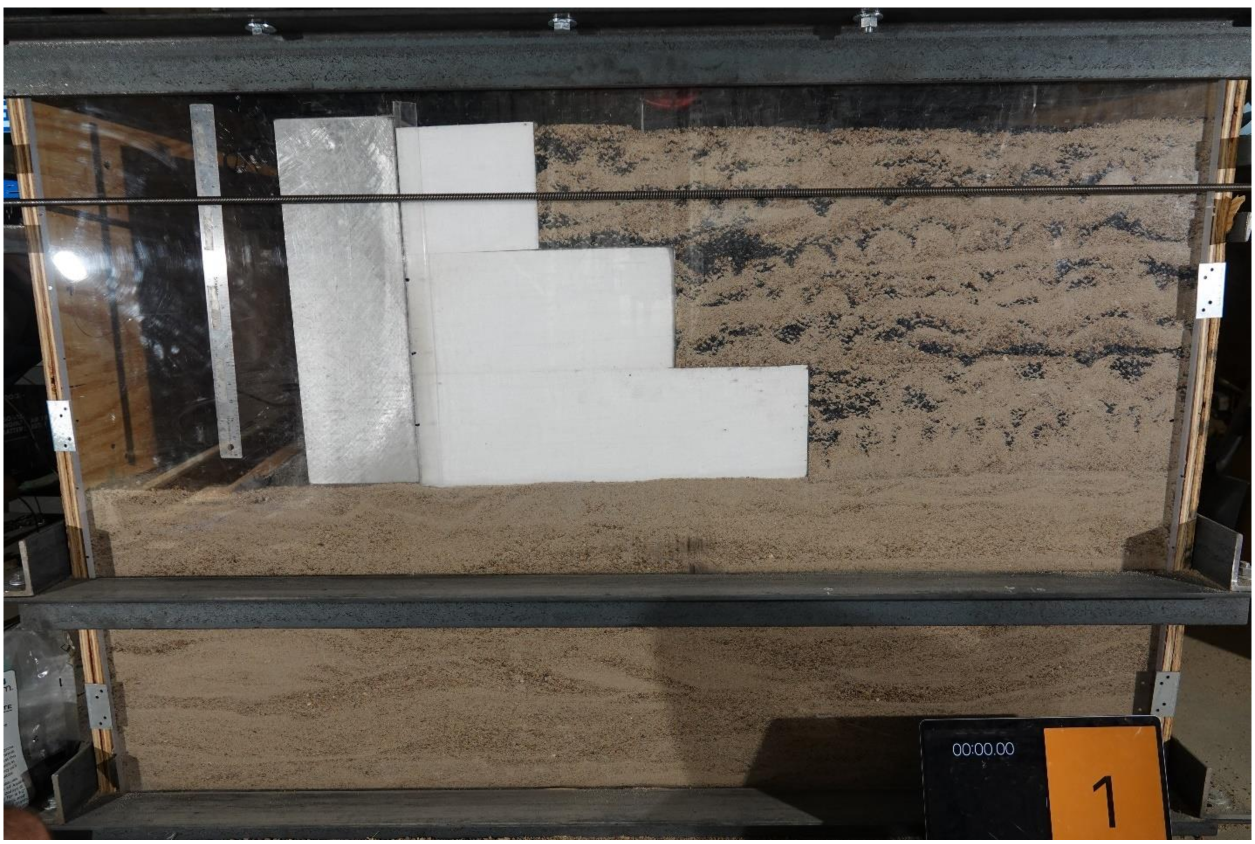

Figure 4-18 Configuration at the End of Experiment, Test T3

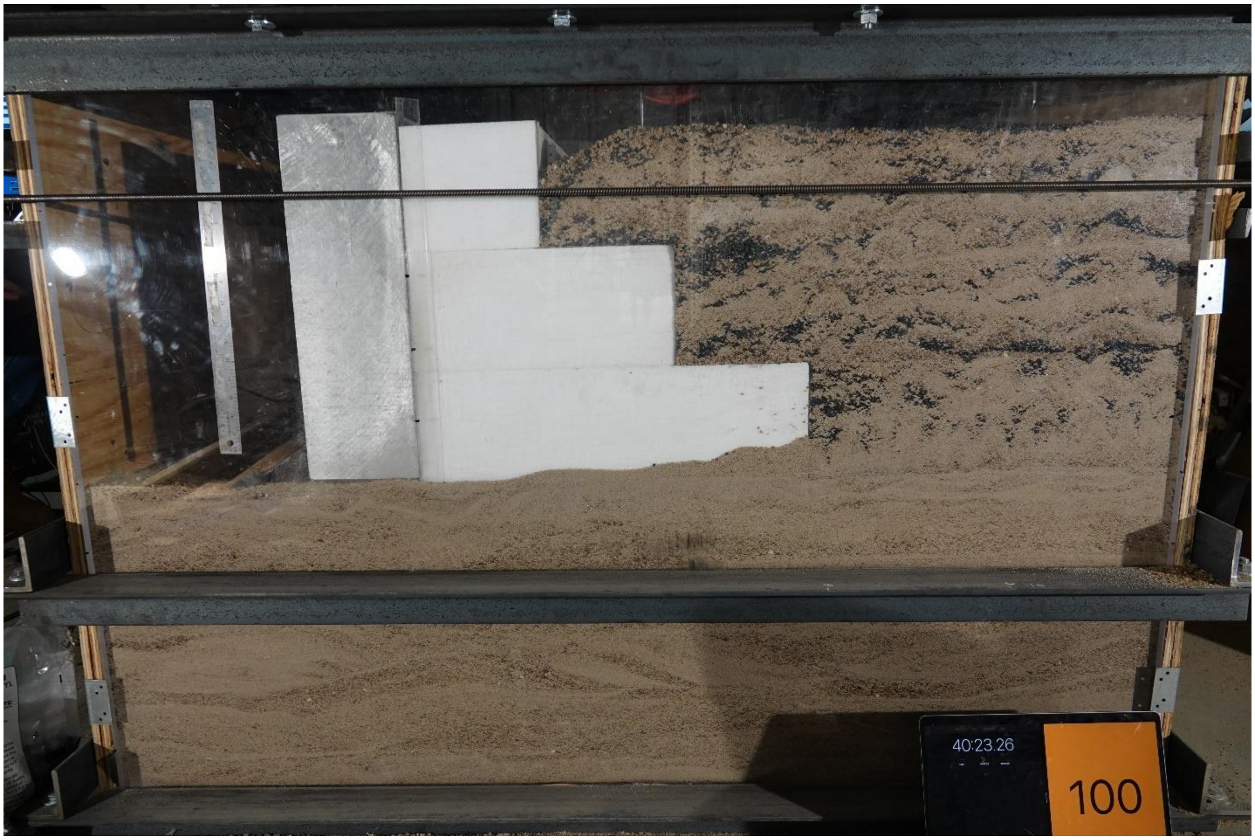

Figure 4-19 Cycle Number vs. Settlement, Test T3

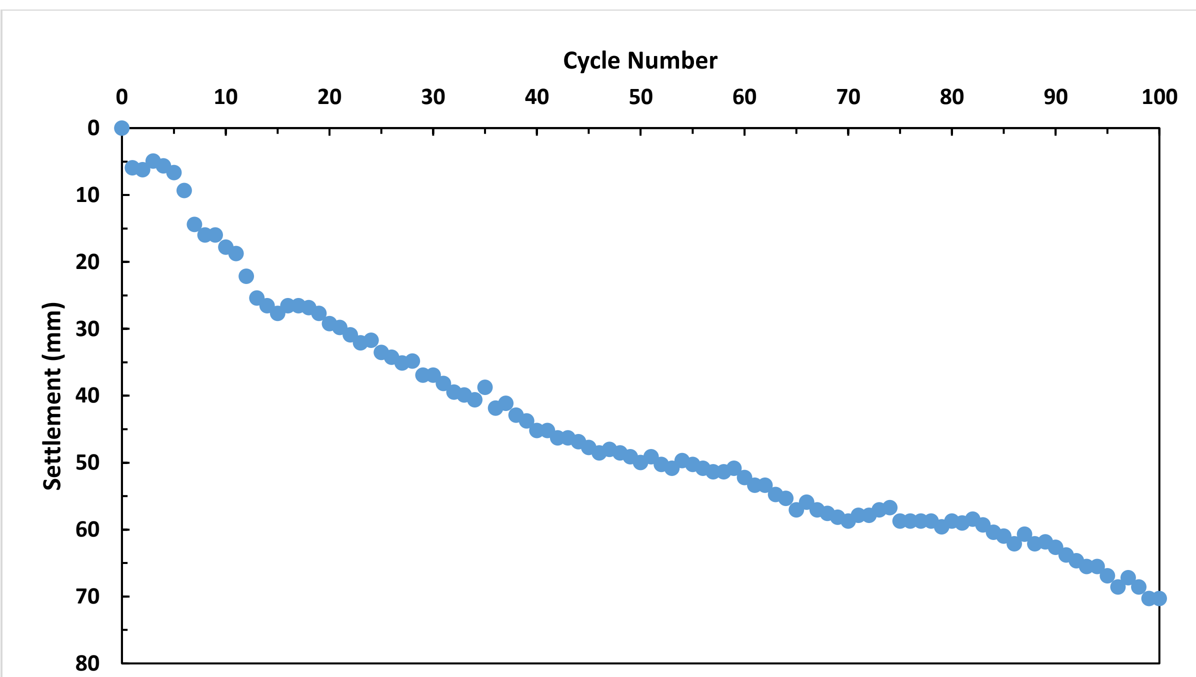

Figure 4-20 displays the Lagrangian shear strain computed by VIC-2D during the very first movement of the abutment away from the backfill. The maximum shear strain that develops in this stage is equal to 0.36%, but that magnitude is not significantly different from the shear strains developing in the surroundings. The intensity of strain localization increases during the beginning of the 5th loading cycle where maximum shear strain in the interface shear bands is 1.48% and -2.82% in the near surface collapse region.

Figure 4-20 Lagrangian Strain (ε_{xy}), Neutral to Active Position, Cycle 1, Test T3

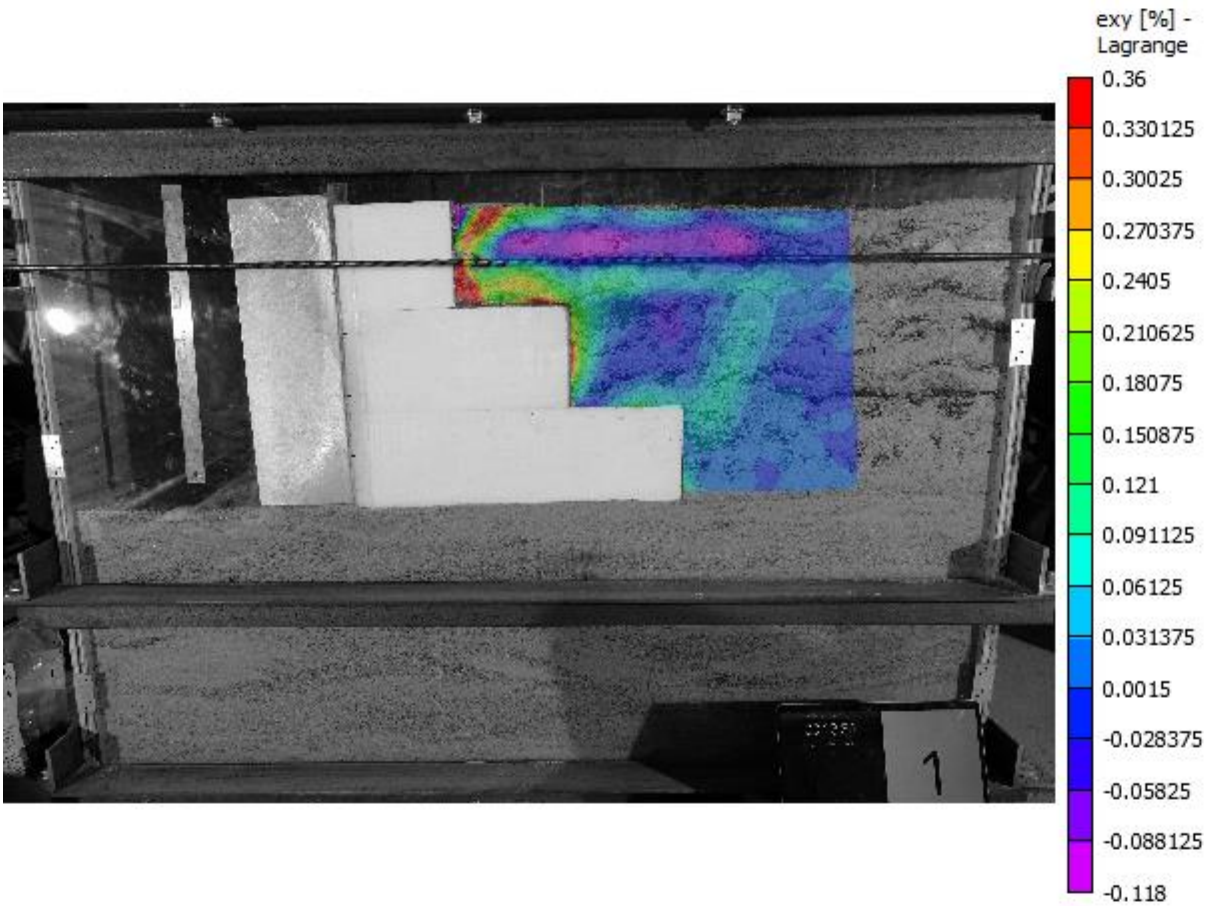

Figure 4-21 Lagrangian Strain (ε_{xy}), Neutral to Active Position, Cycle 5, Test T3

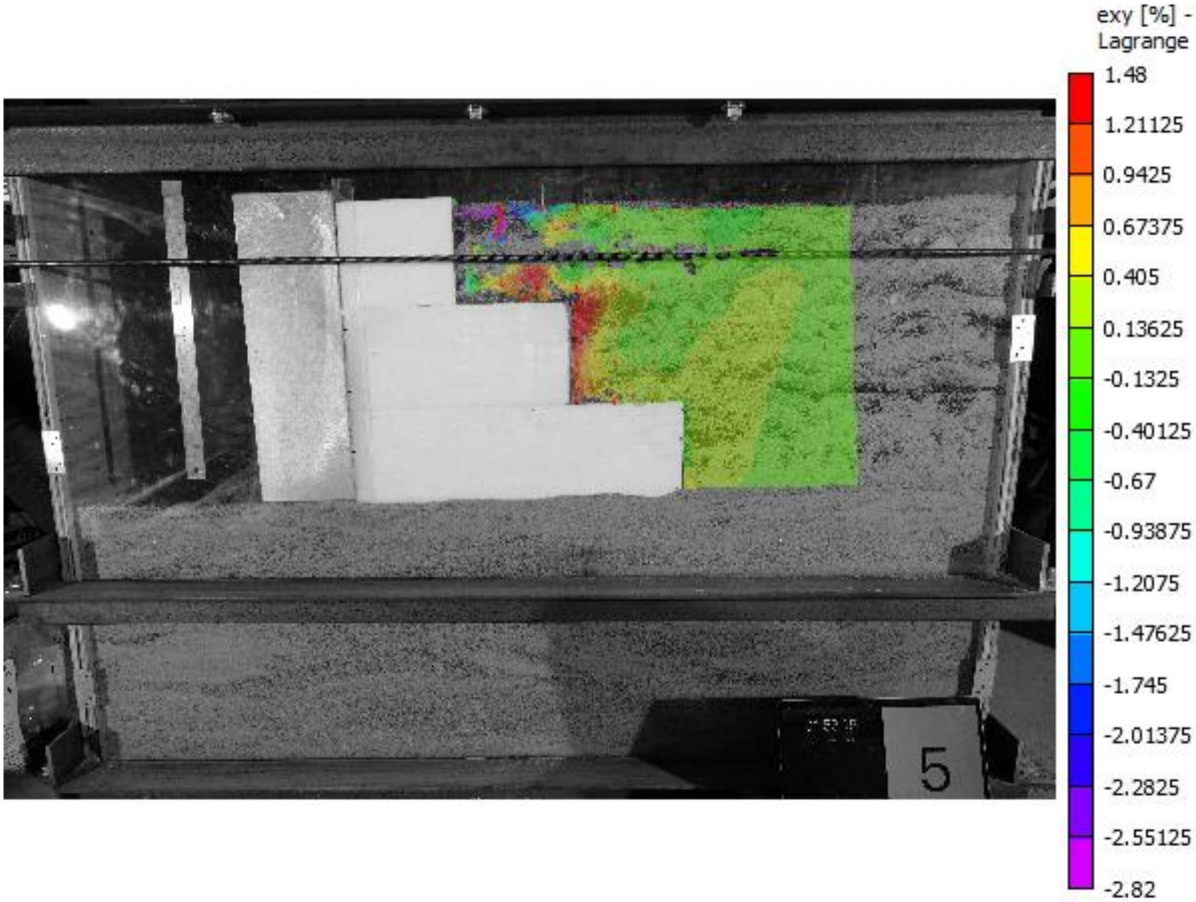

4.5 Test T4: Geotextile

In test T4, a geotextile reinforcement was placed behind the abutment. The spacing of geotextile sheets, lap lengths and other details are provided in Table 4-1.

Table 4.1 Geotextile Configuration, Test T4

	Vertical Spacing (cm)	Lap Length (cm)	Length (cm)	Note
First Four Layers	9.65	10.0	50.0	
Top Layer	9.65	40.0	50.0	- 10 cm of geotextile rests at the top the top of the backfill, followed by 10cm buried in the sand and inclined at approximately at 45° angle, followed by remaining 20 cm that is buried under 5 cm of sand

The maximum compressive force increased 6.72 kN in the 1st cycle to 7.63 kN in the 91st cycle, as shown in Figure 4-22. The captured vs intended displacement history is shown in Figure 4-23.

Figure 4-22 Horizontal Force vs Horizontal Displacement, Test T4

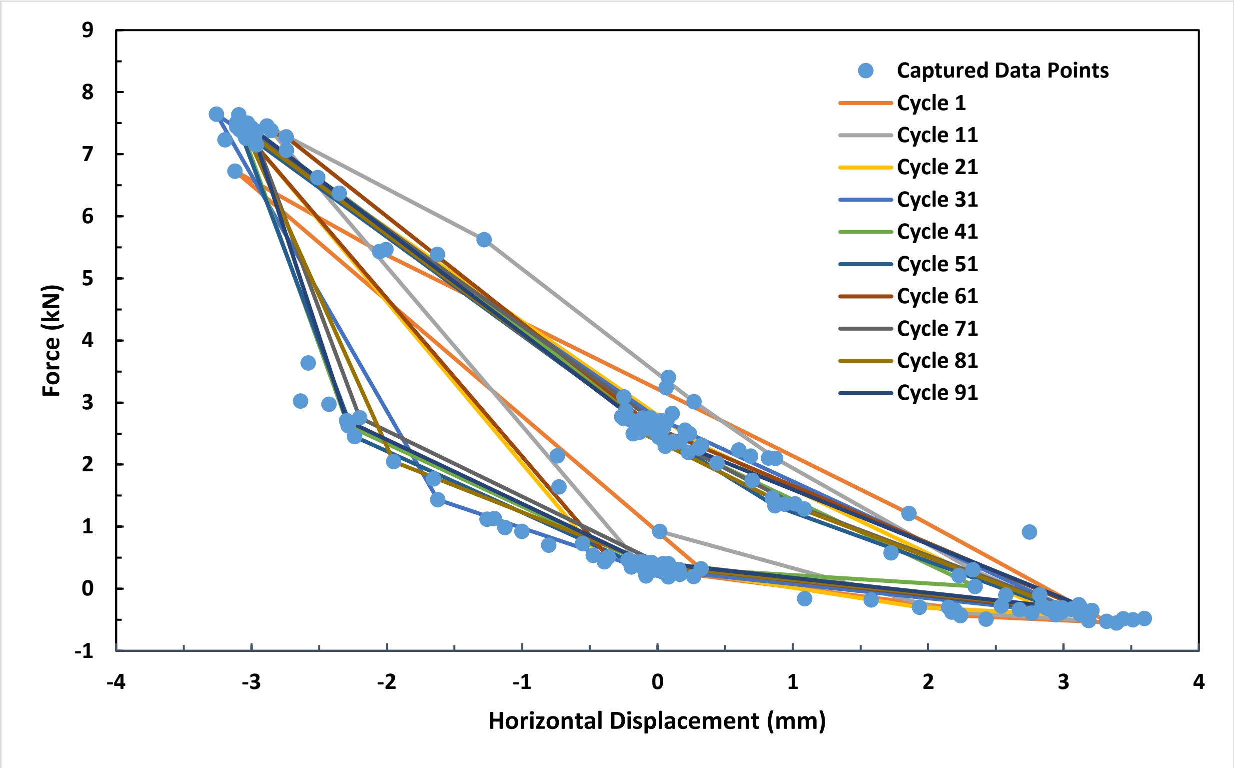

Figure 4-23 Intended Displacement History vs. Captured Data, Test T4

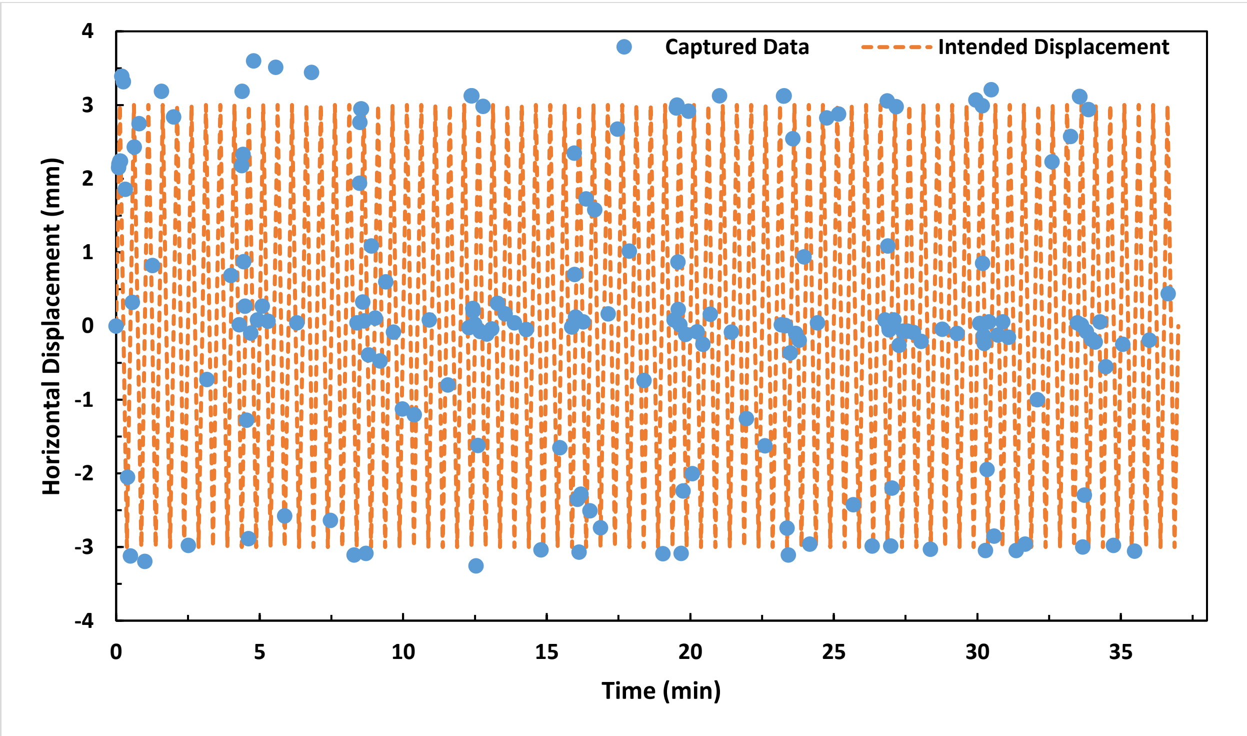

Figure 4-24 shows test T4 configuration including five geotextile sheets forming five reinforced soil layers, prior to the beginning of the test. Figure 4-25 below illustrates the position of the backfill at the end of the 100th cycle. The corresponding amount of the settlement at the interface of reinforced soil and abutment was 75.07 mm as shown in Figure 4-26. Additionally, settlement rate decreased with increasing number of cycles and it reaches significantly smaller rate around the 55th cycle.

Figure 4-24 Configuration Prior to the Beginning of Experiment, Test T4

Figure 4-25 Configuration at the End of Experiment, Test T4

Figure 4-26 Cycle Number vs. Settlement, Test T4

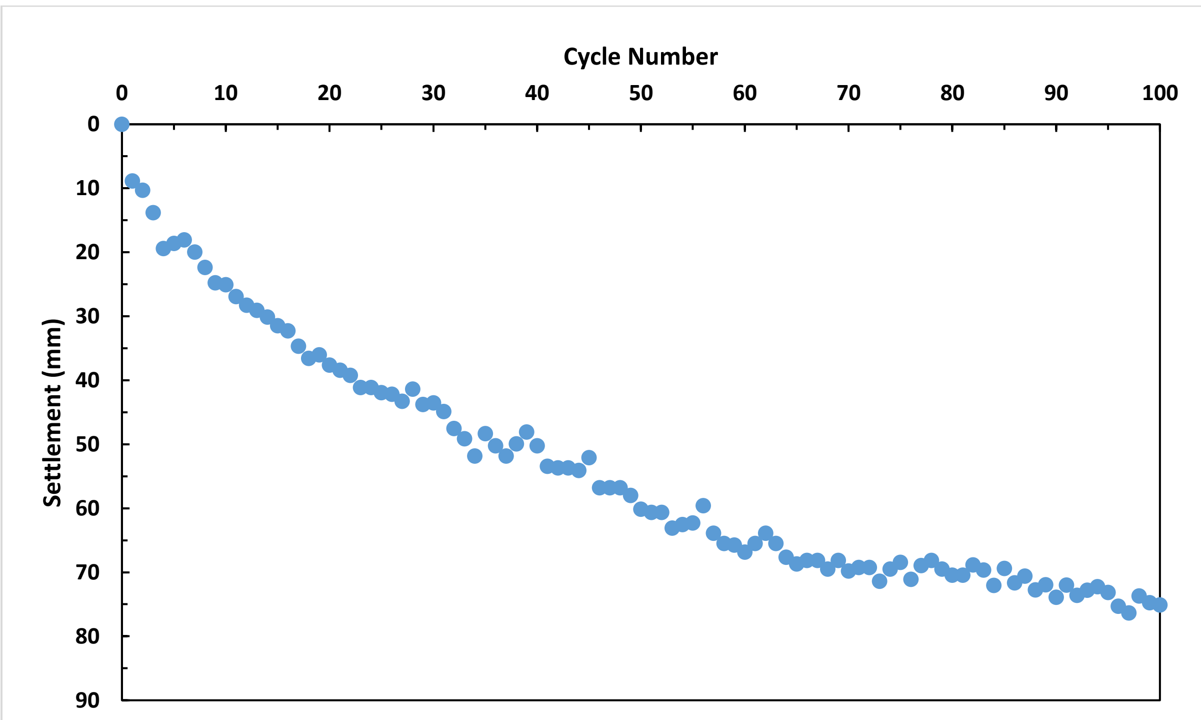

Figure 4-27 depicts the computed Lagrangian shear strain at the beginning of the 1st cycle. Although no shear band associated with active failure is present, there is a zone of large shear strain with maximum value of 2.96% develops at the interface with the abutment. Additionally, the zone of gradually increasing shear strain develops within the steep wedge next to the abutment. At the beginning of the 5th loading cycle seen in Figure 4-28 a region of localized strain next to the abutment remains with the maximum shear strain of 5.5%, and it is accompanied with large shear strain of -5.25% that is observed in the region of near surface collapse occurring inside the top geotextile layer. No shear band indicating active failure is identified.

Figure 4-27 Lagrangian Strain (ε_{xy}), Neutral to Active Position, Cycle 1, Test T4

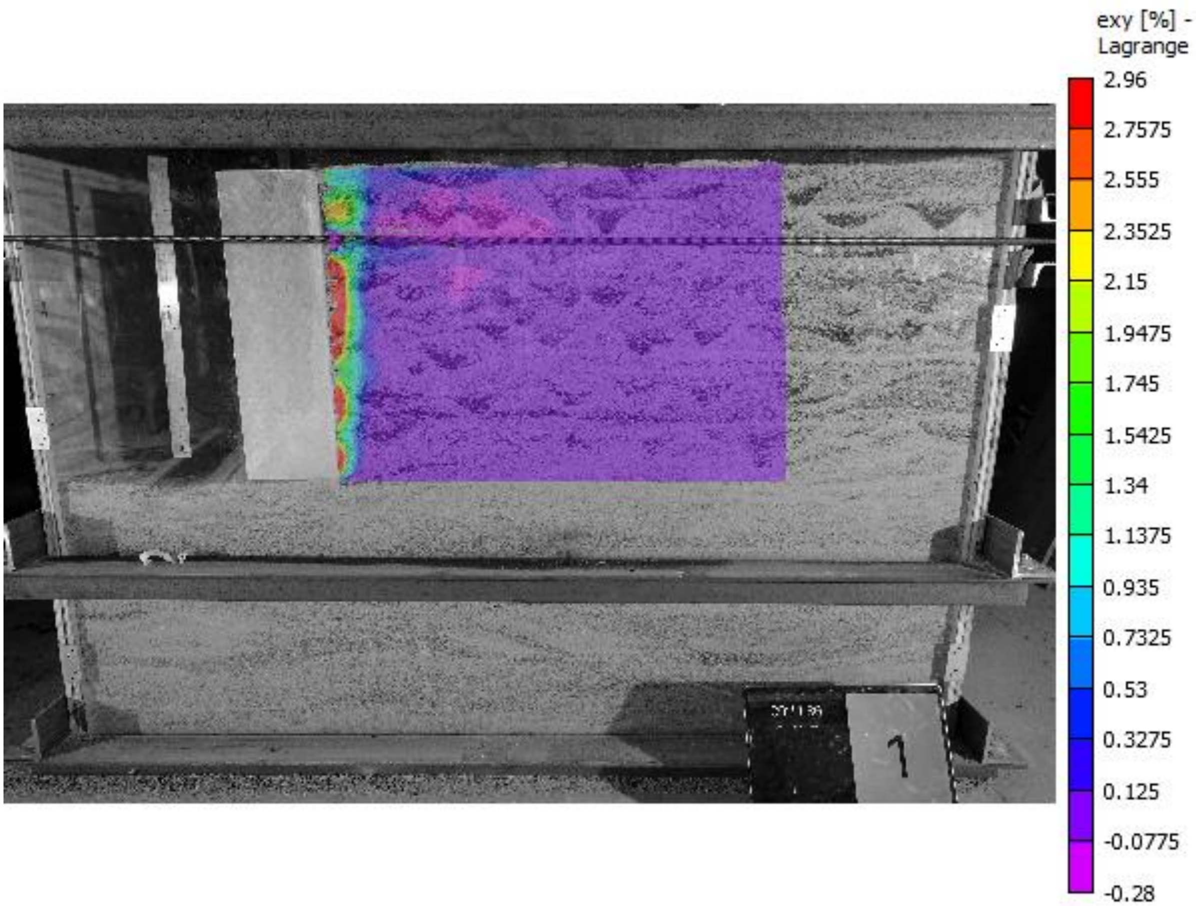

Figure 4-28 Lagrangian Strain (ε_{xy}), Neutral to Active Position, Cycle 5, Test T4

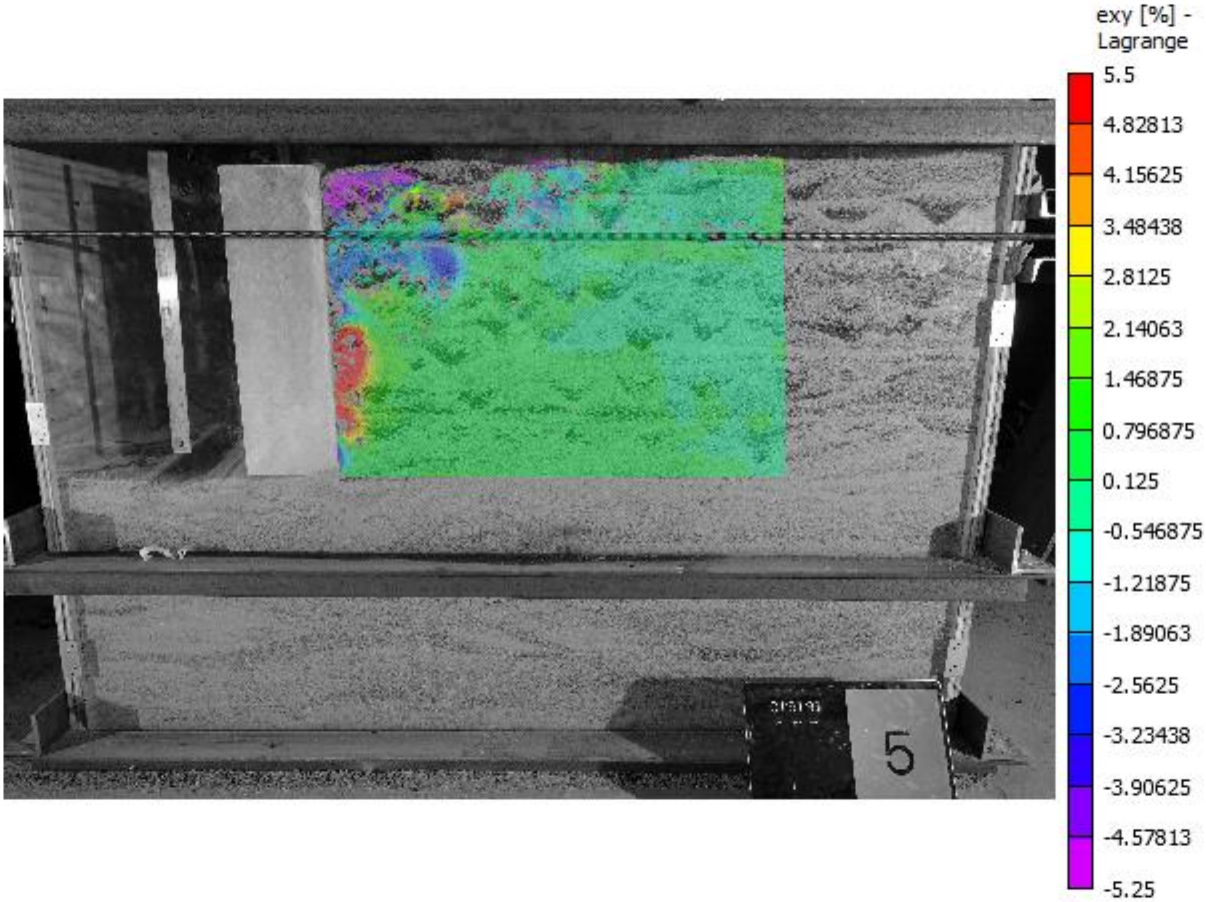

4.6 Test T5: Geogrid

Similarly, to placement of geotextile in test T4, geogrid reinforced backfill forms five soil layers. Further details including dimensions of geogrid are provided in Table 4.2.

Table 4.2 Geogrid Configuration, Test T5

	Vertical Spacing (cm)	Lap Length (cm)	Length (cm)	Note
First Four Layers	9.65	10.0	50.0	- A 30 cm piece of geotextile is wrapped around the facing geogrid next to the abutment.
Top Layer	9.65	40.0	50.0	- A 40 cm of geotextile is wrapped around the facing of the geogrid. - The geogrid rests at the top the top of the backfill, followed by 10cm buried in the sand and inclined at approximately at 45° angle, followed by remaining 20 cm that is buried under 5cm of sand.

As shown in Figure 4-29, the measured horizontal force increased from 6.34 kN in the 1st cycle to 7.81 kN in the 91st cycle. Intended vs measured displacement history is depicted in Figure 4-30.

Figure 4-29 Horizontal Force vs. Horizontal Displacement, Test T5

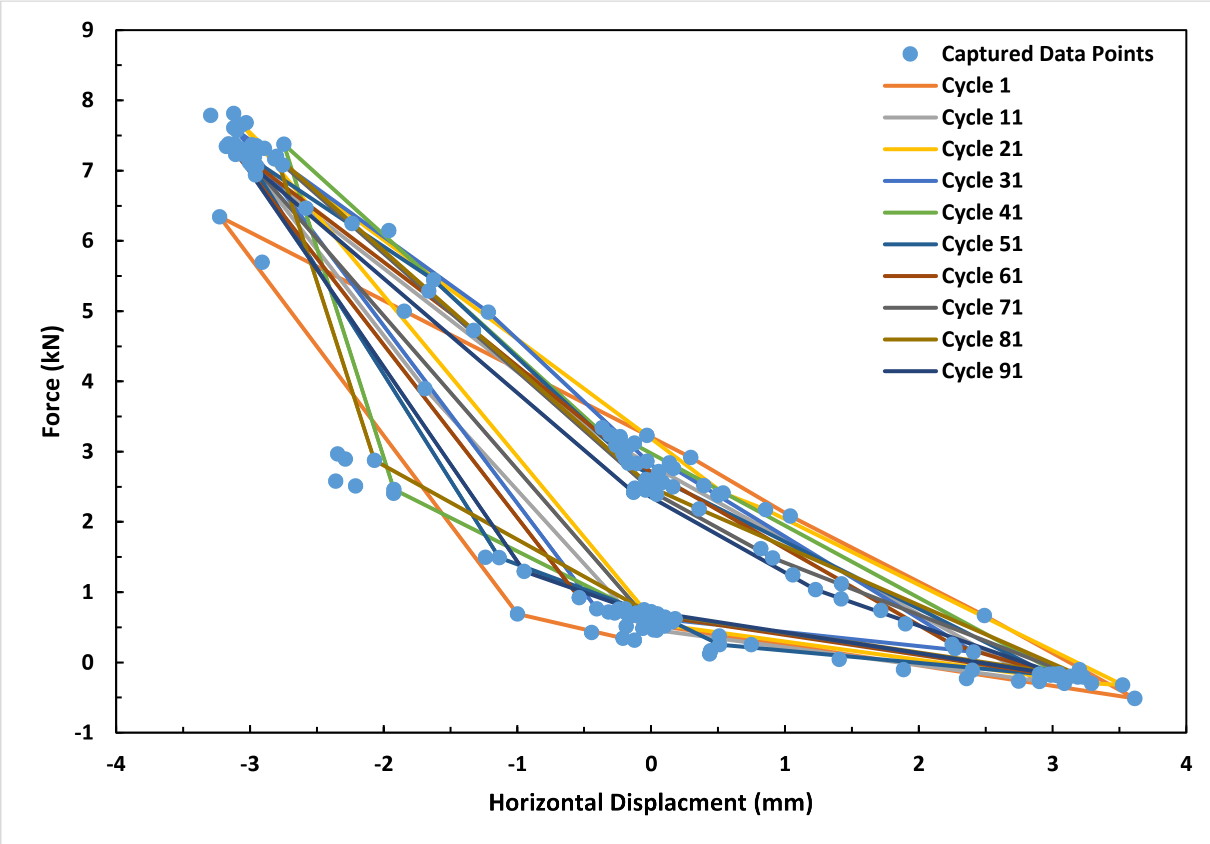

Figure 4-30 Intended Displacement History vs. Captured Data, Test T5

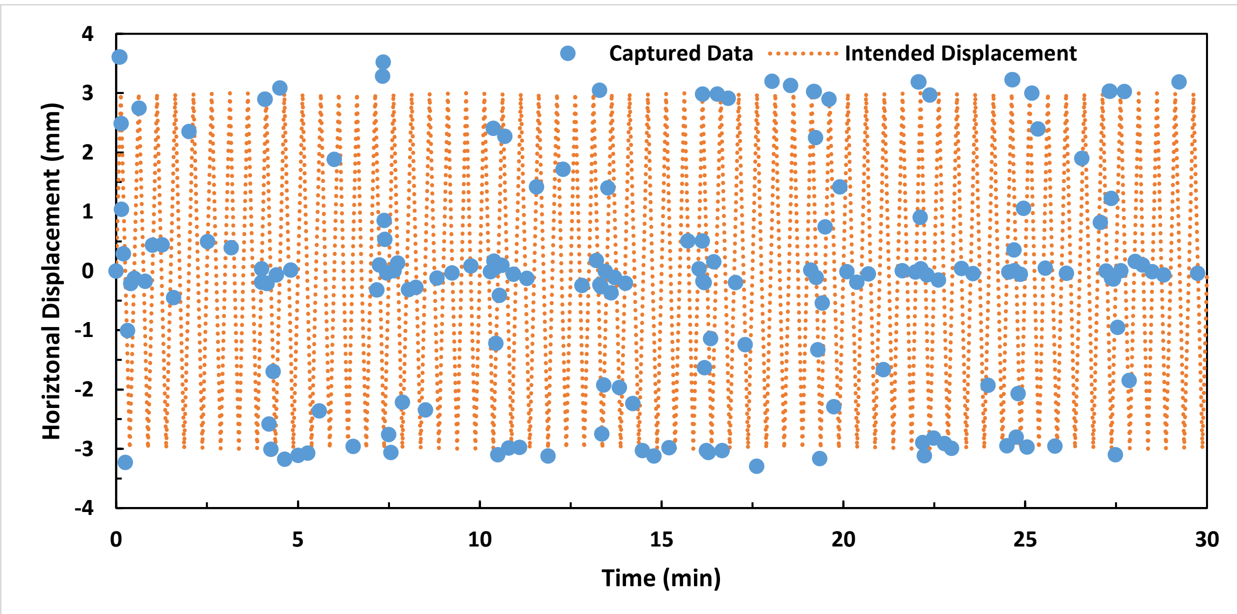

Figure 4-31 shows the backfill configuration with geogrid reinforced soil layers prior to the beginning of the test while Figure 4-32 shows the state at the end of the 100th cycle that resulted in the total settlement of 75.86 mm, as shown in Figure 4-33. The settlement rate decreases with increasing number of cycles and it becomes significantly smaller around the 50th cycle.

Figure 4-31 Configuration Prior to Beginning of Experiment, Test T5

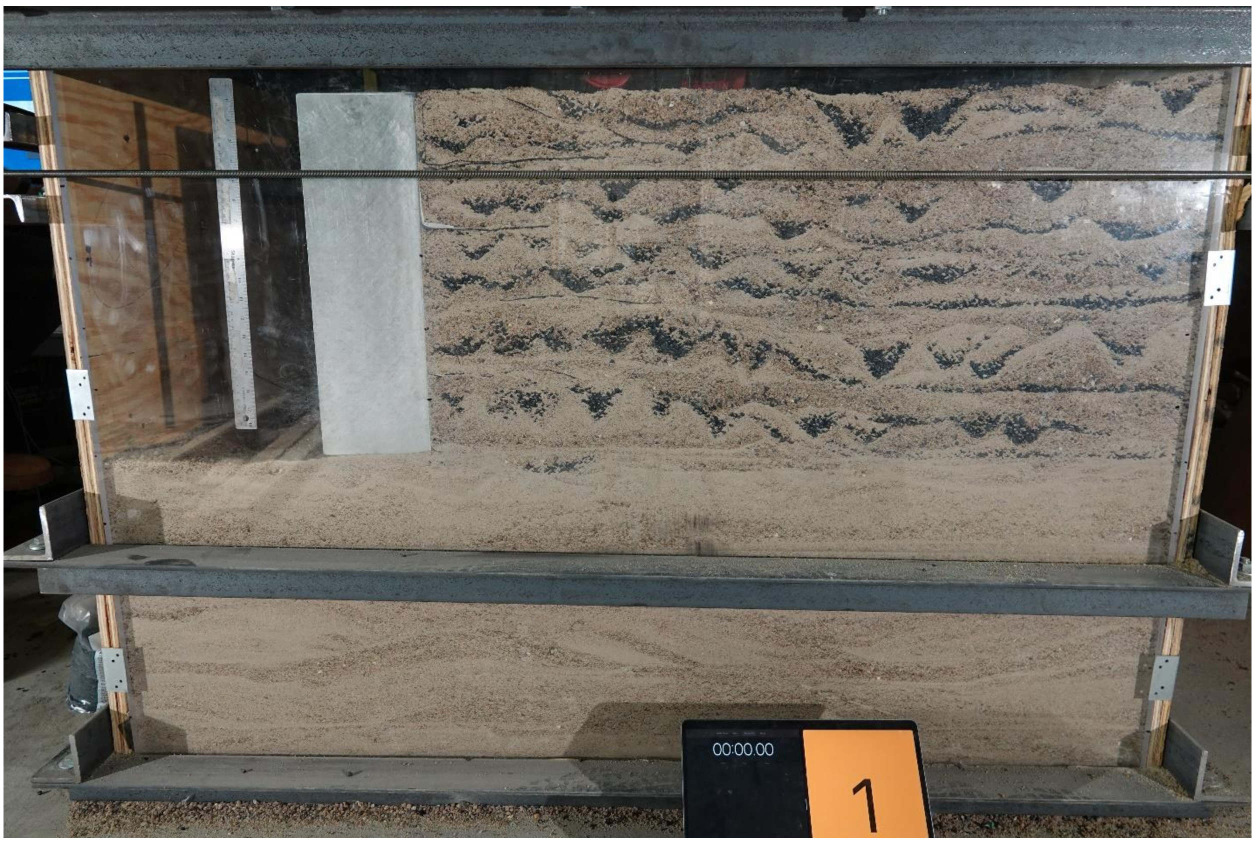

Figure 4-32 Configuration at End of Experiment, Test T5

Figure 4-33 Cycle Number vs. Settlement, Test T5

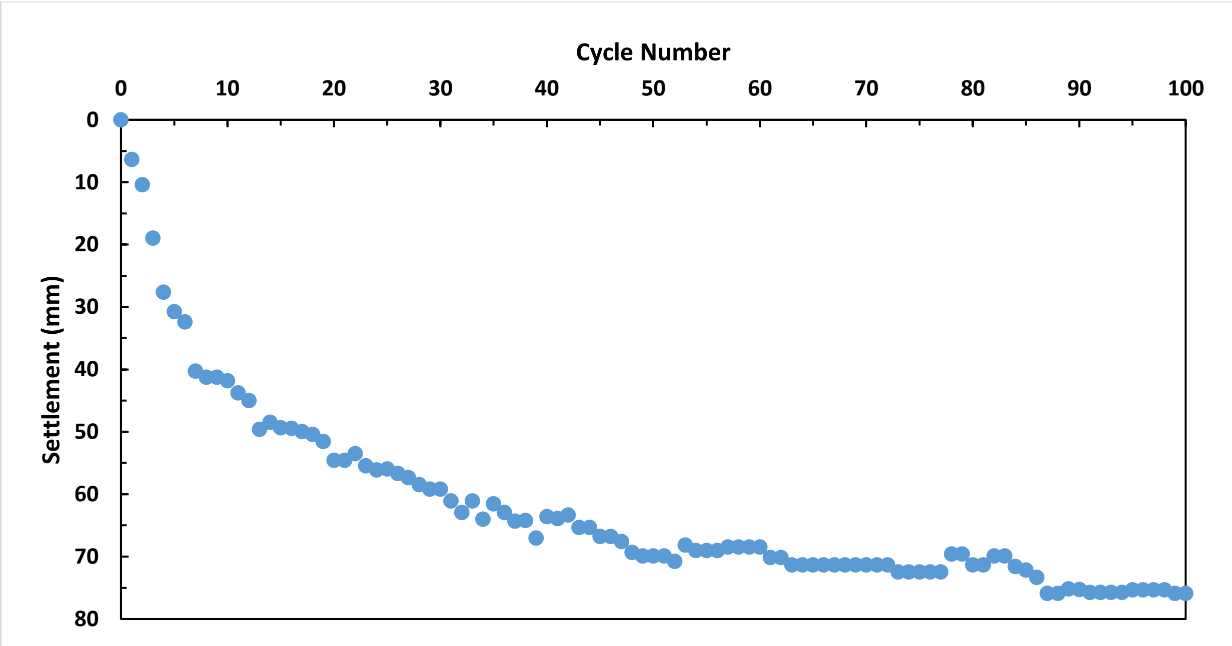

VIC-2D computed Lagrangian shear strain at the very beginning of test T5 and the corresponding heat map is shown in Figure 4-34. Similarly, to test T4, the largest shear strain in the amount of 4.3% develops at the soil-abutment interface, and wedge-shaped steep zone of gradually increasing shear strain forms behind the abutment. No shear bands associated with active failure are identified. The heat map of Lagrangian shear strain that develops between the undeformed configuration and the beginning of cycle 5, Figure 4-35, indicates some remnants of the interface shear band are present and accompanied with diffuse region of large shear strain indicating near surface collapse. The maximum shear strain within the interface shear band is 8.75% while the minimum shear strain within the region of near surface collapse is -1.95%.

Figure 4-34 Lagrangian Strain (ε_{xy}), Neutral to Active Position, Cycle 1, Test T5

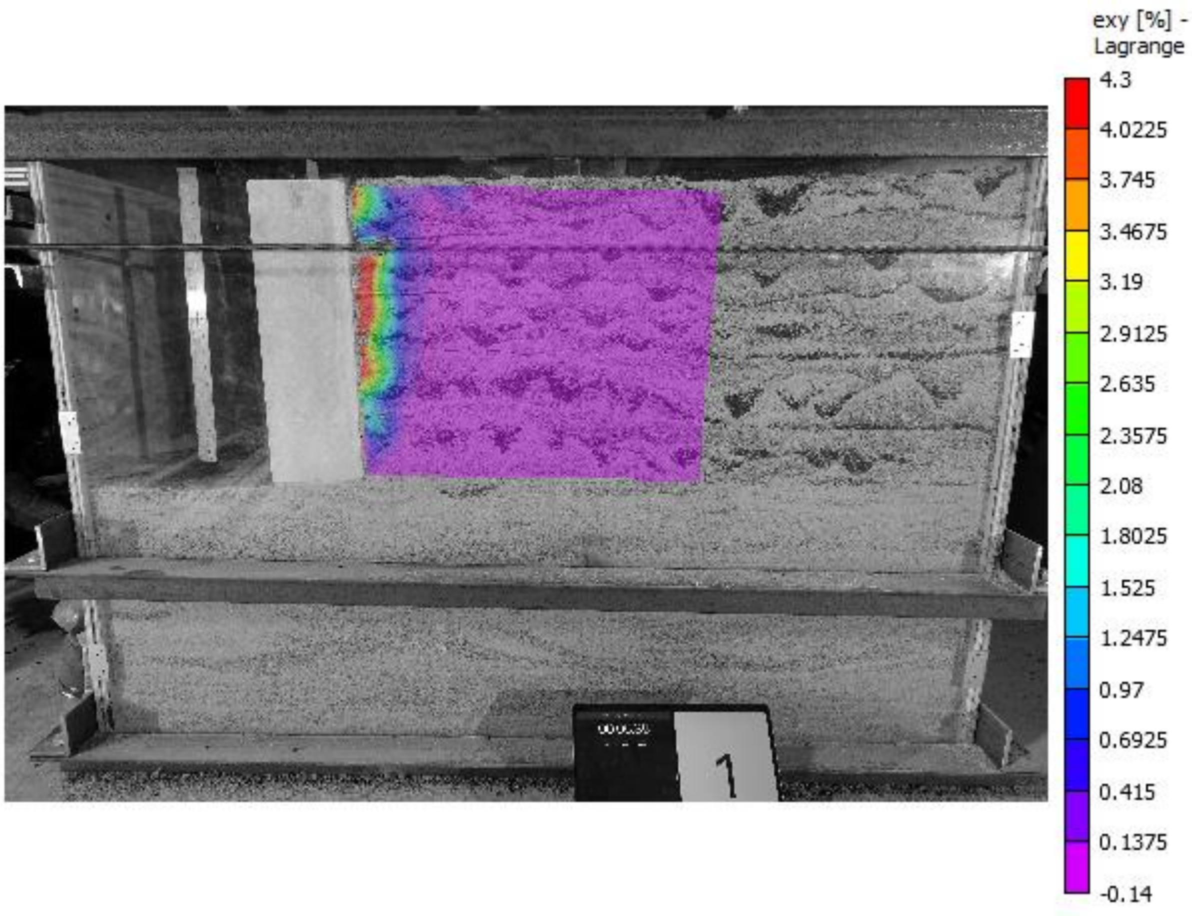

Figure 4-35 Lagrangian Strain (ε_{xy}), Neutral to Active Position, Cycle 5, Test T5

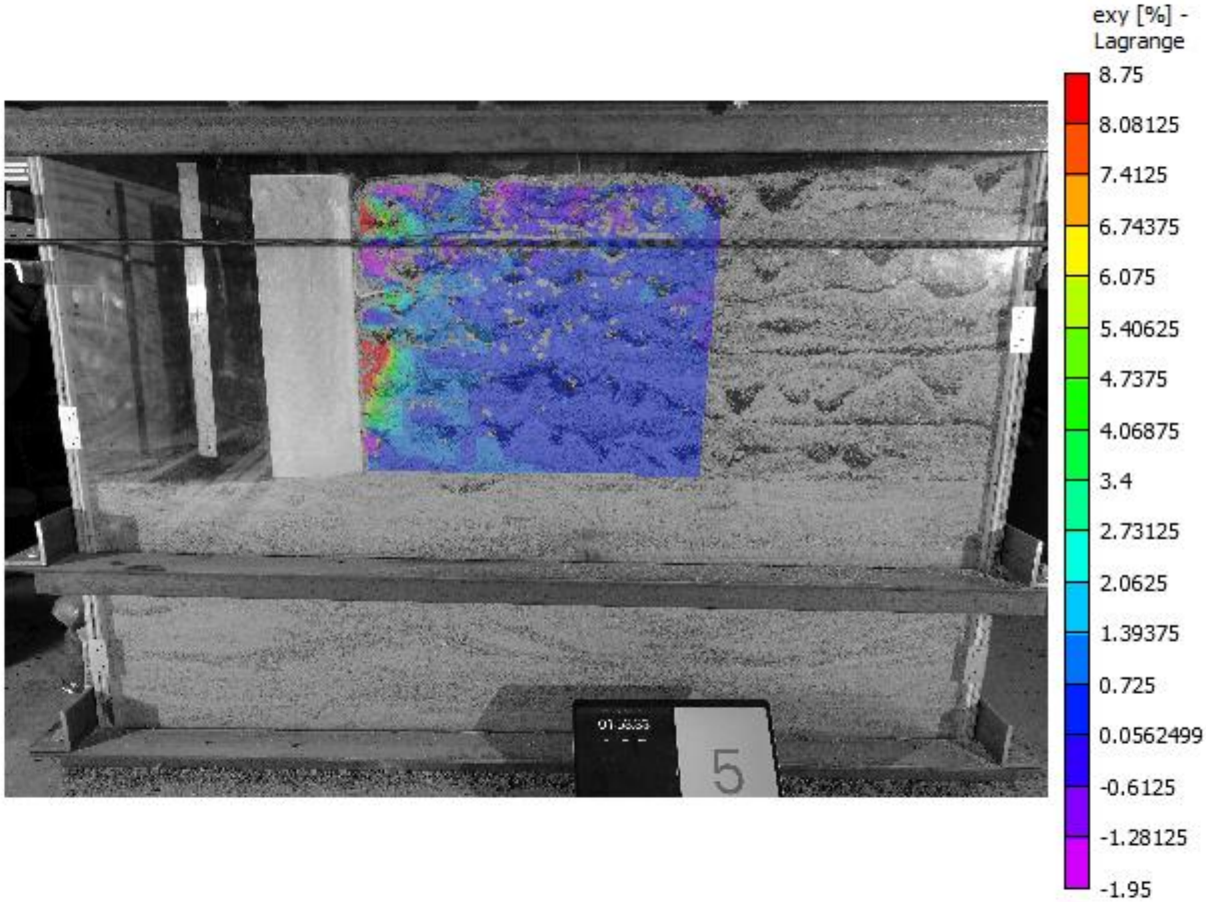

4.7 Test T6: Soft Density EPS 10.16 cm Foam Sheet

In test T6, a 10.16 cm thick soft EPS geofoam sheet was inserted behind the abutment and in front of the backfill. The maximum compressive force measured in cycle one was 6.3 kN and it increased to 9.36 kN at the end of 91st cycle, as shown in Figure 4-36. The intended vs captured displacement history is depicted in Figure 4-37.

.

Figure 4-36 Horizontal Force vs. Horizontal Displacement, Test T6

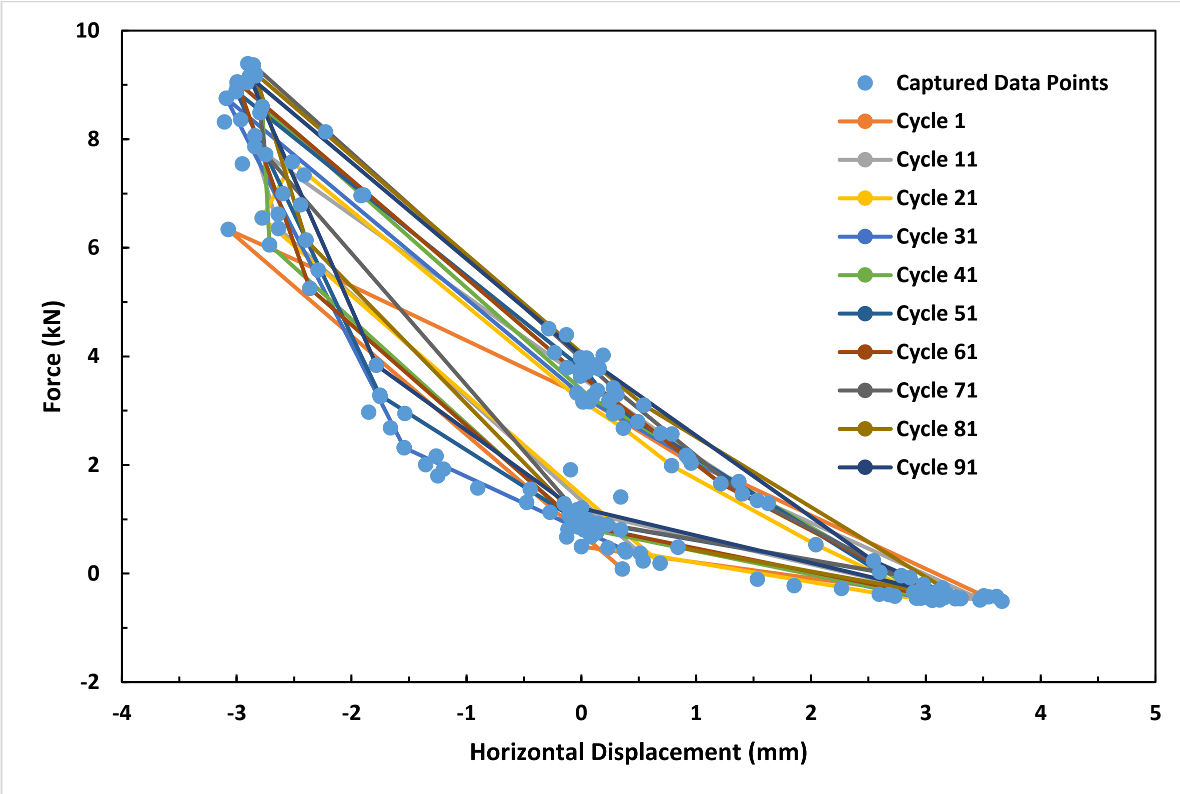

Figure 4-37 Intended Displacement History vs. Captured Data, Test T6

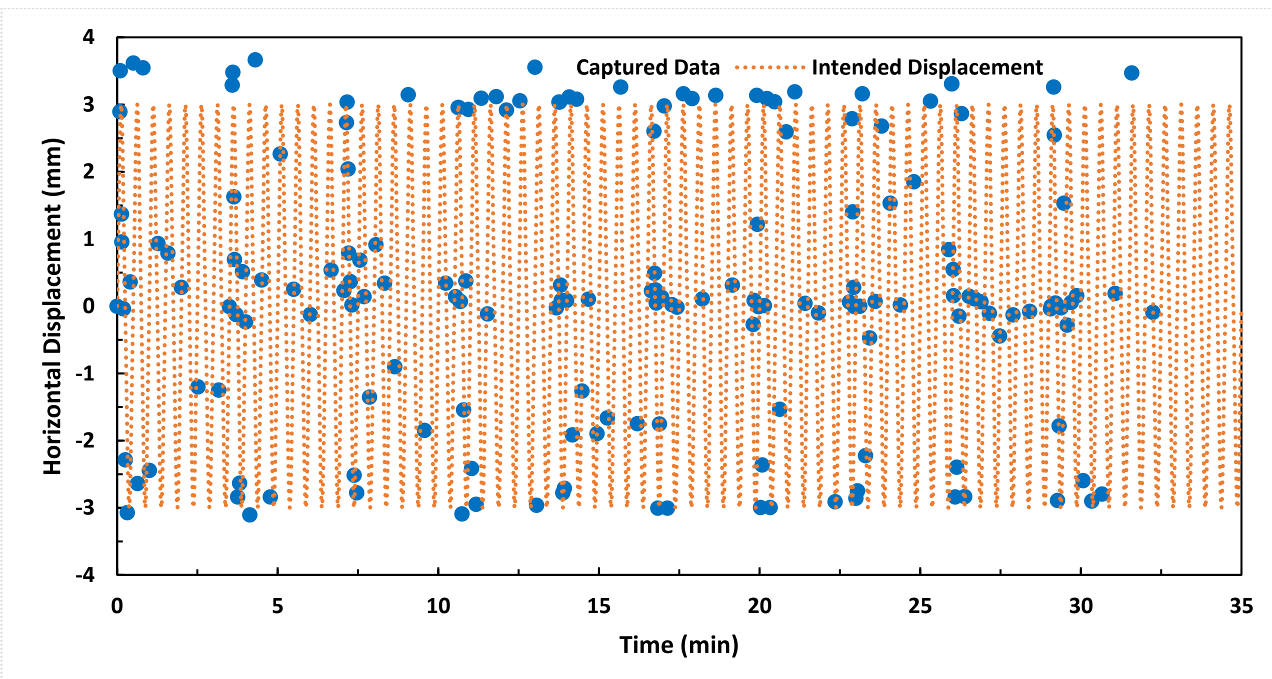

Figure 4-38 depicts the arrangement of the backfill along with in EPS geofoam inclusion prior to the beginning of the test while Figure 4-39 shows the state at the end of 100th cycles resulting in a total settlement of 65.73 mm, which is shown in Figure 4-40. The settlement rate first decreases, then increases again, and finally decreases.

Figure 4-38 Configuration Prior to the Beginning of Experiment, Test T6

Figure 4-39 Configuration at the End of Experiment, Test T6

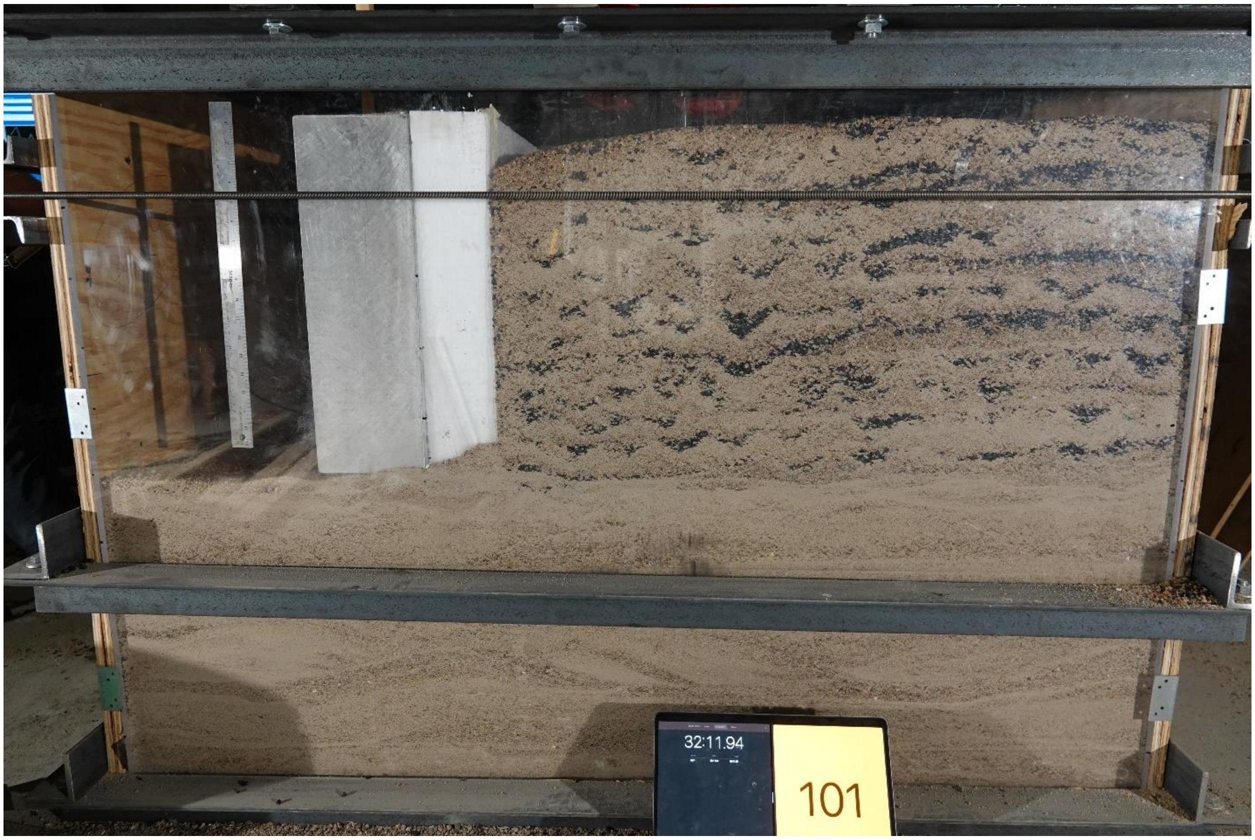

Figure 4-40 Cycle Number vs. Settlement. Test T6

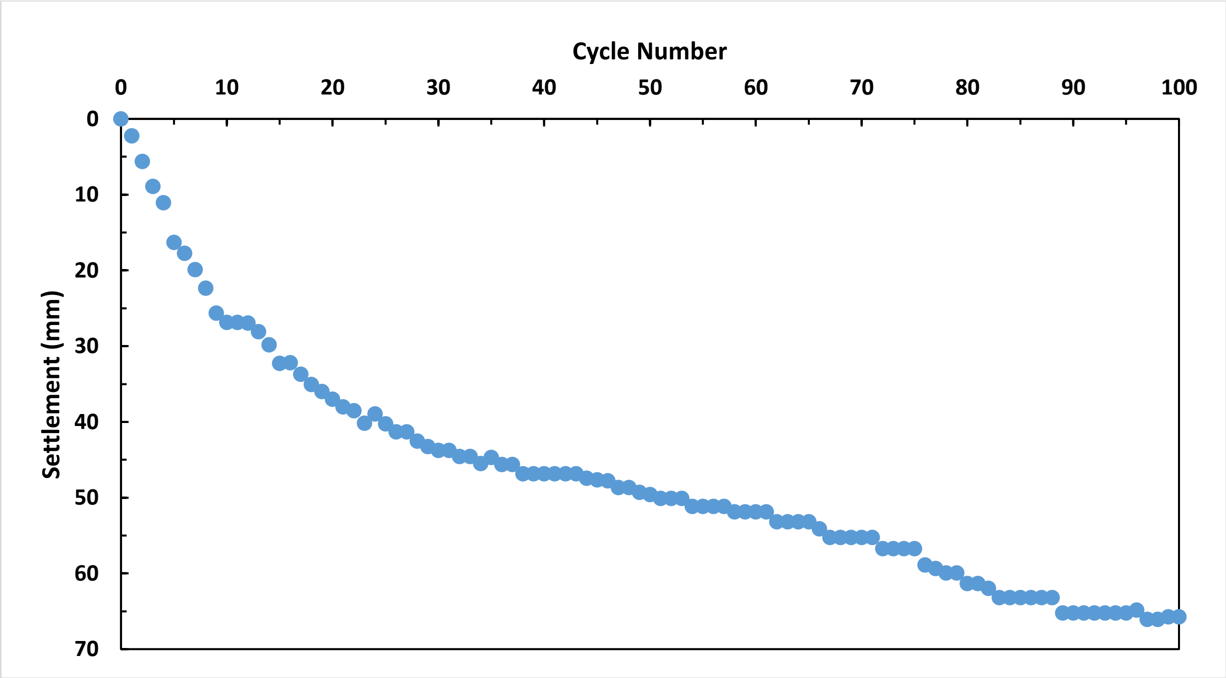

Figure 4-41 below depicts the Lagrangian shear strain at the very beginning of the test, calculated by VIC-2D indicating that the interface shear band developed at the contact of the EPS geofoam and the backfill, within which the maximum shear strain was 2.42%. In addition, the wedge zone featuring gradually increasing shear strain formed in the backfill next to the EPS geofoam inclusion, but it is not bounded by active shear band at the right side, indicating the absence of active failure. Lagrangian shear strain at the beginning of the 5th cycle is shown in Figure 4-42 indicating that at this stage a more diffuse interface shear band is still present with maximum shear strain of 5%. Additional region of high shear strain develops in the area of near surface soil collapse with minimum shear strain of -6.95%. No shear band associated with active failure is present at this stage.

Figure 4-41 Lagrangian Strain (ε_{xy}), Neutral to Active Position, Cycle 1, Test T6

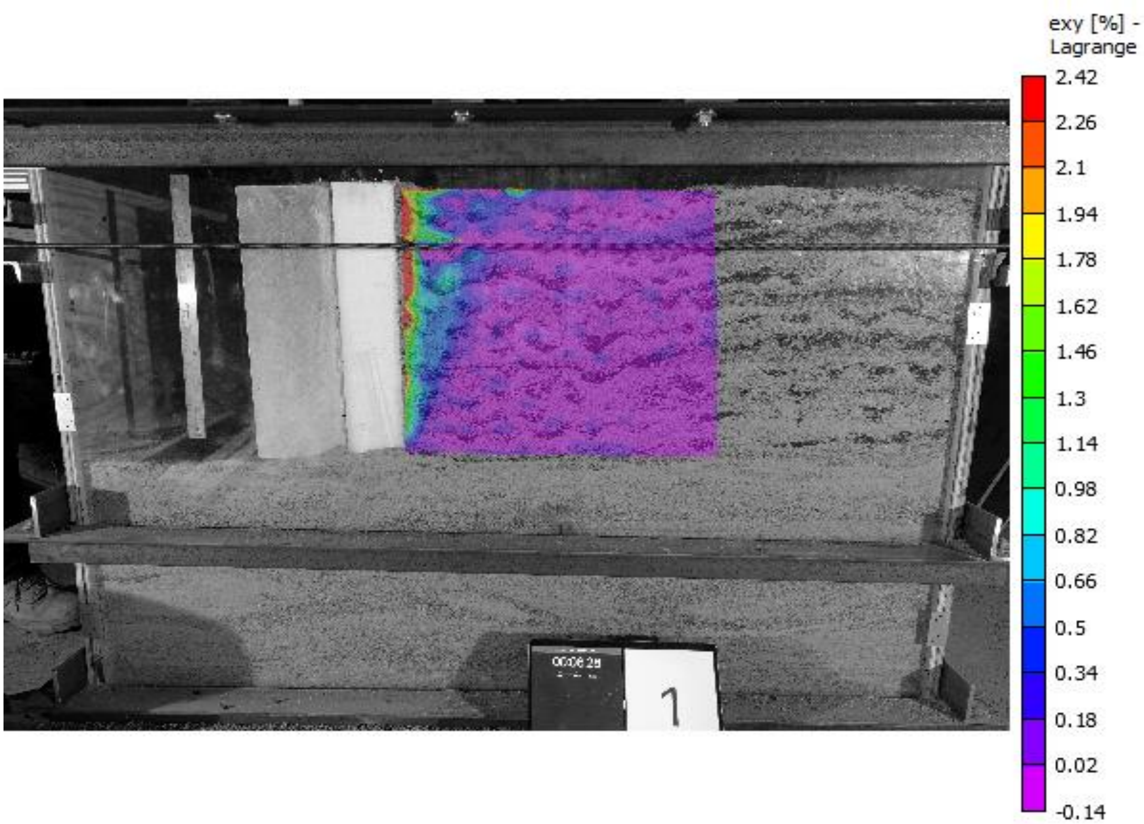

Figure 4-42 Lagrangian Strain (εxy), Neutral to Active Position, Cycle 5, Test T6

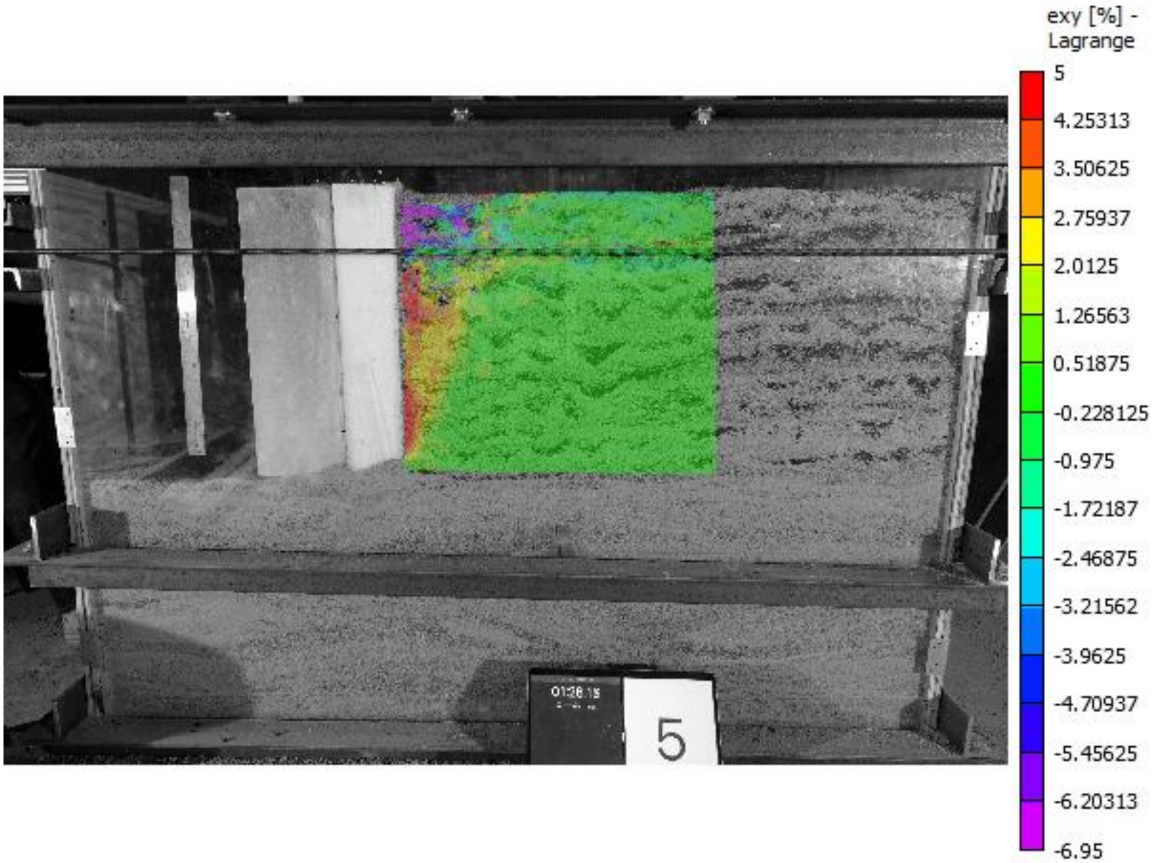

4.8 Test T7: Stiff Density EPS 10.16 cm Geofoam Sheet

For test T7 a 10.16 cm thick EPS geofoam sheet was inserted behind the abutment. The maximum compressive measured force during the 1st cycle was 6.10 kN and it increased to 9.29 kN by the 91st cycle, as shown in Figure 4-43. The intended and captured displacement history is shown in Figure 4-44.

Figure 4-43 Horizontal Force vs. Horizontal Displacement, Test T7

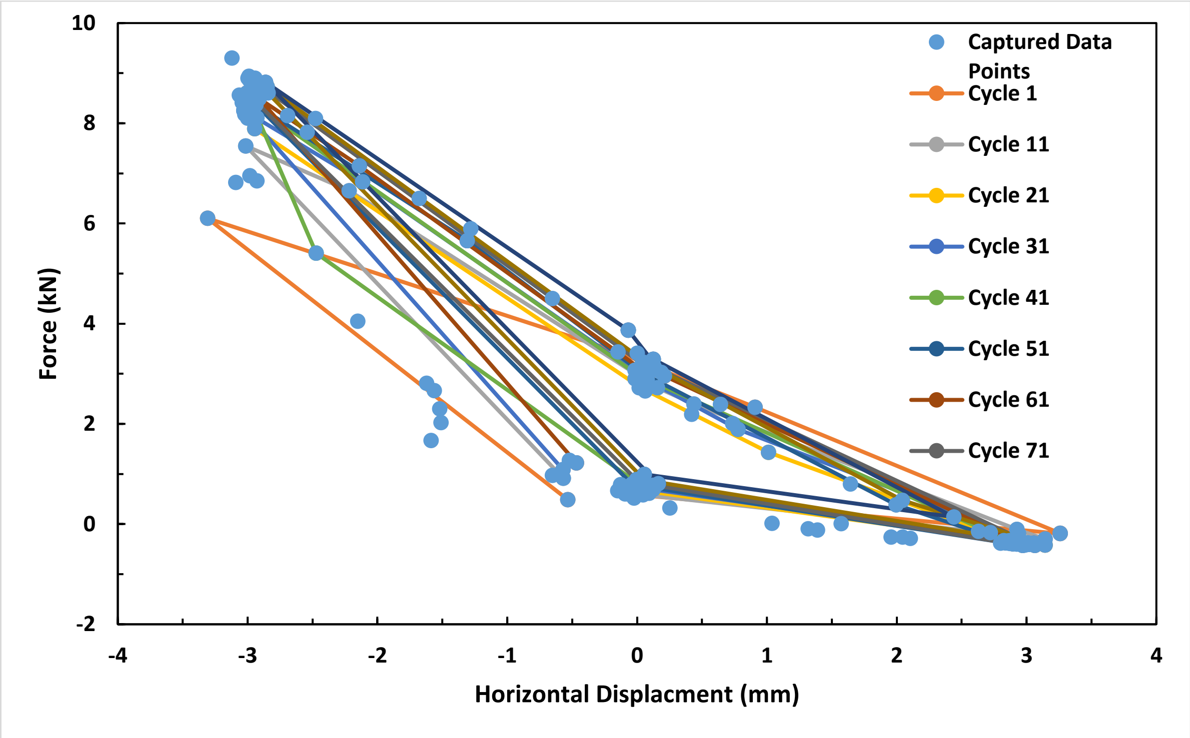

Figure 4-44 Intended Displacement History vs. Captured Data, Test T7

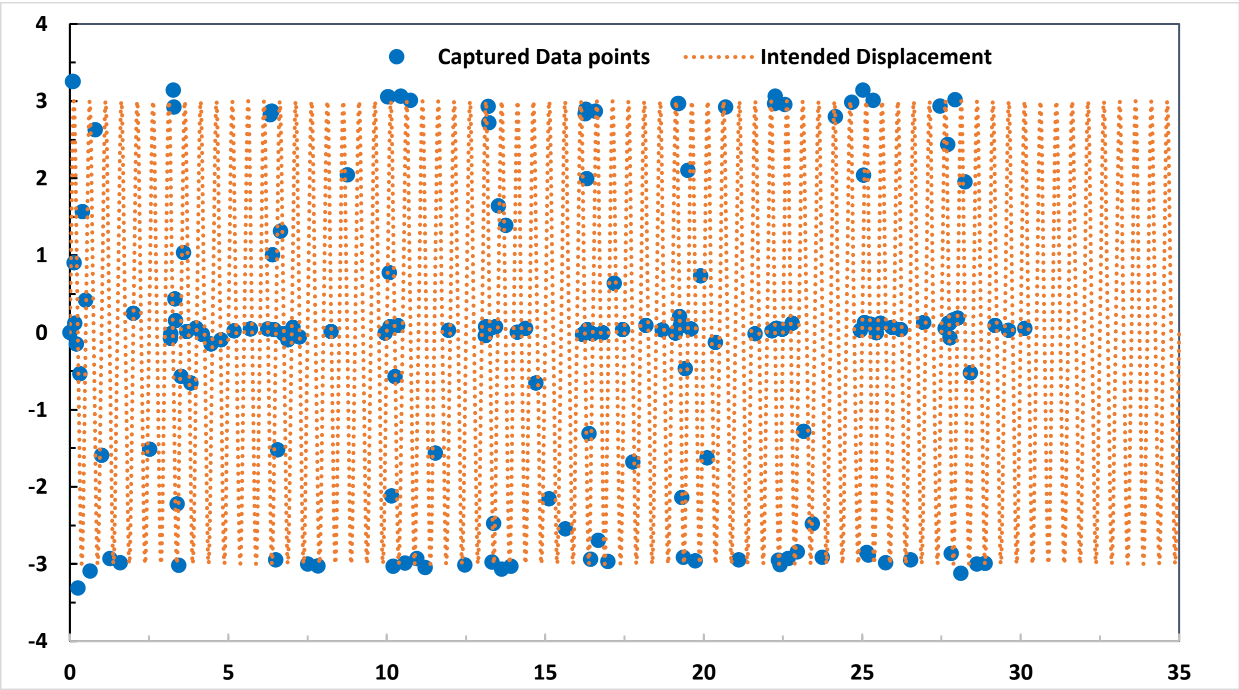

\

Figure 4-45 depicts the arrangement of the backfill along with the EPS geofoam inclusion before beginning of the test. Figure 4-46 captures that state at the end of the 100th cycle, resulting in the interface settlement of 70.54 mm, as shown in Figure 4-47. Although settlement rate decreases with increasing number of cycles, it reaches a constant value around the 30th cycle.

Figure 4-45 Configuration Prior to the Beginning of Experiment, Test T7

Figure 4-46 Configuration at the End of Experiment, Test T7

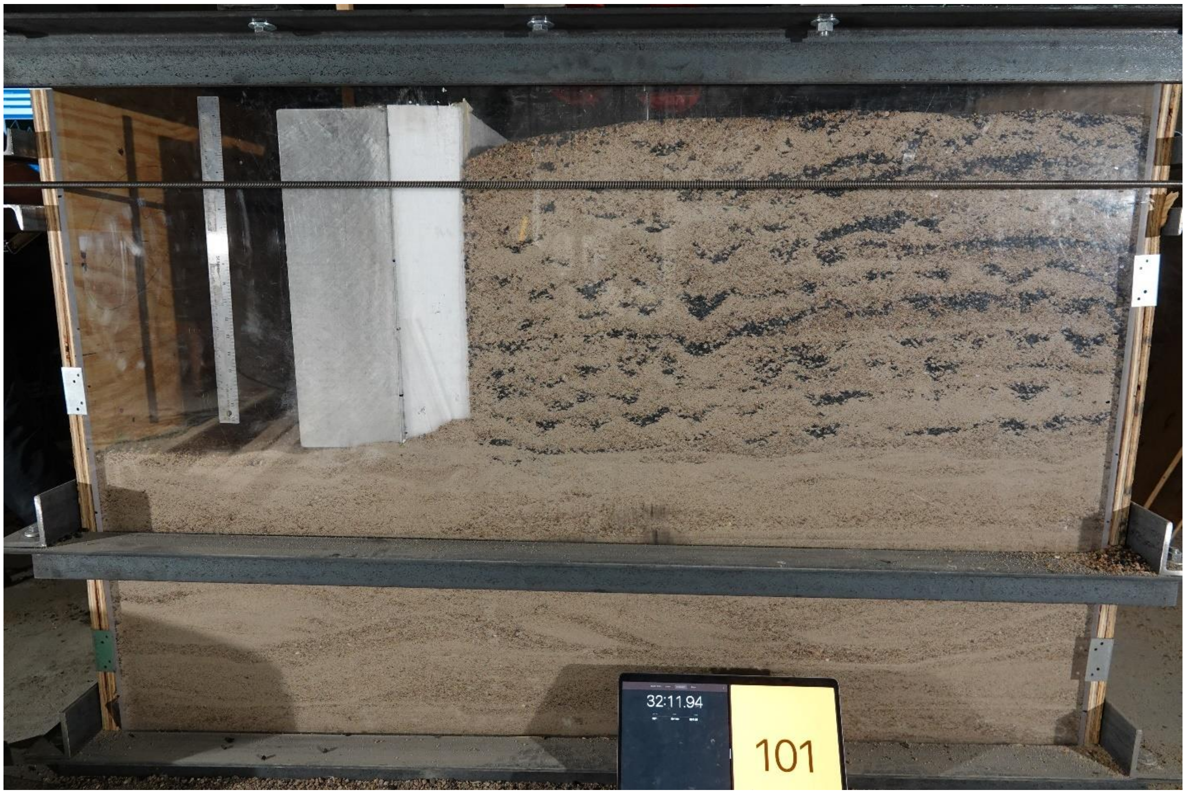

Figure 4-47 Cycle Number vs. Settlement. Test T7

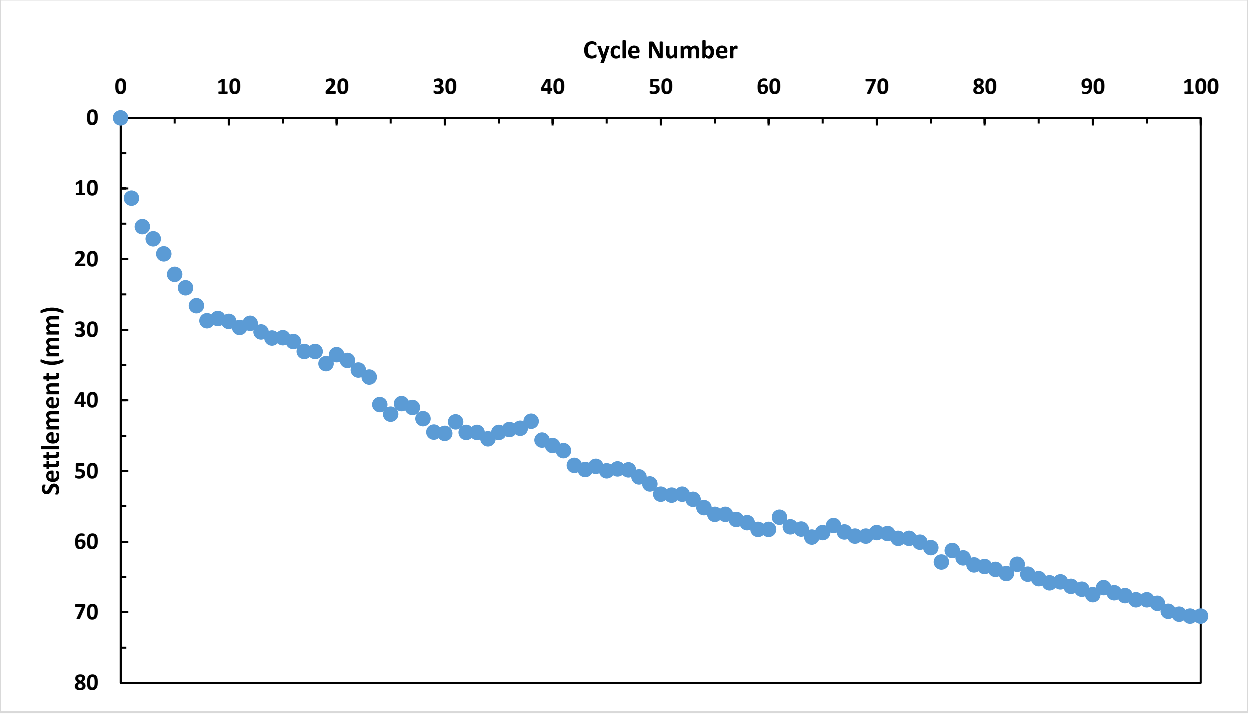

Figure 4-48 shows the heat map of Lagrangian shear strain, which was computed by VIC-2D at the beginning of the test. Vertical interface shear band that develops along the EPS geofoam-backfill contact features maximum shear strain of 1.7%. Although strain gradually increases within the wedge-shaped region behind the abutment no shear band indicating active failure is present. Figure 4-49 shows the heat map of Lagrangian shear strain that develops between the initial undeformed configuration and beginning of the 5th cycle. The observed strain pattern is similar to the one depicted in Figure 4-48. Besides the observed maximum shear strain within the interface shear band that has increased to 5.05% there is also a small near surface region exhibiting shear strain of 5.05%.

Figure 4-48 Lagrangian Strain (ε_{xy}), Neutral to Active Position, Cycle 1, Test T7

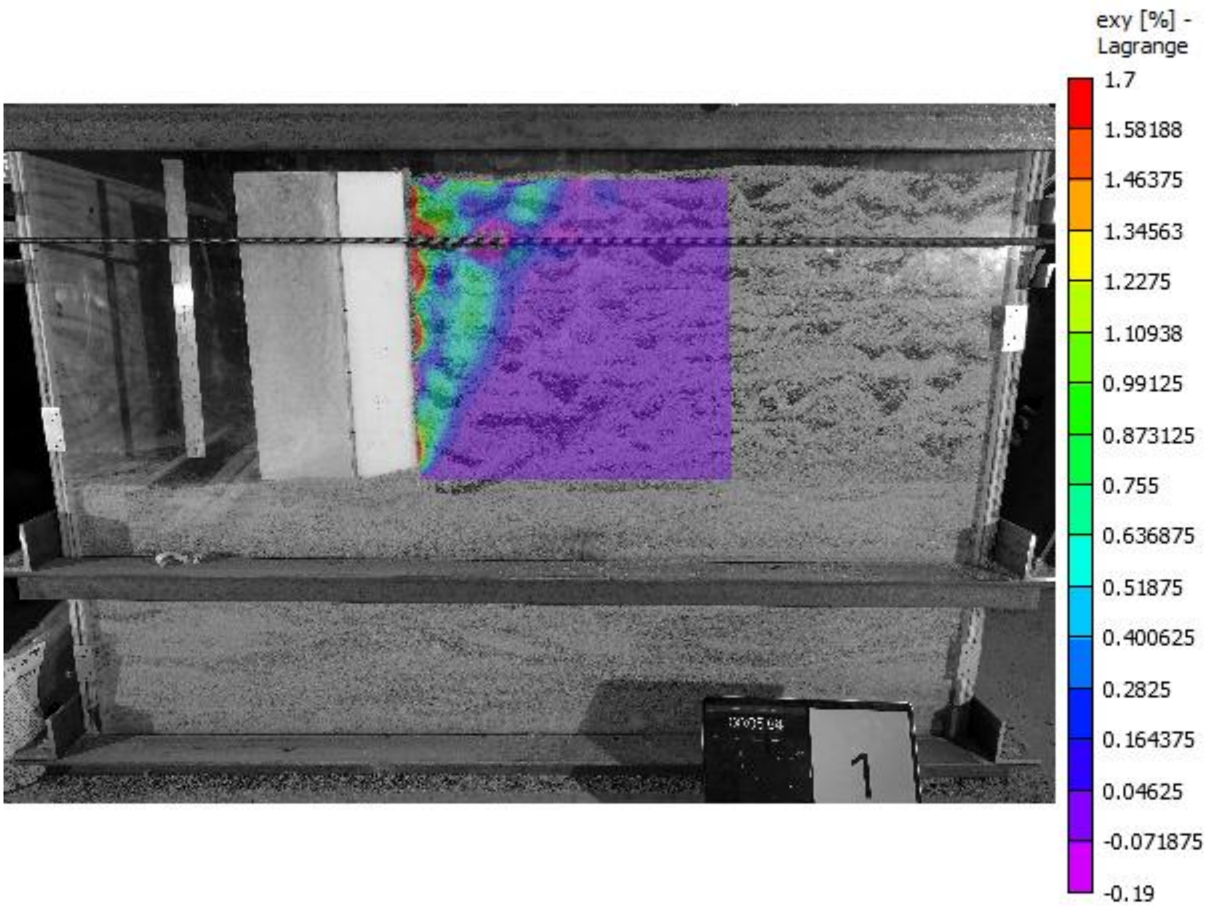

Figure 4-49 Lagrangian Strain (ε_{xy}), Neutral to Active Position, Cycle 5, Test T7

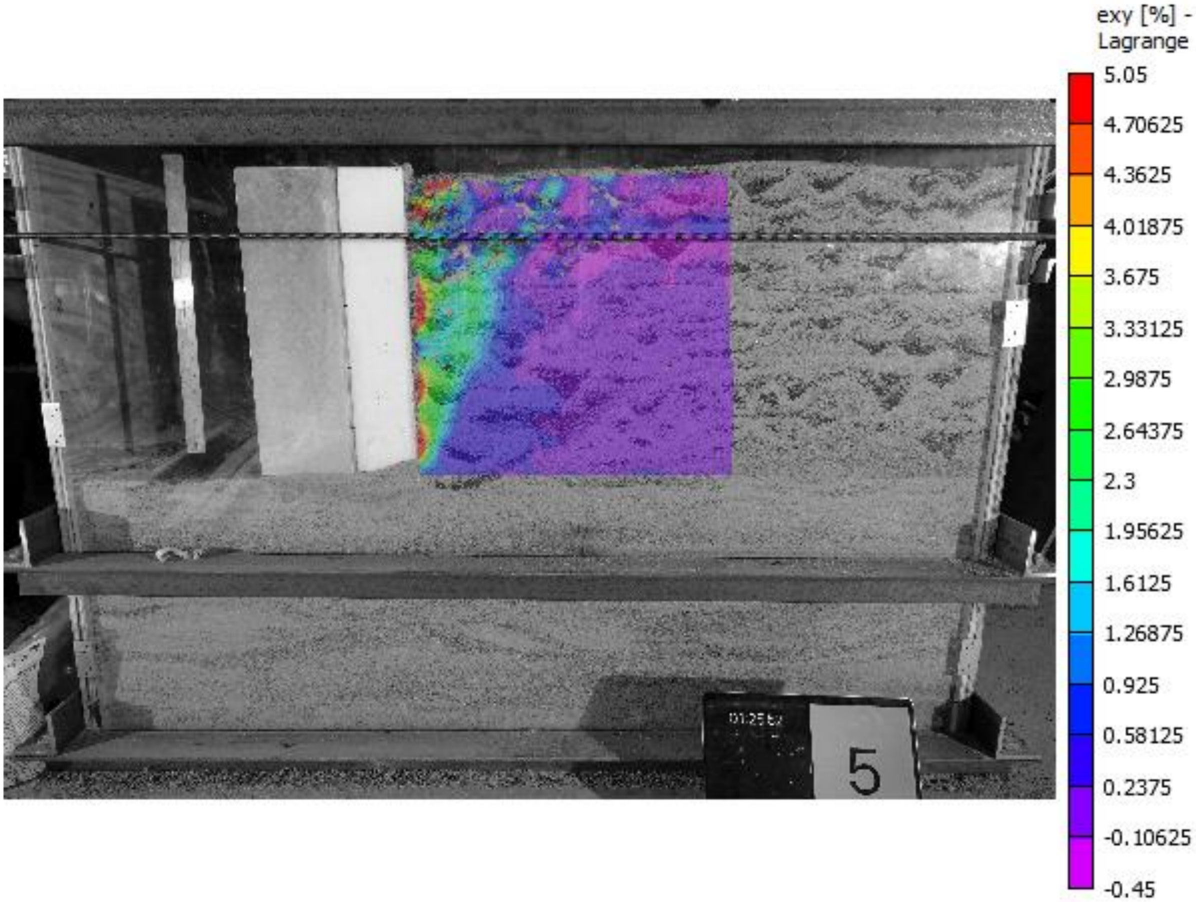

4.9 Test T8: Soft Density EPS 5.08 cm Sheet with Geogrid

In Test T8, a 5.08 cm a soft EPS geofoam sheet was placed behind the abutment and in front of the backfill. Five layers of soil were reinforced with a geogrid and facing as described previously in Table 4.2 in section 4.6. The maximum measured compressive force was 8.03 kN and it remained approximately constant throughout 100 loading cycles. Figure 4-50 shows intended versus captured displacement history.

Figure 4-50 Horizontal Force vs. Horizontal Displacement, Test T8

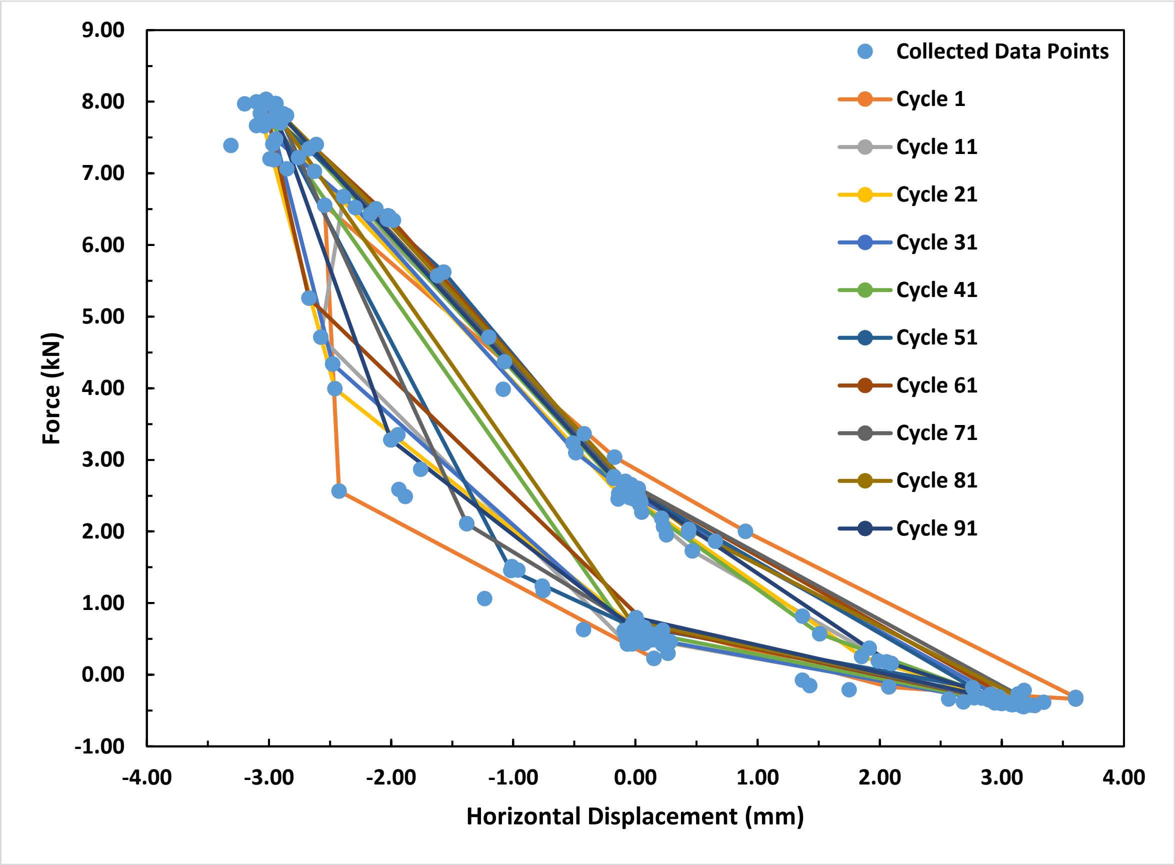

Figure 4-51 Intended Displacement History vs. Captured Data, Test T8

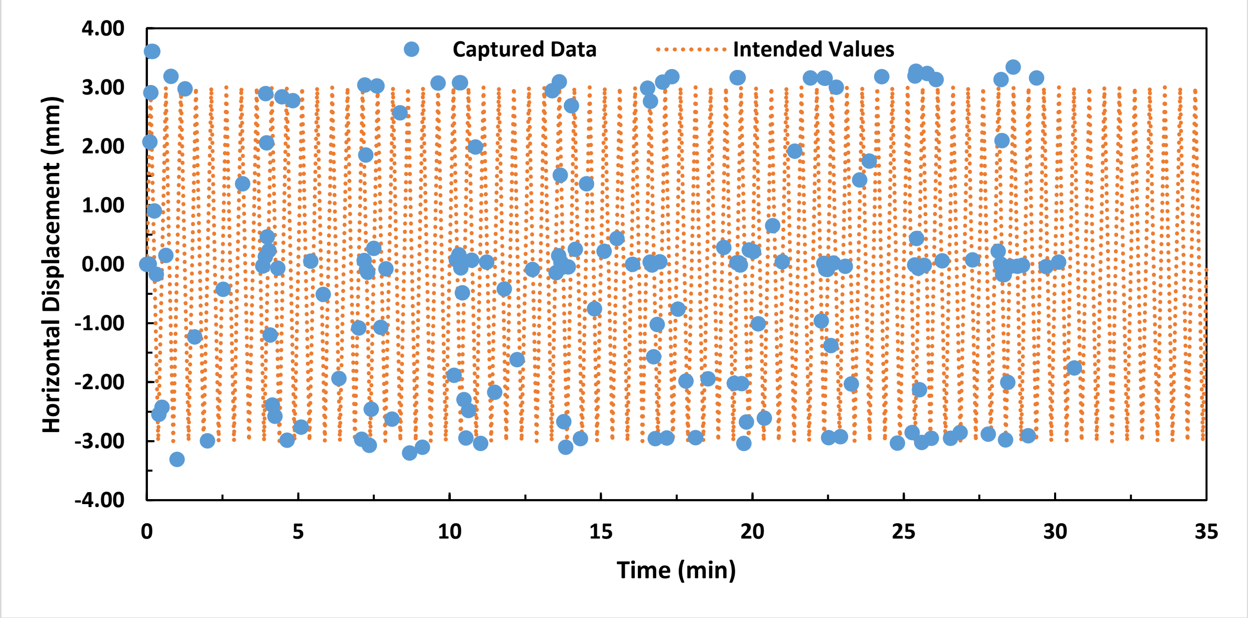

Figure 4-52 depicts the arrangement of the backfill along with in EPS geofoam inclusion and the geogrid prior to the beginning of the test while Figure 4-53 show the state at the end of the 100th cycle. The total surface settlement after 100 cycles was 61.49 mm, as shown in Figure 4-54. Settlement rate decreases with increasing number of cycles and it stabilizes around the 30th cycle.

Figure 4-52 Configuration Prior to Beginning of the Experiment, Test T8

Figure 4-53 Configuration at the End of Experiment, Test T8

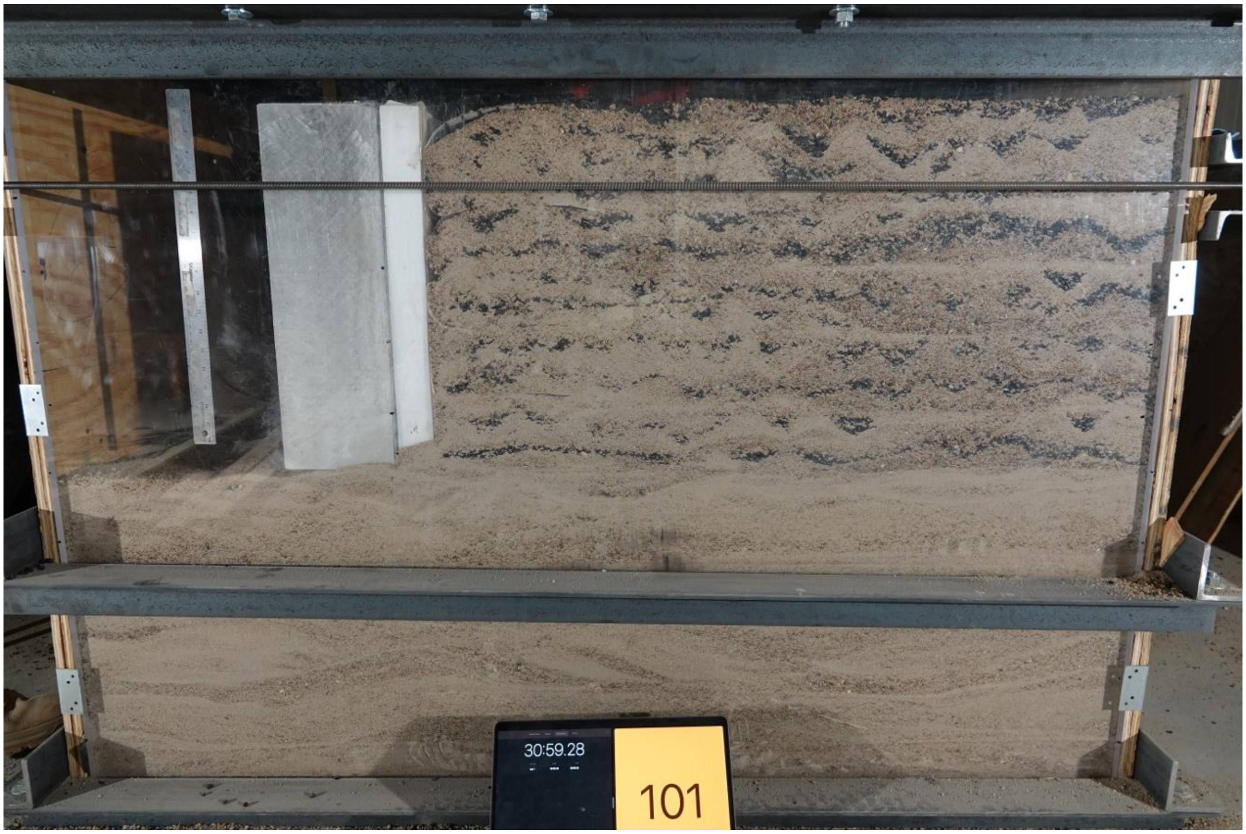

Figure 4-54 Cycle Number vs. Settlement, Test T8

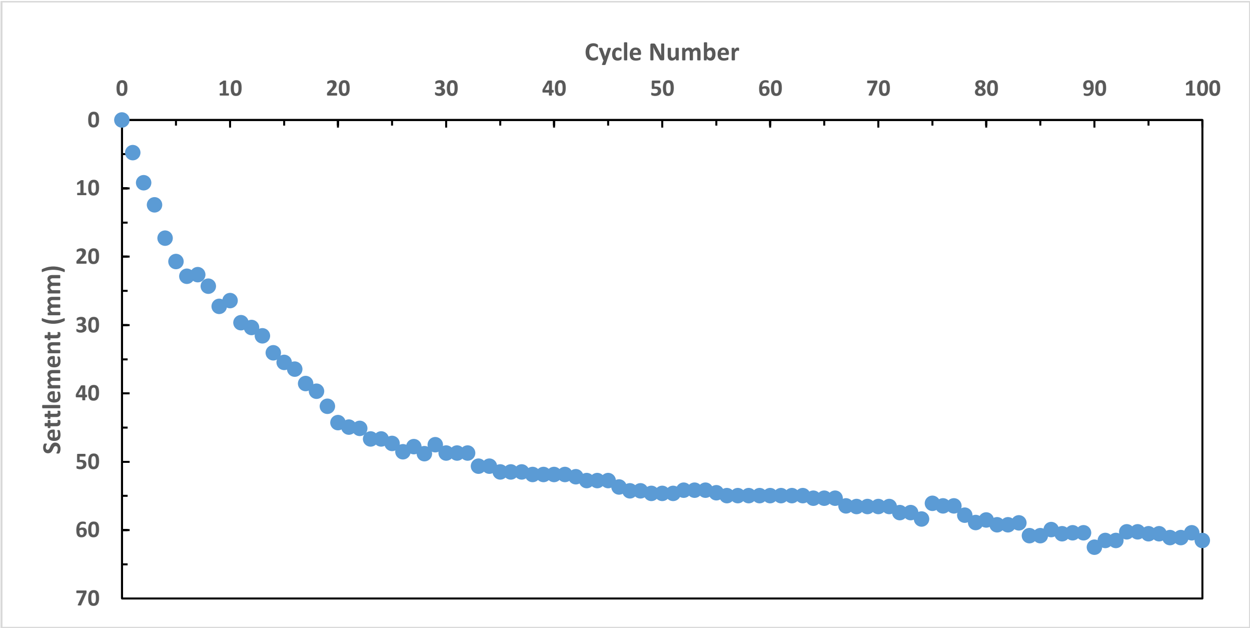

Figure 4 Figure 4-55 shows a heat map of Lagrangian shear strain that developed at the beginning of test T8. The map resembles the strain that developed in test T5, where soil was reinforced with geogrid. Consequently, a steep wedge zone behind the abutment forms, in which strain is gradually increasing. The maximum shear strain of 2.06% develops next to the EPS geofoam-soil interface, but a continuous interface shear band is not formed. A shear band indicating active failure is absent.

Figure 4-56 shows a heat map of Lagrangian shear strain that develops between the initial undeformed configuration and the beginning of cycle 5. The wedge zone of gradually increasing shear strain behind the abutment is now wider than in cycle one, but its right boundary is blurred while the interface shear band becomes more continuous with maximum shear strain of 6.75%.

Figure 4-55 Lagrangian Strain (ε_{xy}), Neutral to Active Position, Cycle 1, Test T8

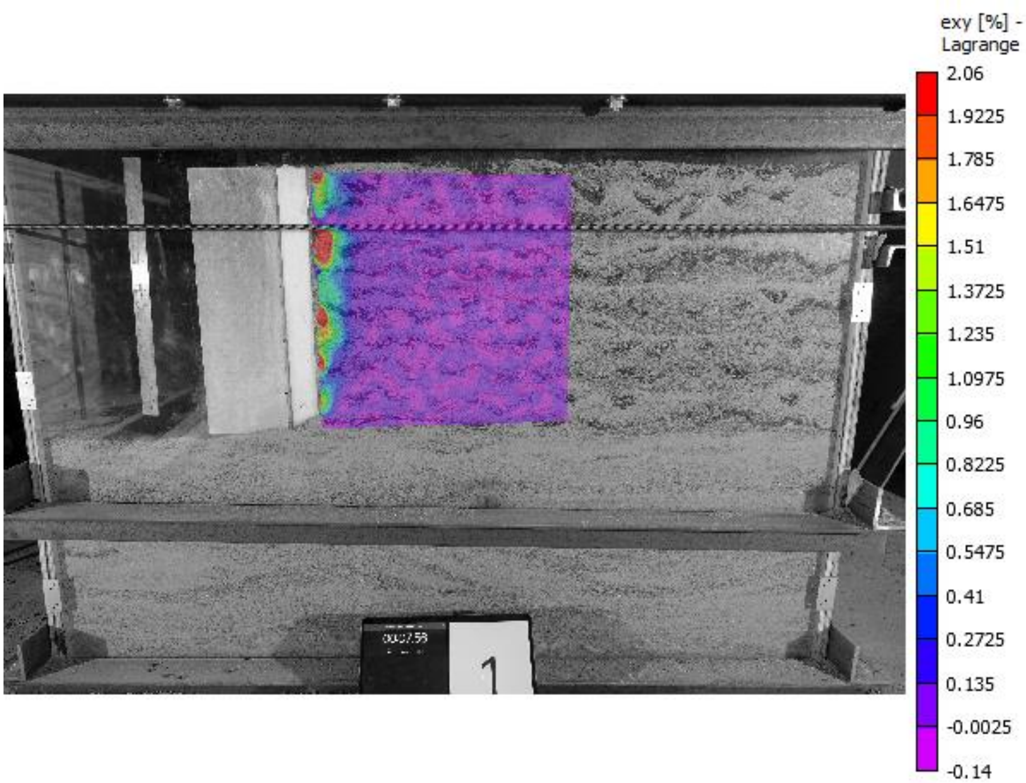

Figure 4-56 Lagrangian Strain (εxy), Neutral to Active Position, Cycle 5, Test T8

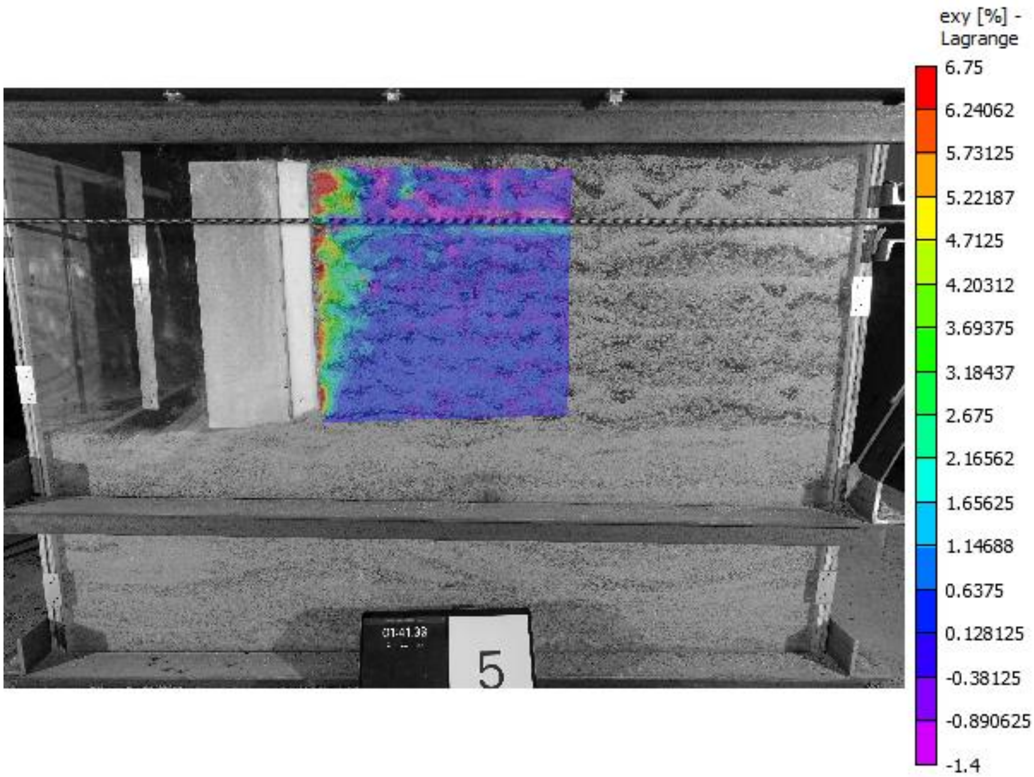

4.10 Test T9: Soft Density EPS 5.08 cm Geofoam Sheet with Geotextile (5 Layers)

In test T9, a 5.08 cm a soft EPS geofoam sheet was placed behind the abutment while the backfill behind it was reinforced with geotextile, forming five reinforced soil layers. Further details of reinforcement were provided in Table 4.2 in section 4.5. The maximum measured compressive force in the 1st cycle was 6.12 kN and it increased to 6.95 kN by the 91st cycle, as shown in Figure 4-57. Corresponding intended vs captured displacement history is shown in Figure 4-58.

Figure 4-57 Horizontal Force vs. Horizontal Displacement, Test T9

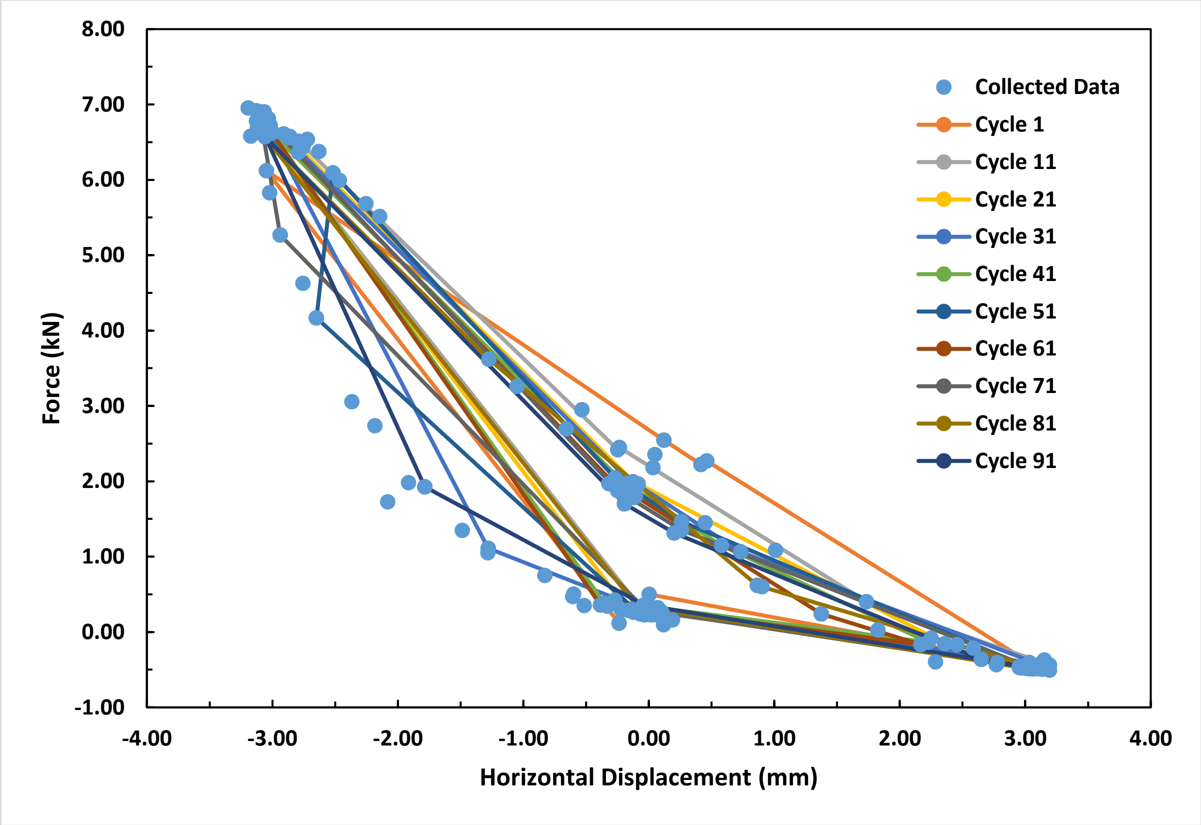

Figure 4-58 Intended Displacement History vs. Captured Data, Test T9

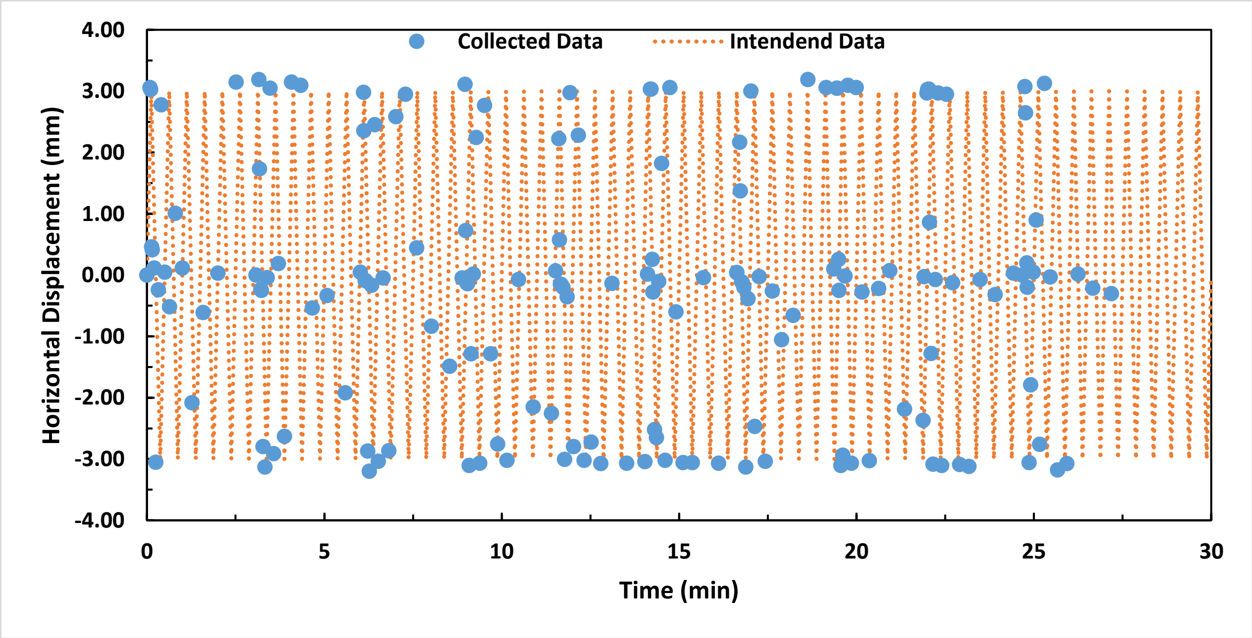

Figure 4-59 displays the configuration of the backfill along with the EPS geofoam inclusion and the geotextile before the beginning of the test while Figure 4-60 shows the state at the end of the 100th cycle. The total surface settlement after 100 cycles was 68.79 mm, as shown in Figure 4-61. The rate of settlement decreases and stabilizes around the 30th cycle.

Figure 4-59 Configuration Prior to the Beginning of Experiment, Test T9

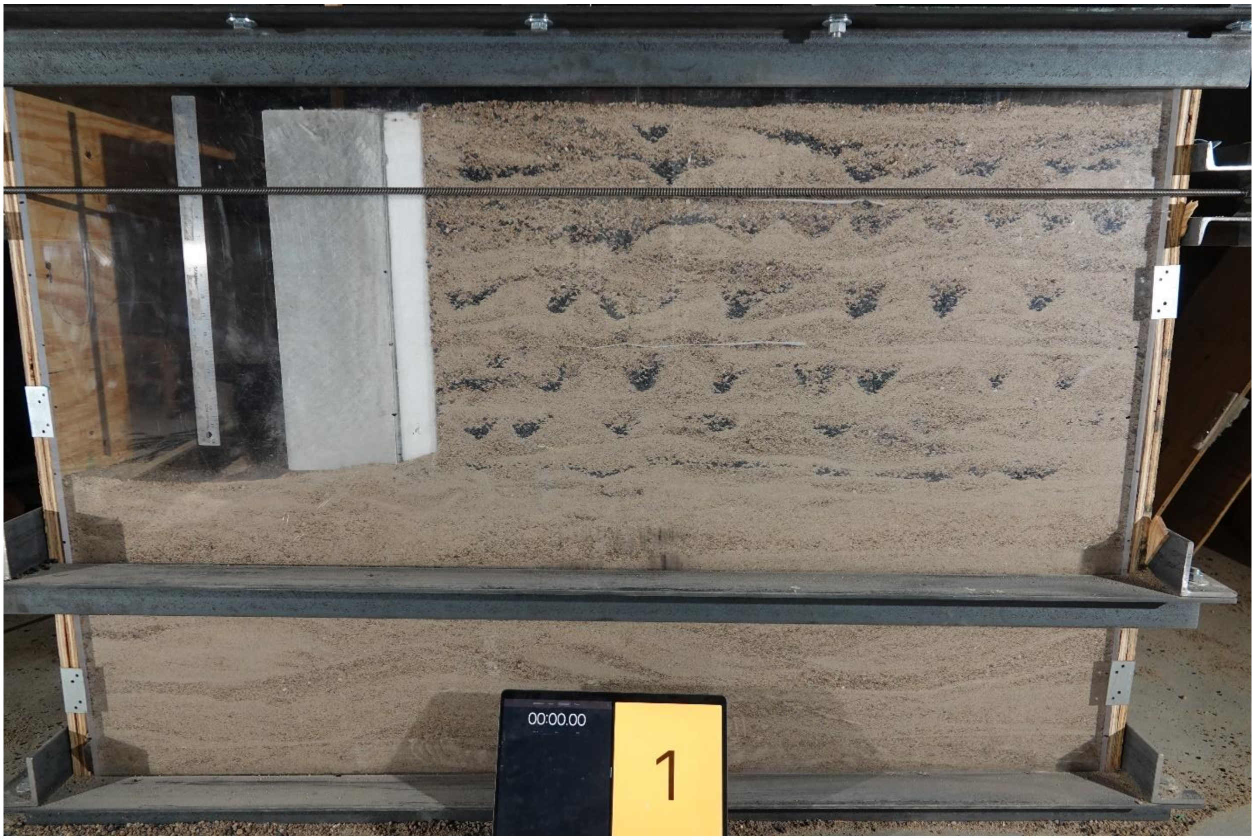

Figure 4-60 Configuration at the End of Experiment, Test T9

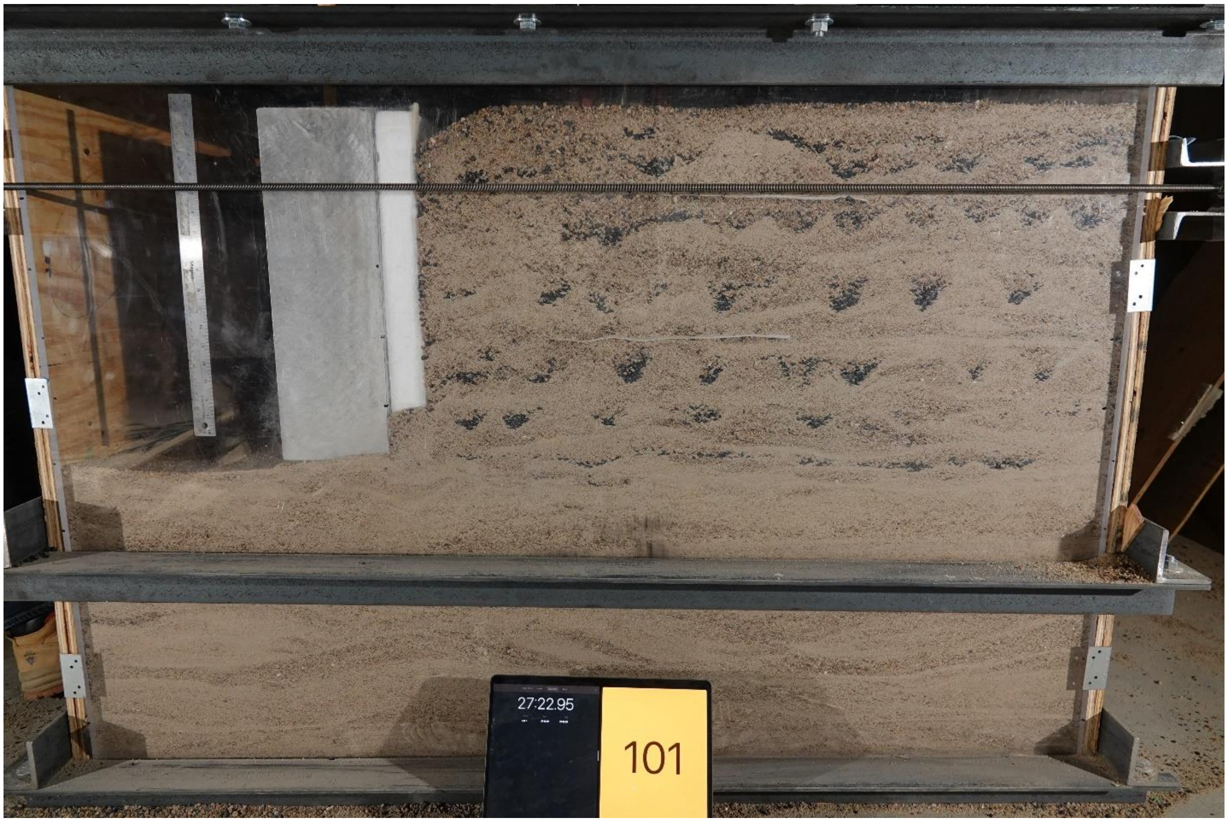

Figure 4-61 Cycle Number vs. Settlement, Test T9

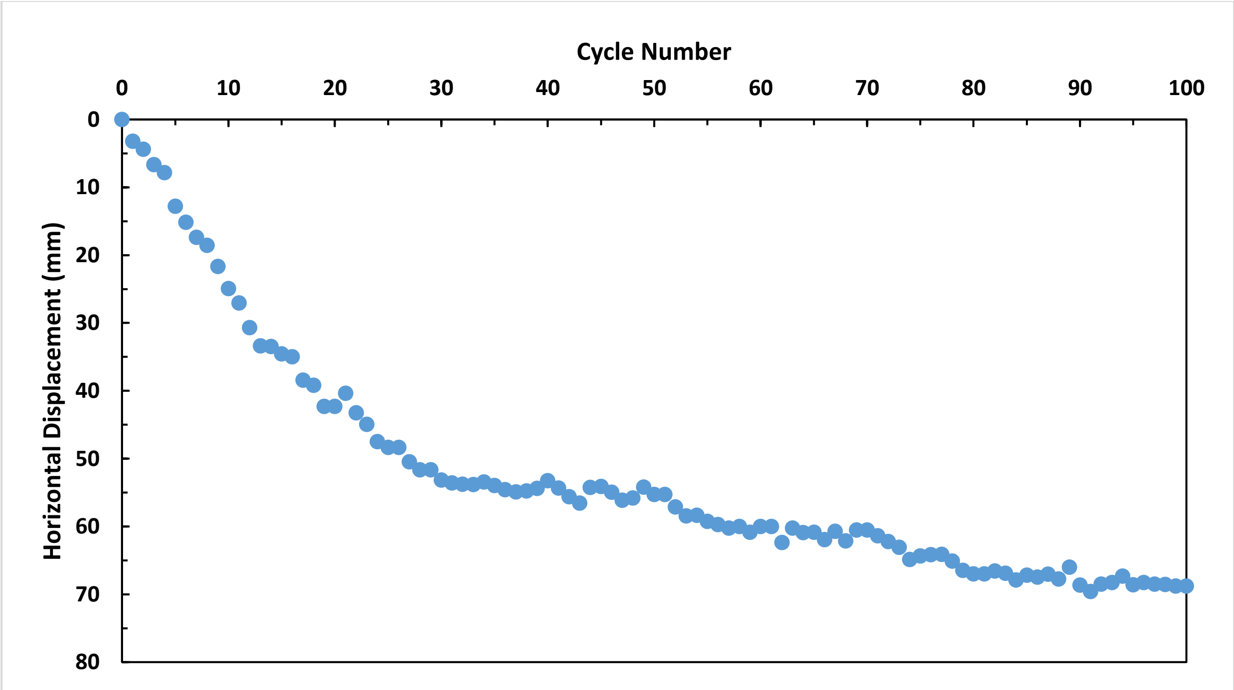

A steep wedge of gradually increasing Lagrangian shear strain forms next to the abutment-backfill interface culminating in development of a discontinuous interface shear band featuring the maximum strain of 2.06% in Figure 4-62. No shear band associated with active failure develops. Figure 4-63 shows a heat map of Lagrangian shear strain at the beginning of the 5th cycle, indicating that the vertical shear band has almost disappeared and maximum shear strain of 9.4% has migrated closer to the backfill surface.

Figure 4-62 Lagrangian Strain (ε_{xy}), Neutral to Active Position, Cycle 1, Test T9

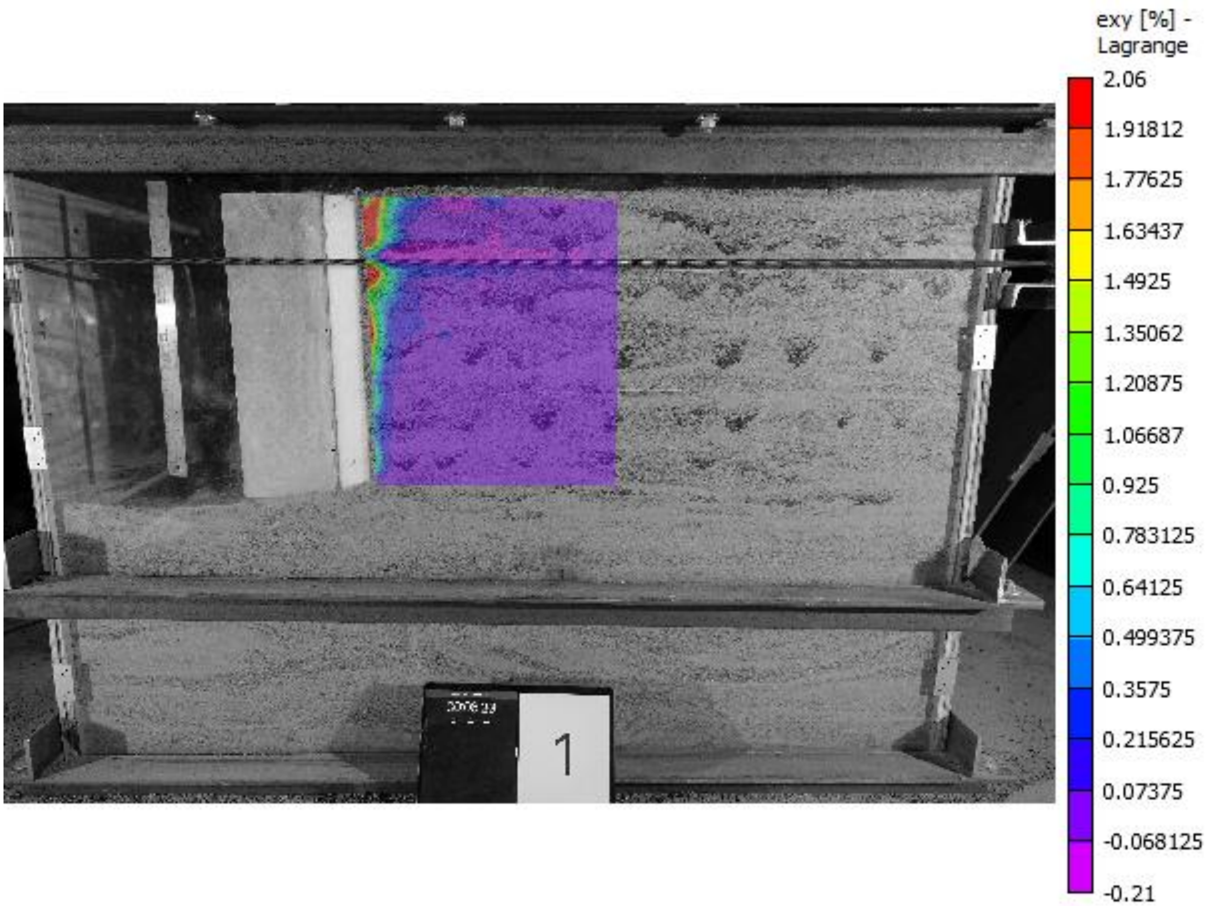

Figure 4-63 Lagrangian Strain (ε_{xy}), Neutral to Active Position, Cycle 5, Test T9

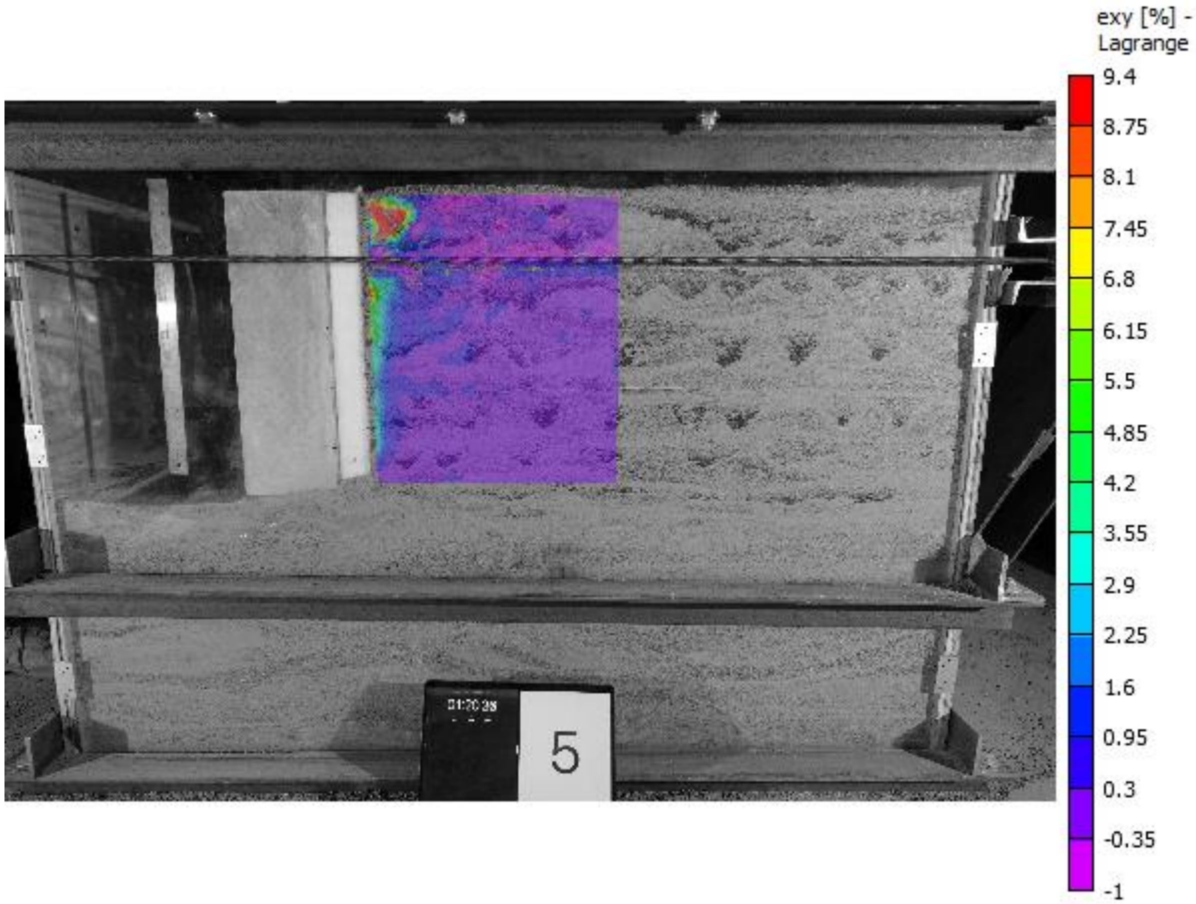

4.11 Test T10: Soft Density EPS 5.08 cm Geofoam Sheet with Geotextile (8 Layers)

Similarly, to test T9, a 5.08 cm EPS geofoam sheet was inserted behind the abutment and in front of the geotextile reinforced backfill resulting in eight reinforced soil layers. The spacing of the geotextile sheets and lap lengths are provided in Table 4-3.

Table 4.3 Configuration of Eight Layers of Geogrid

	Vertical Spacing (cm)	Lap Length (cm)	Length (cm)	Note
First Four Layers	6.00	40.0	50.0	
Top Layer	9.65	40.0	50.0	- A total of 10 cm of geotextile rests at the top the top of the backfill, followed by 10cm buried in the sand and inclined at approximately at 45° angle, followed by remaining 20 cm that is buried under 5cm of sand

The maximum measured compressive horizontal force in the 1st cycle was 5.44 kN and it increased to 5.84 kN in the 91st cycle, as shown in Figure 4-64. The corresponding intended vs captured horizontal displacement history is depicted in Figure 4-65.

Figure 4-64 Horizontal Force vs. Horizontal Displacement, Test T10

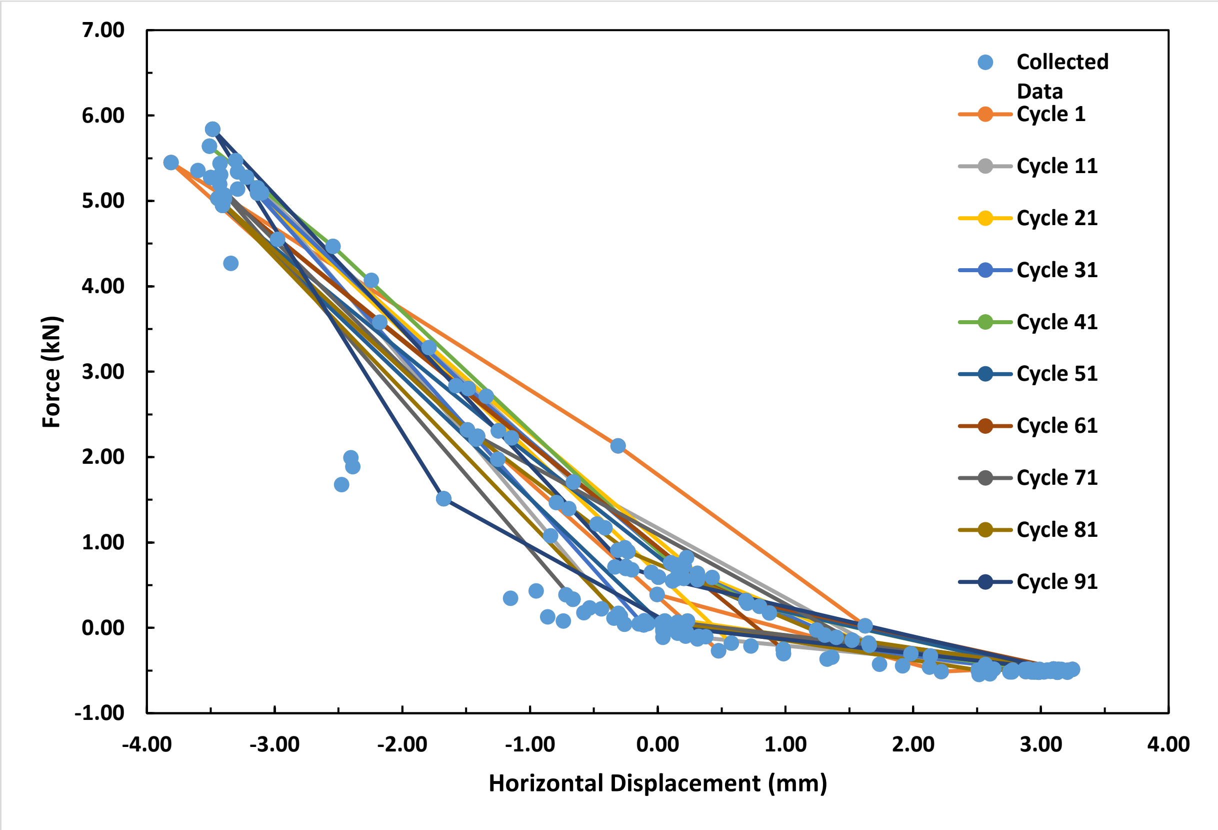

Figure 4-65 Intended Displacement History vs. Collected Data, Test T10

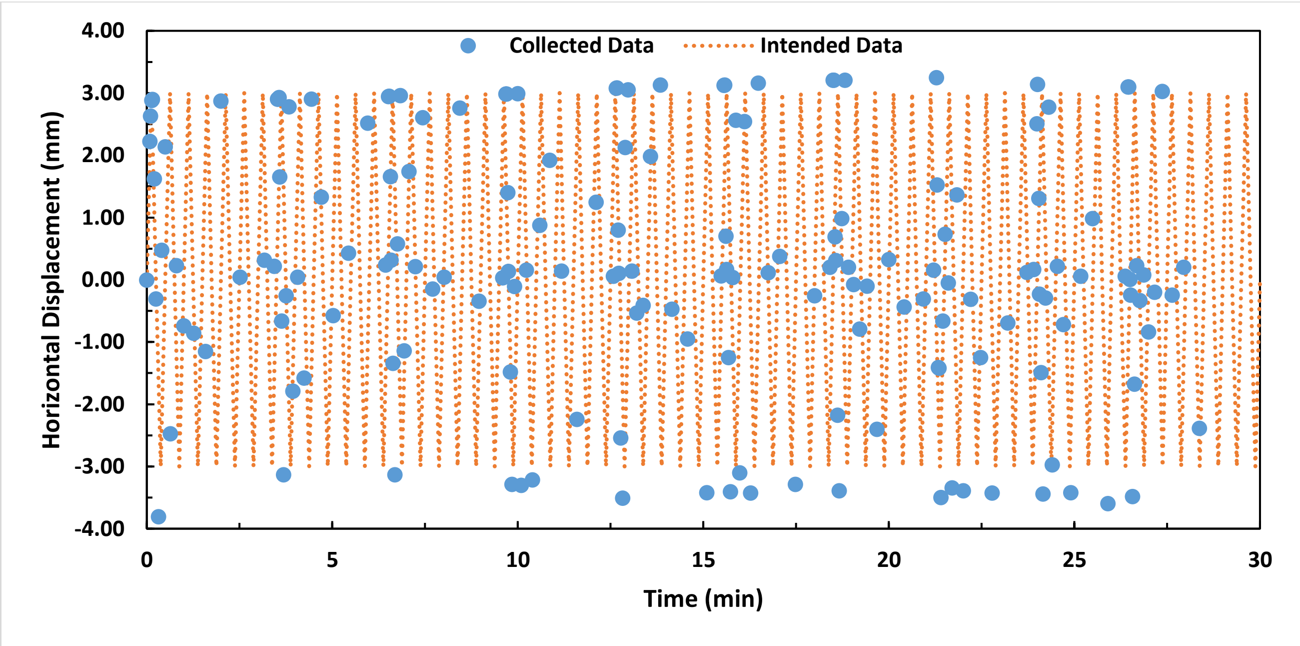

Figure 4-66 displays the configuration of the geotextile reinforced backfill along with the EPS geofoam inclusion prior to the beginning of the test while Figure 4-67 shows that state at the end of the 100th cycle. A progression of the interface settlement is depicted in Figure 4-68, showing that settlement rate decreases with increasing number of cycles and it stabilizes around the 45th cycle. Additionally, the settlement rate becomes equal to zero between the 80th and 95th cycle, culminating with the final settlement of 45.65 mm.

Figure 4-66 Configuration Prior to the Beginning of the Experiment, Test T10

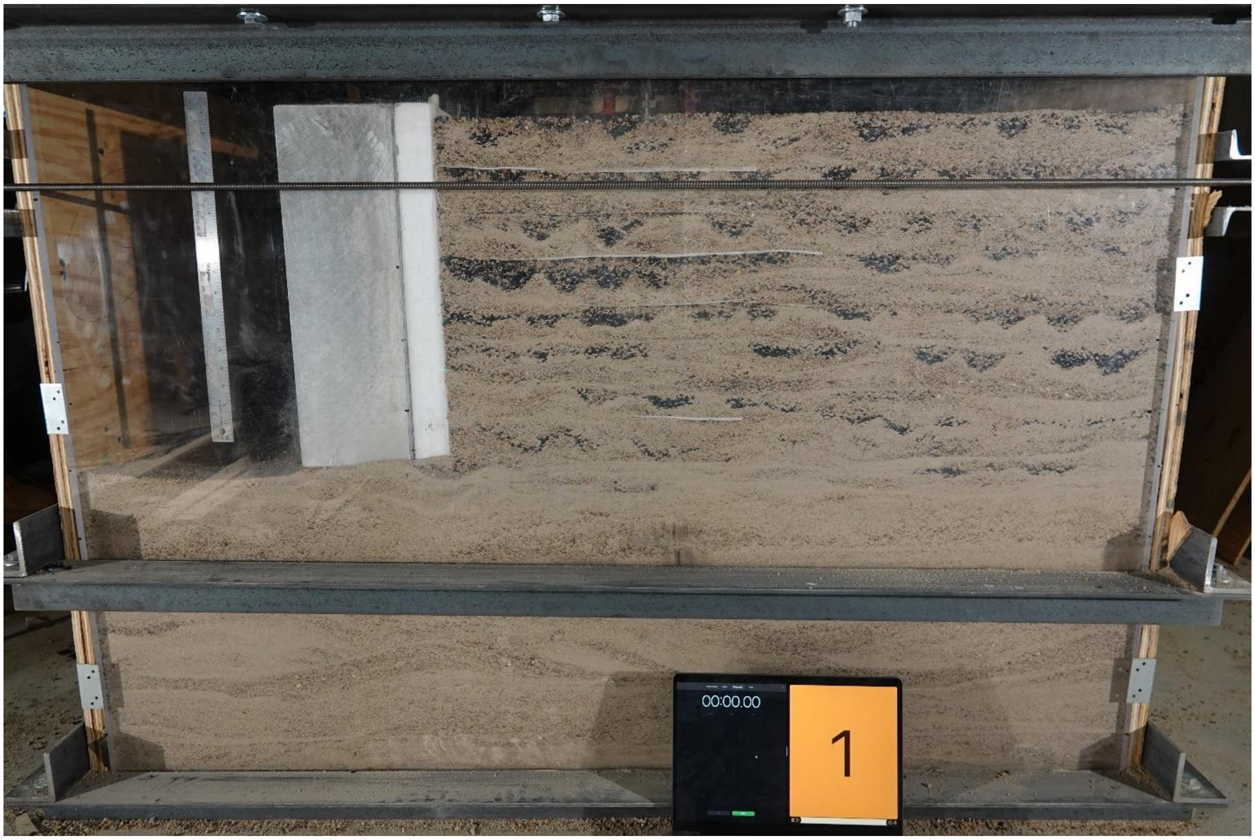

Figure 4-67 Configuration at the End of Experiment, Test T10

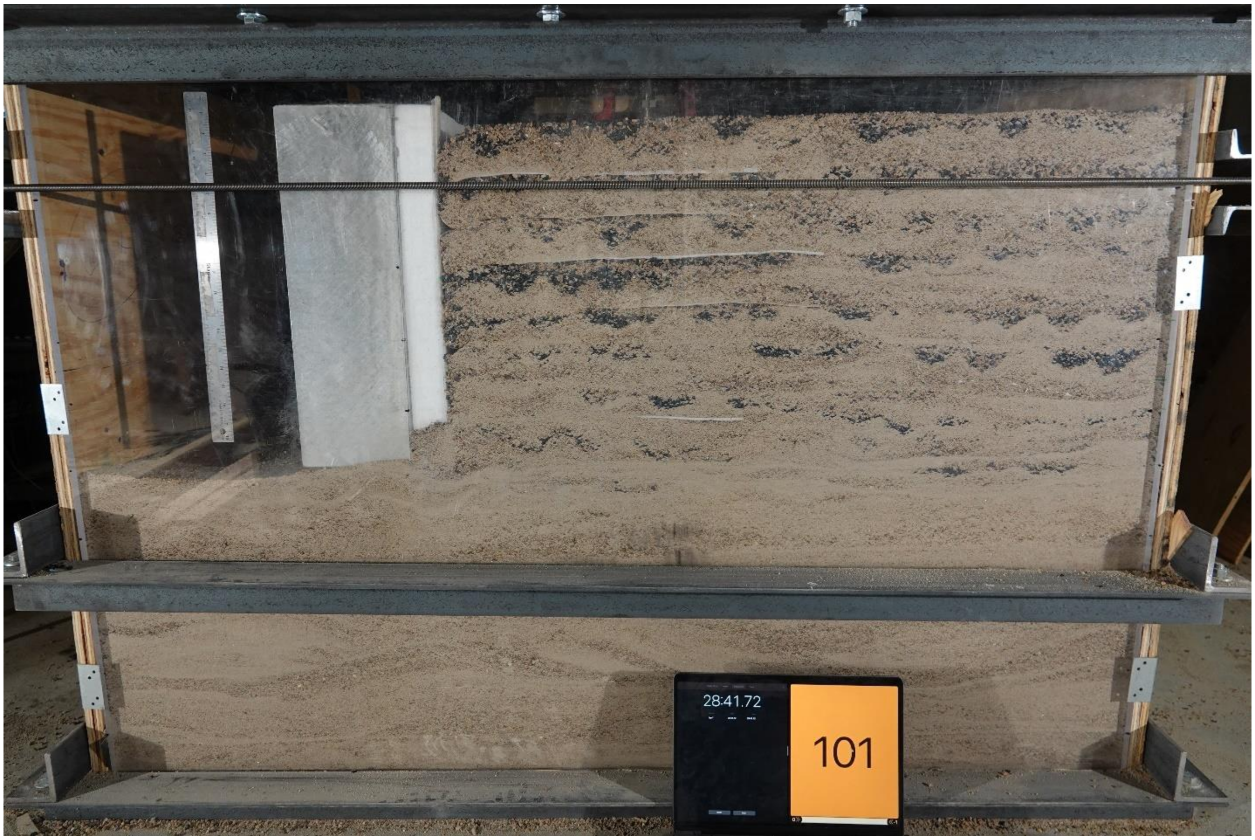

Figure 4-68 Cycle Number vs. Settlement, Test T10

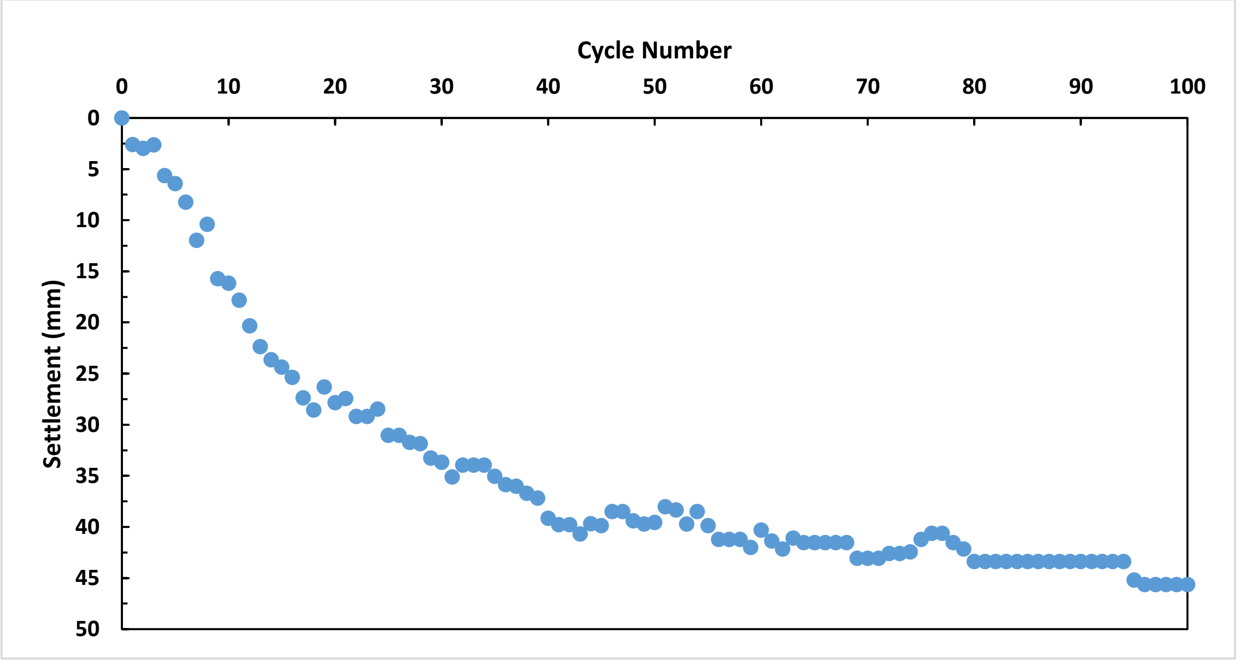

Figure 4-69 below shows a heat map of Lagrangian shear strain at the beginning of the test. Shear strain is localized within the narrow vertical interface shear band with maximum strain of 0.835%. Figure 4-70 shows a heat map of Lagrangian shear strain at the beginning of the fifth cycle. Shear strain remains localized within larger interface area, but slightly less continuously localized. No shear bands associated with active failure are identified.

Figure 4-69 Lagrangian Strain (ε_{xy}), Neutral to Active Position, Cycle 1, Test T10

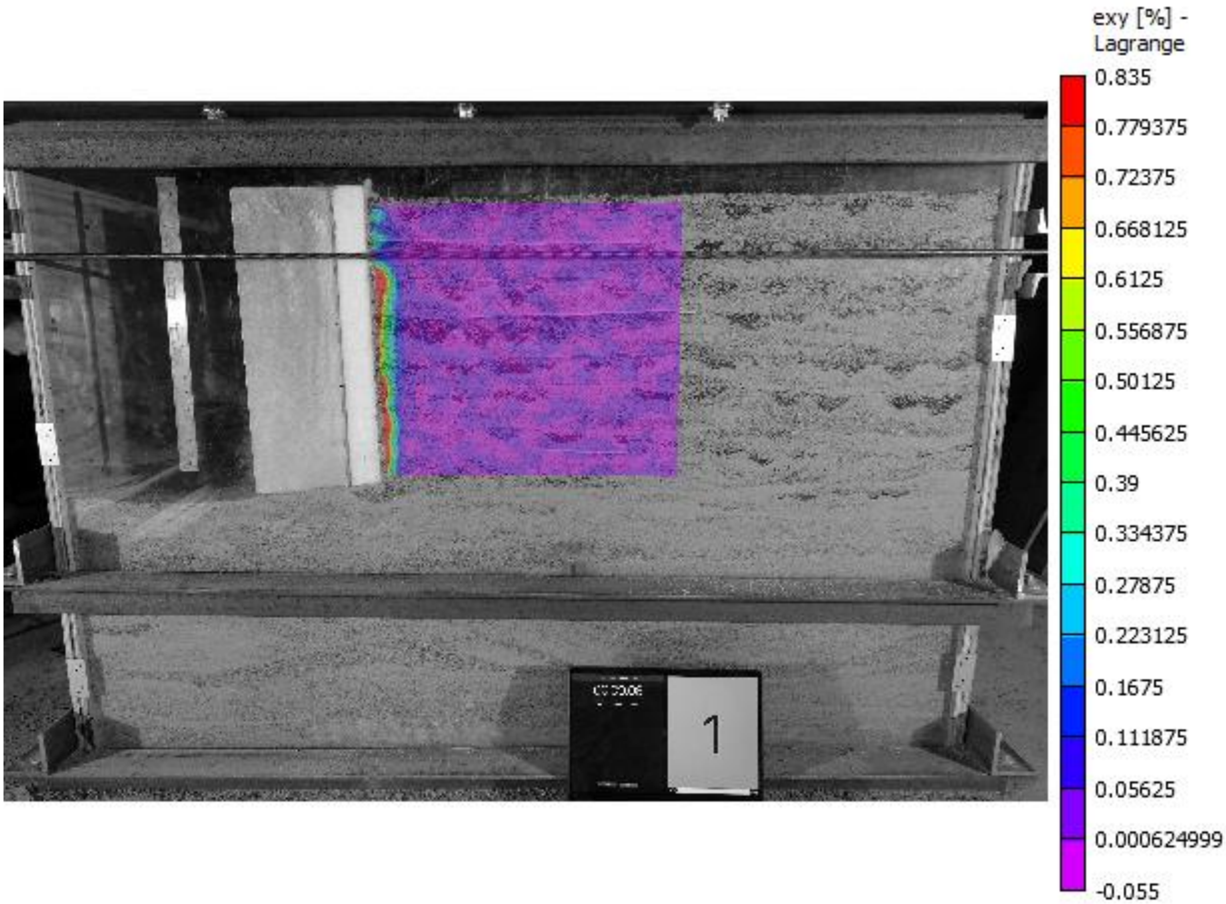

Figure 4-70 Lagrangian strain (ε_{xy}), Neutral to Active Position, Cycle 5, Test T10

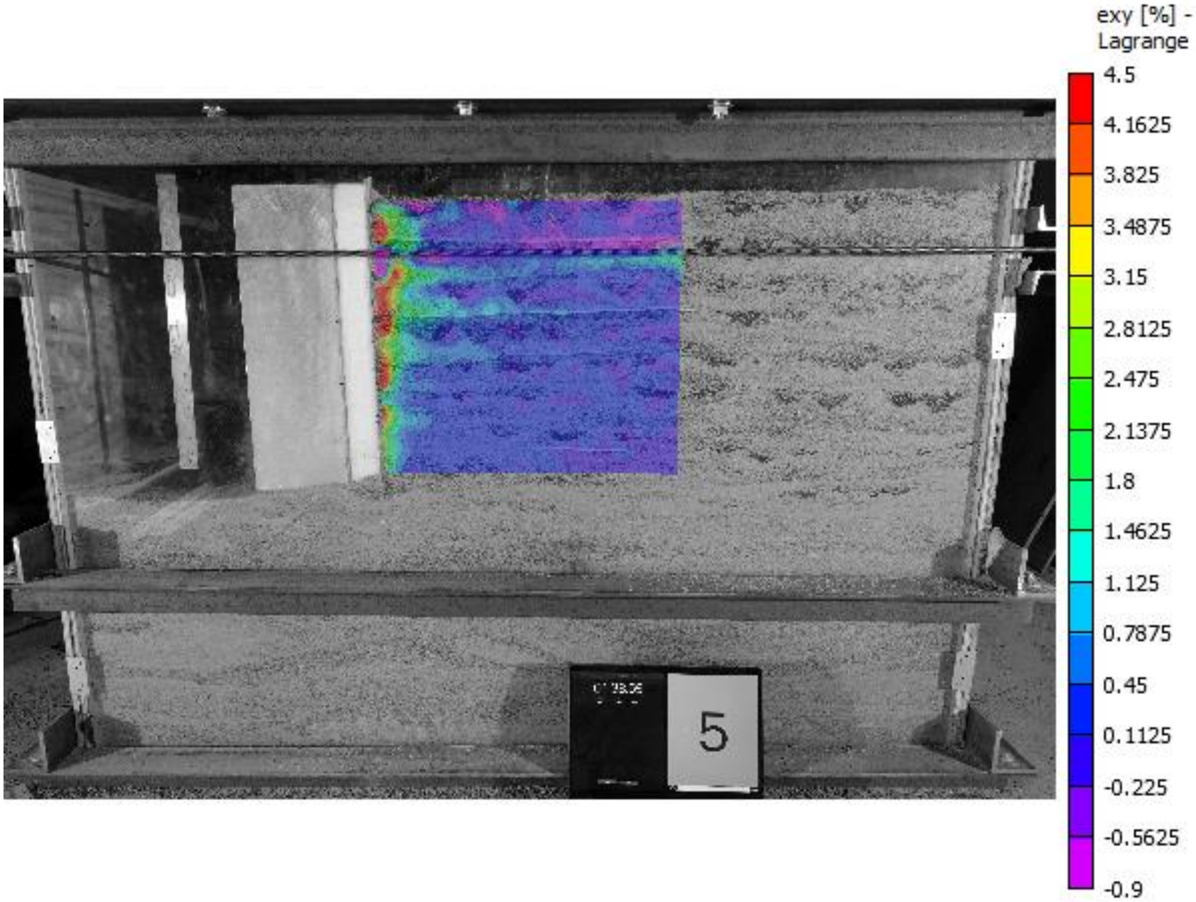

Chapter 5 - Discussion

In this chapter results collected from tests T1 through T10 are reviewed, further analyzed and compared with each other.

5.1 Subsidence Zone and Void Development

The settlement occurs primarily due to the collapse of the near surface soil behind the abutment while abutment moves away from the backfill. This leads to development of a subsidence zone and approach slab, which is not present in this investigation, loses the soil support and experiences distress that escalates with increasing number of load cycles. The size of the subsidence zone is characterized by its lateral extent away from the abutment back-face or soil's interface with the EPS inclusion, and the interface settlement. The former is directly related to the approach slab distress while the latter is likely related to the currently employed mitigation methods. Minimizing the size subsidence zone and void development leads to less frequent repairs and decreased maintenance costs.

Photographs taken during each test in conjunction with software ImageJ are used to obtain the lateral extent of the subsidence zones developed in each test. Figure 5-1 shows both, the lateral extent and interface settlement for all tests at the end of 100 cycles. The distance in Figure 5-1 is measured from the interface of backfill with abutment, or EPS geofoam, or reinforced backfill, depending on the particular test. The lateral extent and interface settlements are shown for all ten tests in Figure 5-1. The subsidence zone is further characterized in Table 5.1 that shows both, the lateral extent and interface settlement for all ten tests.

Figure 5-1 Settlement vs. Distance from the Interface, Cycle 100

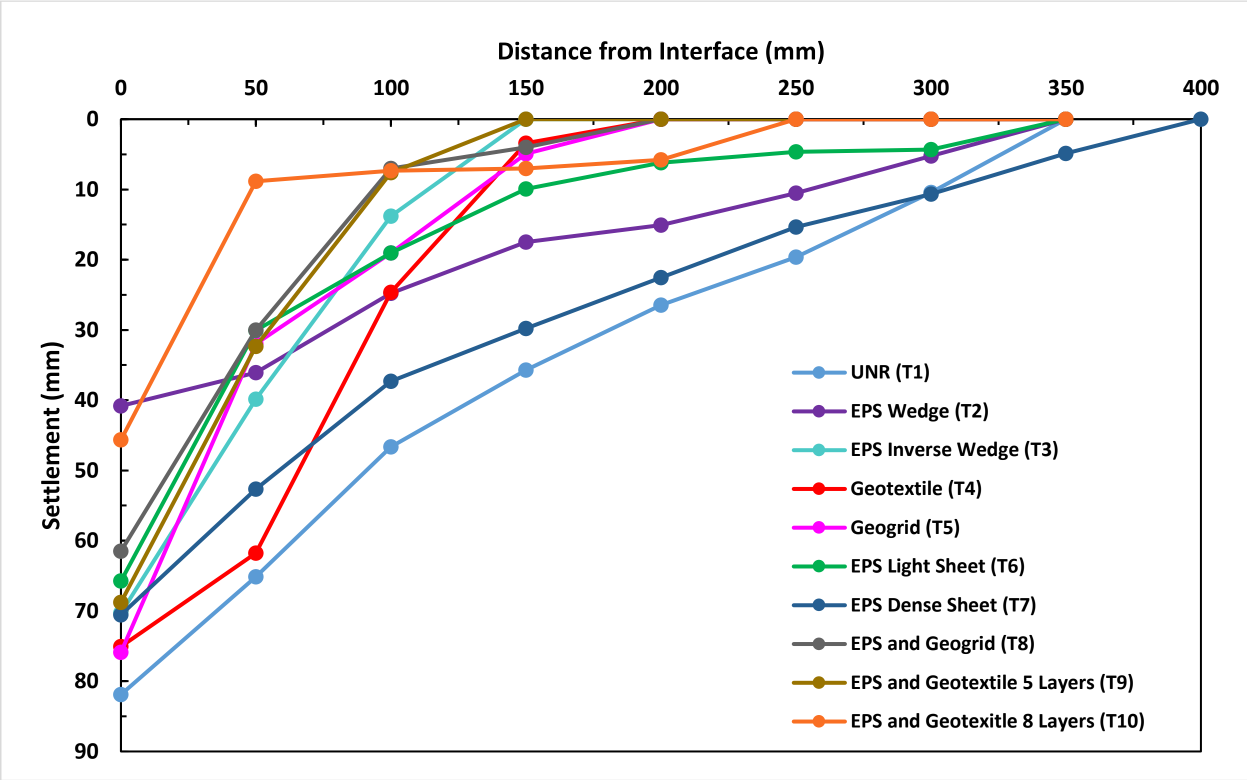

Table 5.1 Comparison of Settlement at Interface and Maximum Horizontal Distance of Affected by Settlement, Cycle 100

Test	Settlement at Interface (mm)	Max Distance Settlement Extends Past Interface (mm)
T1	81.90	350
T2	40.81	350
T3	70.30	150
T4	75.07	200
T5	75.87	200
T6	65.75	350
T7	70.54	400
T8	61.49	200
T9	68.77	150
T10	45.65	250

With regard to the approach slab distress the best performing tests would be those with the smallest lateral extent of the subsidence zone. After 100 cycles these are test T3 and test T9. Nevertheless, bridges are repaired much sooner before they experience 100 cycles of thermal loading corresponding to 100 years. To this end, Figure 5-2 and 5-3 show settlement vs its horizontal extent after five and ten cycles respectively. Similarly, to Table 5.1, Tables 5.2 and 5.3 summarize data presented in Figures 5-2 and 5-3.

Figure 5-2 Settlement vs. Distance from Interface, Cycle 5

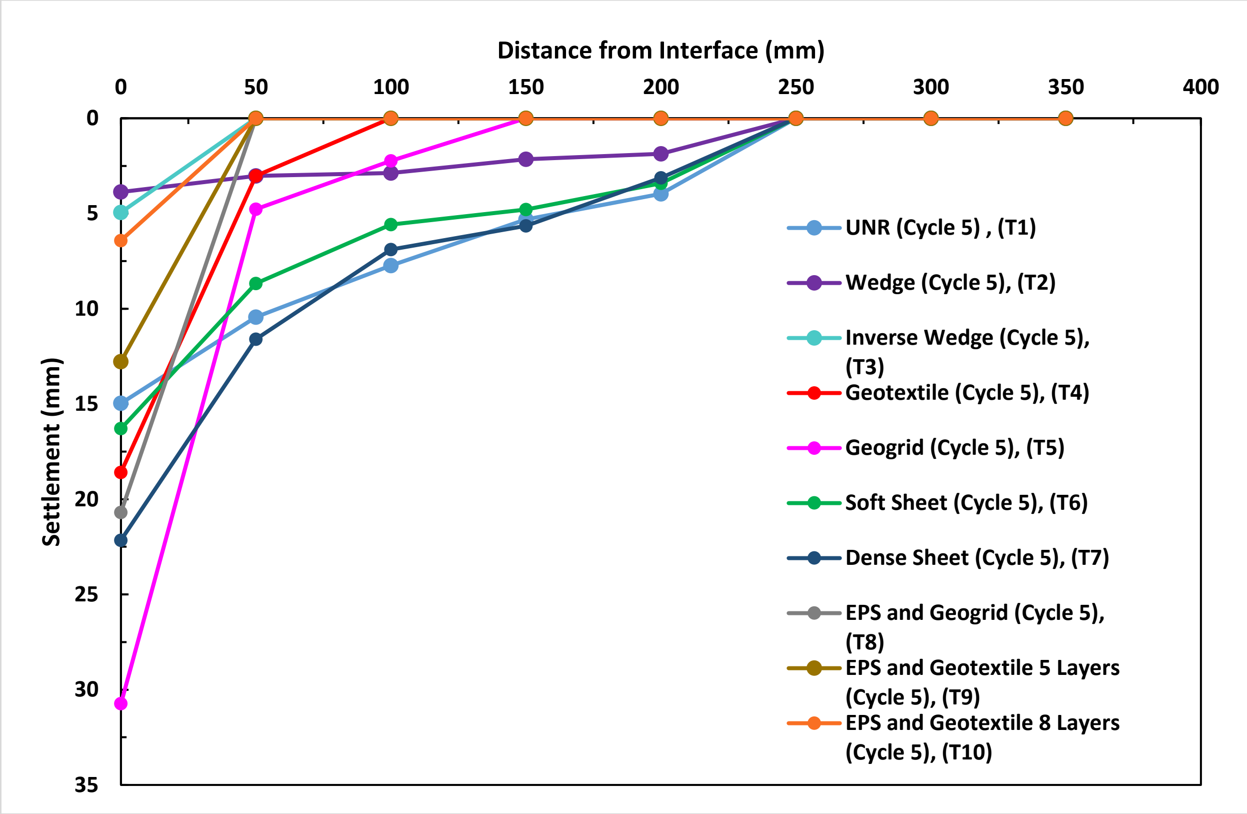

Table 5.2 Comparison of Settlement at Interface and Maximum Horizontal Distance of Affected by Settlement, Cycle 5

Test	Settlement at Interface (mm)	Max Distance Settlement Extends Past Interface (mm)
T1	14.97	250
T2	3.87	250
T3	4.94	50
T4	18.59	100
T5	30.74	150
T6	16.30	250
T7	22.15	250
T8	20.69	50
T9	12.78	50
T10	6.41	50

Figure 5-3 Settlement vs. Distance from Interface, Cycle 10

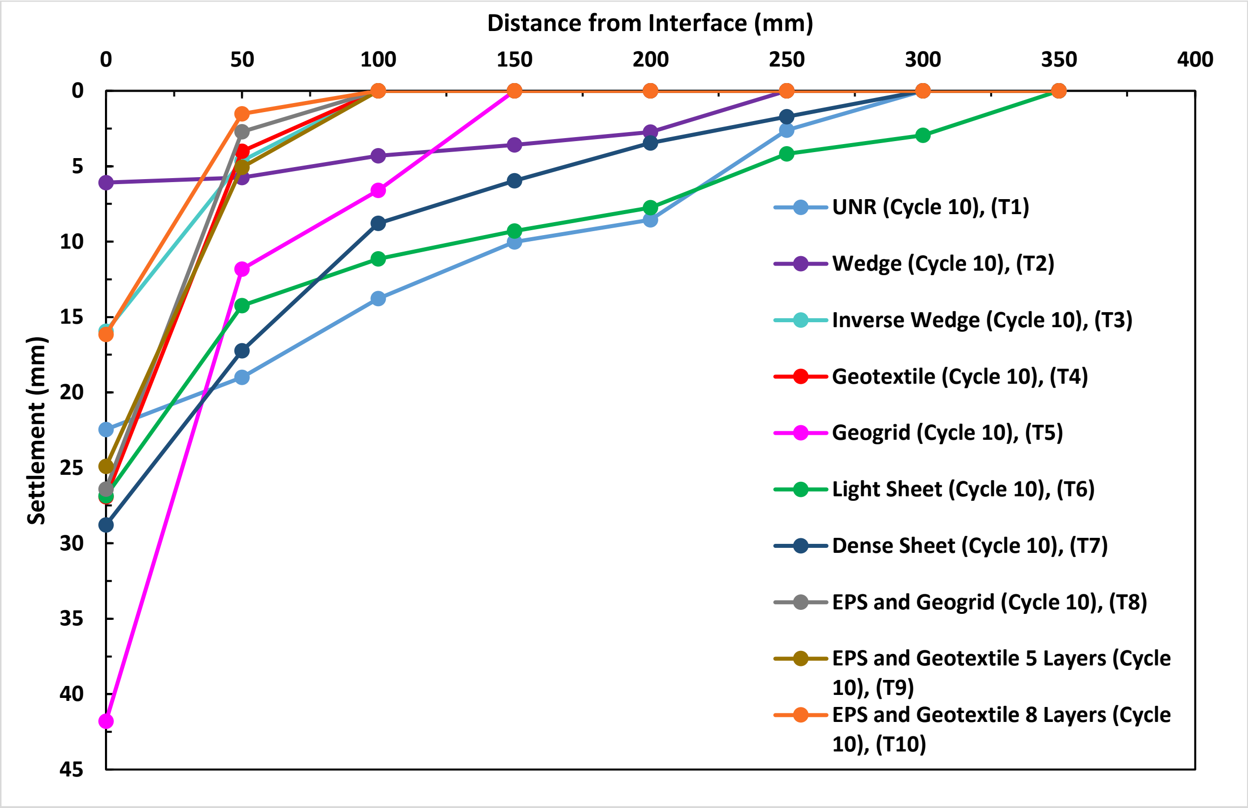

Table 5.3 Comparison of Settlement at Interface and Maximum Horizontal Distance of Affected by Settlement, Cycle 10

Test	Settlement at Interface (mm)	Max Distance Settlement Extends Past Interface (mm)
T1	22.45	300
T2	6.08	250
T3	15.95	100
T4	26.92	100
T5	41.81	150
T6	26.85	350
T7	28.78	300
T8	26.41	100
T9	24.91	100
T10	16.15	100

Based on Figure 5-2 and Table 5.2 test T3 that employed inverse wedge configuration resulted in the smallest amount of the interface settlement and smallest lateral extent of settlement after five cycles. According to Figure 5-3 and Table 5-3 the best two remediation methods are those employed in test T3 and T10, where the latter employs a combination of EPS geofoam and 8-layer geotextile reinforcement.

.

5.2 Reduction of Lateral Earth Force

The relationship between maximum measured compressive horizontal force and the interface settlement after 100 cycles was also obtained from the collected experimental data and it is summarized in Table 5.4. It is noted that the maximum force for each test was measured during the 91st Cycle.

Table 5.4 Comparison of Interface Settlement and Maximum Measured Compressive Horizontal Force

Test	Settlement at Interface (mm)	Maximum Lateral Force (kN)
T1	81.90	10.36
T2	40.81	6.49
T3	70.30	4.68
T4	75.07	7.63
T5	75.87	7.81
T6	65.75	9.36
T7	70.54	8.91
T8	61.49	8.03
T9	68.77	6.95
T10	45.65	5.84

As seen from Table 5.4, the maximum settlement and maximum force were measured in the reference test T1. Excluding test T1, the minimum settlement was observed in test T2 featuring EPS wedge, while minimum force was measured in test T3 featuring inverse EPS wedge. Test T10 that contained EPS sheet and eight layers of geotextile reinforcement resulted in the second minimum settlement, after test T2, and the second minimum force after test T3.

5.3 Calculated DIC Strains

In each test an interface shear band was detected by using in-plane Lagrangian shear strain computed by VIC-2D. In tests T1 and T2 an internal shear band was also present, indicating attainment of active failure. Table 5.5 shows orientation of shear bands with horizontal direction and corresponding maximum shear strains identified in cycle one.

Table 5.5 Orientation of Shear Bands and Corresponding Maximum Magnitudes of Lagrangian Shear Strains (ε_{xy}), Neutral to Active Position, Cycle 1

	Interface Shear Band			Internal Shear Band		
Test	Maximum Lagrangian Strain (%)		Shear Band Angle (°)	Maximum Lagrangian Strain (%)		Shear Band Angle (°)
	Magnitude	Sign		Magnitude	Sign	
T1	0.72	(-)	90	1	(+)	68
T2	1.04	(-)	90	1.33	(+)	69
T3	0.36	(+)	90	-	-	-
T4	2.96	(+)	90	-		-
T5	4.30	(+)	90	-		-
T6	2.42	(+)	90	-		-
T7	1.70	(+)	90	-		-
T8	2.06	(+)	90	-		-
T9	2.06	(+)	90	-		-
T10	0.83	(+)	90	-		-

Based on the information presented in Table 5.5, the internal shear bands developed only in tests T1 and T2, and they were inclined at 68º and 69º towards the horizontal direction respectively. This is close to the Coulomb's solution for the orientation of shear band given by

$$\theta = 45^\circ + \frac{\phi'}{2} \tag{5.1}$$

where θ is the inclination of shear band with horizontal direction, in this case. With effective friction angle of 42.2º equation 5.1 gives θ= 66.1º, which is close to the Coulomb's solution.

Similarly, to Table 5.5, Table 5.6 presents the maximum magnitude and the angles of the captured shear bands in cycle five. Compared to results in Table 5.5, the magnitudes of all shear strains increased. From Table 5.6 it is seen that the two tests that had the least amount of void development after 5 and 10 cycles. tests T3 and T10, also had the least amount of shear strain developing inside the interface shear bands

Table 5.6 Orientation of Shear Bands and Corresponding Maximum Magnitudes of Lagrangian Shear Strains (ε_{xy}), Neutral to Active Position, Cycle 5

	Interface Shear Band			Internal Shear Band		
Test	Maximum Lagrangian Strain (%)		Shear Band Angle (°)	Maximum Lagrangian Strain (%)		Shear Band Angle (°)
	Magnitude	Sign		Magnitude	Sign	
T1	3.25	(-)	90	5	(+)	68
T2	8.35	(+)	90	-	-	-
T3	1.34	(+)	90	-		-
T4	5.50	(+)	90	-		-
T5	8.75	(+)	90	-		-
T6	5.00	(+)	90	-		-
T7	5.50	(+)	90	-		-
T8	6.75	(+)	90	-		-
T9	8.34	(+)	90	-		-
T10	4.50	(+)	90	-		-

Chapter 6 - Conclusion and Recommendation for Future Studies

6.1 Conclusions

The outcomes of the experimental studies conducted in this study are summarized as follows:

- The settlement that develops next to the interface of abutment and backfill or EPS geofoam inclusion and backfill is one of the factors that should be considered when developing settlement remediation and alleviation methods. The other important factor that has direct bearing on the amount of approach slab distress is the lateral extent of the backfill surface settlement.
- The maximum measured horizontal force acting on the abutment appears to be related to the amount of interface settlement.
- The use of EPS geofoam as a fill material between the abutment and soil in the inverse wedge formation significantly reduces the lateral pressure and soil settlement in IAB approaches. The inverse wedge after 5 and 10 cycles features the smallest amount of interface settlement and the smallest lateral extent of the settlement.
- The use EPS geofoam sheet in combination with eight layers of geotextile, five layers of geotextile, and five layers of geogrid generally performs better than either EPS geofoam sheet on its own or any of the geosynthetics on its own. This can be attributed to the benefits that EPS geofoam has in reducing the lateral force on the abutment and the benefits that geosynthetics have in their ability to reduce the settlement.

- The strain fields obtained from VIC-2D indicate development of shear bands associated with active failure within the very first loading cycle for tests T1 and T2. No active shear bands were identified in any of the remaining tests throughout the first five cycles. Additionally, interface shear bands that result from the near surface sand collapse and subsequent falling of the sand particles into the interface region, and developing large shear strains were also detected.
- Using DIC software VIC-2D is a viable method for capturing displacements, strains and associated failure and collapse mechanisms in granular backfill. Nevertheless, total Lagrangian shear strain measure can be successfully employed only throughout the first five cycles, during which the backfill experiences smaller displacements. VIC-2D then compares each image to the reference photo representing the undeformed configuration and if the displacements are too large the subset of pixels will fall out of the search window, and VIC-2D fails to find any displacement. This can be remedied by using incremental strains or updating the undeformed configuration.

6.2 Recommendation for Future Studies

- This research has shown that EPS geofoam performs effectively in reducing the differential settlement that develops in IAB approaches due to its ability to decrease the lateral force. Further studies that would consider combinations of wedge and inverse wedge with use of geosynthetics are advised.
- It is recommended to investigate the effect of backfill soil density on development of bridge approach settlement.

- It is also recommended to investigate effect of different magnitude of horizontal displacements, or different amount of Δ/H on development of bridge approach settlement.

References

Al-Qarawi, A. (2016). The application of EPS geofoam in mitigating the approach problems in integral abutment bridges (Master's thesis, Western Sydney University (Australia)).

Al-Qarawi, A. (2021). A study on the fundamental behavior of soil-structure interaction and mitigating effects of EPS geofoam inclusions in integral abutment bridges. (PhD., Dissertation, Western Sydney University (Australia))

Arsoy, S., Barker, R. M., & Duncan, J. M. (1999). The behavior of integral abutment bridges (Vol. 3, p. 13). Charlottesville, VA: Virginia Transportation Research Council.

Barker R., Duncan, J., Rojiani., Ooi, P., Tan, C., and Kim, S. (1992) National Cooperative Highway Research Program Report 343: Manuals for the Design of Bridge Foundations. https://onlinepubs.trb.org/onlinepubs/nchrp/nchrp_rpt_343.pdf

Bureau of Transportation Statistics. (2023). State transportation infrastructure. State Transportation Infrastructure | Bureau of Transportation Statistics. https://www.bts.gov/state-transportation-infrastructure

Burke Jr, M. P. (2009). Integral and semi-integral bridges. John Wiley & Sons.

Das, B. M., & Sivakugan, N. (2018). Principles of foundation engineering. Cengage learning.

England, G.L., and Tsang, N.C.M. (2005). Design of soil loading for integral bridges. Indian Concrete Journal, 79(9): 53–59.

England, G. L., Tsang, N. C., & Bush, D. I. (2000). Integral bridges: a fundamental approach to the time–temperature loading problem. Thomas Telford.

FHWA, (2006). Shored Mechanically Stabilized Earth (SMSE) Wall Systems Design Guidelines, FHWA-CFL/TD-06-001, U.S. Department of Transportation

FHWA, (2018). Design and Construction Guidelines for Geosynthetic Reinforced Soil Abutments and Integrated Bridge Systems, FHWA-HRT-17-080, U.S. Department of Transportation

Hong, Y., Wang, X., Wang, L., Kang, G., & Gao, Z. (2024). High-cycle shakedown, ratcheting and liquefaction behavior of anisotropic granular material with fabric evolution: experiments and constitutive modelling. Journal of the Mechanics and Physics of Solids, 105638.

Hoppe, E., Weakley, K., & Thompson, P. (2016). Jointless bridge design at the Virginia Department of Transportation. Transportation Research Procedia, 14, 3943-3952

Huntley, S. A., & Valsangkar, A. J. (2013). Field monitoring of earth pressures on integral bridge abutments. Canadian Geotechnical Journal, 50(8), 841-857

Jacky, J. (1944). The coefficient of earth pressure at rest. journal for Society of Hungarian Architects and Engineers, 78(22), 355-358.

Kapogianni, E., & Sakellariou, M. (2017). Application of particle image velocimetry (PIV) and digital image correlation (DIC) techniques on scaled slope models. Int Res J Eng Technol (IRJET), 4(9), 853-860.

Liberzon, A., Lasagna, D., Aubert, M., Bachant, P., Käufer, T., jakirkham, Bauer, A., Vodenicharski, B., Dallas, C., Borg, J., tomerast & ranleu (2020). OpenPIV/openpiv-python: OpenPIV – Python (v0.22.2) with a new extended search PIV grid option.

Lings, M.L., Dietz, M.S. (2005) The Peak Strength of Sand-Steel Interfaces and the Role of Dilation, Soils and Foundations, Volume 45, Issue 6,2005, Pages 1-14, ISSN 0038-0806, https://doi.org/10.3208/sandf.45.1.

Liu, H., Han, J., & Parsons, R. L. (2021). Mitigation of seasonal temperature change-induced problems with integral bridge abutments using EPS foam and geogrid. Geotextiles and Geomembranes, 49(5), 1380-1392.

Maier, P., Kuhlmann, U., Pfaffinger, M., Mensinger, M., Schneider, S., Zinke, T., & Ummenhofer, T., & Friedrich, H. (2014). Sustainability Assessment of Bridges – Recent German Research Results. http://dx.doi.org/10.13140/2.1.1656.4483.

Mayne, P. W., & Kulhawy, F. H. (1982). Ko-OCR relationships in soil. Journal of the Geotechnical Engineering Division, 108(6), 851-872.

Meymand, P.J., (1998). Shaking Table Scale Model Test of Nonlinear Soil-Pile-Superstructure Interaction in Soft Clay. (PhD., Dissertation, University of California, Berkley)

Mitoulis, S. A., Palaiochorinou, A., Georgiadis, I., and Argyroudis, S. (2016) Extending the application of integral frame abutment bridges in earthquake-prone areas by using novel isolators of recycled materials. Earthquake Engineering Structural. Dynamics., 45:2283–2301. doi:10.1002/eqe.2760.

Nova-Roessig, L., & Sitar, N. (2006). Centrifuge model studies of the seismic response of reinforced soil slopes. Journal of Geotechnical and Geoenvironmental Engineering, 132(3), 388-400.

Perić, D., Miletić, M., Shah, B. R., Esmaeily, A., & Wang, H. (2016). Thermally induced soil structure interaction in the existing integral bridge. Engineering Structures, 106, 484-494.

Peters, W. H., Ranson, W. F., Sutton, M. A., Chu, T. C., & Anderson, J. (1983). Application of digital correlation methods to rigid body mechanics. Optical Engineering, 22(6), 738-742.

Rickson, R. J. (2006). Controlling sediment at source: an evaluation of erosion control geotextiles. Earth Surface Processes and Landforms: The Journal of the British Geomorphological Research Group, 31(5), 550-560

Sarsby, R. W. (1985). The influence of aperture size/particle size on the efficiency of grid reinforcement. In Proc., 2nd Canadian Symp. on Geotextiles and Geomembranes (pp. 7-12).

Sigdel, L. D., Leo, C. J., Liyanapathirana, S., & Hu, P. (2021). Integral bridge abutment-soil interaction analysis using PIV technique. In Proceedings of the International Conference on Geotechnical Engineering, ICGE-Colombo-2020: Geotechnics in a Challenging Environment, 6-7th December 2021, Colombo, Sri Lanka (pp. 253-258).

Sigdel, L. D., Lu, M., Al-qarawi, A., Leo, C. J., Liyanapathirana, S., & Hu, P. (2023). Application of engineered compressible inclusions to mitigating soil-structure interaction issues in integral bridge abutments. Journal of Rock Mechanics and Geotechnical Engineering.

Stanier, S. A., Blaber, J., Take, W. A., & White, D. J. (2016). Improved image-based deformation measurement for geotechnical applications. Canadian Geotechnical Journal, 53(5), 727-739.

Ting, J. M., & Faraji, S. (1998). Streamlined analysis and design of integral abutment bridges. Report UMTC, 97-13.

VDOT, (2020). Abutments-Chapter 17, Virginia Department of Transportation.

White, D. J., & Take, W. A. (2002). Particle image velocimetry (PIV) software for use in geotechnical testing. University of Cambridge, Department of Engineering.

White, H & New York State Department of Transportation. (2007). Integral Abutment Bridges: Comparison of Current Practice Between European Countries and the United States of America. https://www.dot.ny.gov/divisions/engineering/technical-services/trans-r-and-d-repository/SR152.pdf

Wu, H., Yao, C., & Li, C. (2020). Review of application and innovation of geotextiles in geotechnical engineering. Materials, *13(7),* 1774